

2016

# Miniaturized RF Components With A Novel Tunable Engineered Substrate For Wireless Communication Systems

Yujia Peng

Follow this and additional works at: <http://scholarcommons.sc.edu/etd>

 Part of the [Electrical and Electronics Commons](#)

---

## Recommended Citation

Peng, Y.(2016). *Miniaturized RF Components With A Novel Tunable Engineered Substrate For Wireless Communication Systems*. (Doctoral dissertation). Retrieved from <http://scholarcommons.sc.edu/etd/3891>

This Open Access Dissertation is brought to you for free and open access by Scholar Commons. It has been accepted for inclusion in Theses and Dissertations by an authorized administrator of Scholar Commons. For more information, please contact [SCHOLARC@mailbox.sc.edu](mailto:SCHOLARC@mailbox.sc.edu).

MINIATURIZED RF COMPONENTS WITH A NOVEL TUNABLE ENGINEERED  
SUBSTRATE FOR WIRELESS COMMUNICATION SYSTEMS

by

Yujia Peng

Bachelor of Science  
Wuhan University of Technology, 2009

Master of Science  
Xidian University, 2012

---

Submitted in Partial Fulfillment of the Requirements

For the Degree of Doctor of Philosophy in

Electrical Engineering

College of Engineering and Computing

University of South Carolina

2016

Accepted by:

Guoan Wang, Major Professor

Mohammad Ali, Committee Member

Krishna Mandal, Committee Member

Fanglin (Frank) Chen, Committee Member

Cheryl L. Addy, Vice Provost and Dean of The Graduate School

© Copyright by Yujia Peng, 2016  
All Rights Reserved.

## DEDICATION

To my beloved family

## ACKNOWLEDGEMENTS

A four-year Ph.D. experience at the University of South Carolina is a difficult yet worthwhile journey for me because of the people who surrounded me along the way. This dissertation would not have been possible without the support from many kind people. It is my great pleasure to acknowledge those who have given me guidance, assistance and companionship.

Foremost, I would like to express my most sincere gratitude to my advisor and committee chair, Dr. Guoan Wang, for giving me the opportunity to participate in his research group. I am very fortunate to be his Ph.D. student. His inspiring ideas, broad scientific knowledge and illuminating instructions always lead me in my research work. What I have learned most from him is not how to be a good research scientist, but how to have an optimistic attitude towards frustrations and failures. His enthusiastic encouragement and patient guidance on both research as well as my career have been invaluable. I could not have imagined having a better advisor and friendlier mentor for my Ph.D.

I would like to thank Prof. Mohammad Ali, Prof. Krishna Mandal and Prof. Fanglin (Frank) Chen for their precious time and effort in serving on my Ph.D. committee and for their brilliant comments and valuable suggestions in the proposal defense and dissertation. I would especially like to thank Prof. Mohammad Ali and his Ph.D. student Nowrin Chamok for allowing me to use their equipped laboratory for fabrication and measurement. I am very grateful to the collaborators of our laboratory: Dr. Xinchuan Liu

and Prof. Xuejun Wen for working with me about the sensor design and fabrication. I want to thanks Dr. MVS Chandrashekhar and Dr. Alexander Grekov for training me and giving me the chance to use the clean room equipment.

Additionally, I am indebted to my colleagues in the laboratory of Smart Microwave and RF Technology: Tengxing Wang, Wei Jiang, B M Farid Rahman Yongmao Huang and Sam Wang, for stimulating research discussions, for the great efforts and helps in device fabrication, and for all the progress we have made together under the guidance of Dr. Guoan Wang. I also want to thank my office mates: Zhichao Liu, Wuzhao Yan, Zheqing Zhou and Lixing Yang for the friendly working environment and for making my research experience rich and colorful with our valuable time working and having fun together. Many thanks to the friends who helped me integrate into the overseas school life and make it memorable.

Finally, I would like to express my eternal gratitude to my beloved parents, grandparents and younger brother for their everlasting love and unlimited support. It is their constant encouragement and love that helps me get through the hard times of studying and allows me to enjoy life with a carefree mind. I would like to give thanks to my two uncles and aunts for their support and valuable advice which equip me with courage while studying abroad and for their help make the United States feel like home.

## ABSTRACT

There is an increasing demand for reliable sensor system capable of remote sensing and measuring interesting data. Although large communication range can be achieved, active wireless communication systems are still suboptimal in longtime applications due to their harmful battery supply. Inductively coupled passive devices, with the advantages in safe long-term implanting, structural simplicity, small fabrication footprint and low-cost production, are preferred in chronic monitoring, but little work has been done to optimize the performance of these systems, especially under some design constraints.

The model and optimization of an inductively coupled wireless pressure sensor system is presented in this dissertation. With MEMS and semiconductor technology, the pressure sensor is designed as a miniaturized LC resonant circuit operating in 402MHz within a small footprint of 3.2 mm by 3.2 mm. An optimization approach is conducted to analyze inductive as well as pressure sensitivity. With mutually dependent geometrical parameters and performance related RF characteristics considered in the full optimization of the system, the applied design of this experiment method can reduce the large number of combined groups of values in fractional simulations with a focus on a few performance related factors. The second task of this research is to improve the limited working range of the sensing system. A half-active wireless communication system is studied as an alternative solution to this problem. Wireless power harvesting circuits and auxiliary

data-acquisition circuits are integrated in the system for long distance communication. However, physical size of system also becomes large with the added circuits. The challenges of designing compact wireless communication system are proposed to be solved in this dissertation.

With the requirements of multi-band and multi-function in wireless communication systems with improved performance and reduced size, development of tunable miniaturized RF components are a promising solution to fulfill the trend. Many technologies have been investigated and applied to develop tunable devices including MEMS and semiconductor varactors, ferroelectric capacitors, and magnetically tunable inductors with ferromagnetic materials, etc. However, the tunability of reported devices using the above technologies is directly dependent on the individual design configurations, which limits the design flexibility and broader application. A unique solution is to design arbitrary tunable RF components using an engineered substrate with an embedded patterned permalloy (Py) thin film which was developed for the first time in this dissertation. With high and current-dependent permeability, an engineered substrate embedded with Py thin film is a promising and flexible approach to design compact frequency-agile RF devices. Py thin film is patterned into slim bars on an engineered substrate to improve its ferromagnetic resonant frequency (FMR) for RF and mmwave applications. Miniaturized RF components are first developed with the proposed engineered magneto-dielectric substrate in this dissertation. Permeability tunable smart substrate was also developed by integrating an array of DC bias lines to provide a tuning path of Py patterns. The design principles and factors affecting the characteristics of the engineered substrate have been fully analyzed. Design efficacy of the developed tunable



substrate has been demonstrated with implemented components including a patch antenna, a phase shifter, a bandpass filter, and a three-port bandpass filtering balun. The proposed engineered substrate is feasible in implementing arbitrary RF and microwave devices with improved tuning capability and design flexibility.

## TABLE OF CONTENTS

DEDICATION .....	iii
ACKNOWLEDGEMENTS.....	iv
ABSTRACT .....	vi
LIST OF TABLES .....	xi
LIST OF FIGURES .....	xii
LIST OF SYMBOLS .....	xvii
LIST OF ABBREVIATIONS.....	xviii
CHAPTER 1: INTRODUCTION.....	1
1.1 MOTIVATION AND BACKGROUND.....	1
1.2 CHAPTER OUTLINE .....	9
CHAPTER 2 INDUCTIVELY COUPLED WIRELESS SENSOR SYSTEM .....	13
2.1 INTRODUCTION.....	13
2.2 DESIGN AND OPTIMIZATION OF PRESSURE SENSOR .....	16
2.3 MODELING ANALYSIS OF RESONANT PRESSURE SENSOR.....	27
2.4 MODELING ANALYSIS OF WIRELESS SENSOR SYSTEM .....	32
2.5 EXPERIMENT OF WIRELESS SENSOR SYSTEM .....	45
2.6 CONCLUSIONS .....	50
CHAPTER 3 MAGNETO-DIELECTRIC SUBSTRATE WITH PATTERNED PY THIN FILM FOR THE MINIATURIZATION OF RF COMPONENTS .....	52
3.1 INTRODUCTION.....	52

3.2 MERITS OF MAGNETO-DIELECTRIC MATERIAL .....	53
3.3 CHARACTERIZATION OF MAGNETIC MATERIAL .....	57
3.4 MAGNETO-DIELECTRIC SUBSTRATE WITH PATTERNED PY THIN FILM .....	65
3.5 IMPLEMENTATION OF MAGNETO-DIELECTRIC SUBSTRATE .....	69
3.6 CONCLUSIONS .....	73
CHAPTER 4 ENGINEERED SUBSTRATE WITH PATTERNED PY THIN FILM FOR ELECTRICALLY TUNABLE RF COMPONENTS .....	74
4.1 INTRODUCTION .....	74
4.2 RECONFIGURABLE TECHNOLOGIES.....	75
4.3 ELECTRICALLY TUNABLE PY PATTERNS ENABLED ENGINEERED SUBSTRATE ....	85
4.4 IMPLEMENTATION OF TUNABLE ENGINEERED SUBSTRATE.....	88
4.5 CONCLUSIONS .....	110
CHAPTER 5 CHARACTERISTIC ANALYSIS OF ENGINEERED SUBSTRATE .....	112
5.1 INTRODUCTION.....	112
5.2 LIMITATIONS OF THE IMPLEMENTATION WITH ENGINEERED SUBSTRATE .....	112
5.3 TUNING PROPERTY OF ENGINEERED SUBSTRATE .....	120
5.4 CONCLUSIONS .....	132
CHAPTER 6 CONTRIBUTIONS AND FUTURE WORKS .....	134
6.1 SUMMARY OF CONTRIBUTIONS.....	134
6.2 FUTURE WORKS .....	136
REFERENCES .....	139

## LIST OF TABLES

Table2.1 Summary of optimized sensors.....	30
Table2.2 Varied diameter and total length of coils on SRF, inductor and capacitor .....	43
Table3.1 Classification of magnetic materials based on magnetic properties .....	59
Table4.1 Comparison of different types of tuning technologies.....	84
Table4.2 Equivalent permeability of the multi-layer substrate with the effects of patterned Py film.....	91
Table5.1 Extracted equivalent inductance under different permeability .....	127

## LIST OF FIGURES

Figure1.1 Wireless telemetry system with a simplified structure for the measurement of LC resonant sensor.....	2
Figure1.2 Half-active RFID based wireless communication system for wireless sensor system .....	4
Figure2.1 (a) 3D view of RB sensor (b) Top view of RB sensor .....	16
Figure2.2 Cross-section view of the construction of bio-pressure sensor .....	18
Figure2.3 Equivalent circuit model of resonant sensor with variable pressure-dependent capacitor on silicon substrate .....	20
Figure2.4 Optimization methodology of resonant sensor with EM structure.....	24
Figure2.5 Top view of optimized dimension of resonant pressure sensor for (a) Design 1 (b) Design 2 (c) Cross-section view of optimized resonant pressure sensor .....	25
Figure2.6 Optimized quality factor Q of planar inductor coil .....	26
Figure2.7 (a) Transmission coefficient of $S_{21}$ as a function of frequency (b) Calculated capacitance as a function of frequency .....	29
Figure2.8 (a) Quality factor of the inductor derived from the planar spiral coil of resonant pressure sensor (b) Calculated inductance from the planar spiral coil of resonant pressure sensor .....	29
Figure2.9 Sensitivity of resonant sensor to the deformation of air chamber (a) Frequency shift of resonant sensor for design 1 with gradually deformed air chamber (b) Frequency shift of resonant sensor for design 2 with gradually deformed air chamber.....	31
Figure2.10 Equivalent telemetric circuit model.....	33
Figure2.11 (a) EM models of wireless sensor system for the analysis of inductive sensitivity and pressure sensitivity.....	37
Figure2.12 Analysis of inductive sensitivity for (a) Design 1 (b) Design 2 at different telemetry distance .....	38

Figure2.13 Analysis of pressure sensitivity for (a) Design 1 (b) Design 2 with different deformation induced by the pressure .....	40
Figure2.14 Different types of hand-made spiral inductor for measurement .....	42
Figure2.15 (a) Measured inductance of primary coil (b) Measured quality factor of primary coil (c) Measured characteristic impedance of primary coil .....	45
Figure2.16 Fabricated resonant pressure sensor from design 1.....	46
Figure2.17 Experimental setup of wireless telemetric system for the measurement of resonant pressure sensor .....	47
Figure2.18 (a) Measured phase of impedance of the primary coil at the resonant frequency of pressure sensor with different pressure (b) Resonant frequencies of pressure sensor with different pressure .....	49
Figure3.1 Reflection and transmission of an incident electromagnetic wave on a boundary of two mediums with different permeability and permittivity .....	56
Figure3.2 Precession of spinning electron in a steady magnetic field .....	61
Figure3.3 Hysteresis of the magnetization $M$ versus an applied magnetic field .....	62
Figure3.4 (a) Internal magnetizations within ferromagnetic material (b) Identical external field from surface monopoles (c) The internal “demagnetizing” field from induced surface monopoles .....	63
Figure3.5 (a) Trimetric view of the construction of the patterned Py thin film on high resistivity silicon substrate.....	68
Figure3.6 (a) Top view of the no-magnetic patch antenna with optimized dimensions: $L_1=8\text{mm}$ , $L_2=6.34\text{mm}$ , $L_3=21.4\text{mm}$ , $W_1=0.45\text{mm}$ , $W_2=13.175\text{mm}$ , $W_3=28\text{mm}$ (b) side view of the patch antenna on magneto-dielectric substrate .....	70
Figure3.7 (a) Simulated return loss of patch antenna on multi-layered substrate with magnetic properties in an ideal case and without magnetic properties (b) Radiation pattern of magnetic antenna in elevation (YZ) plane (c) Radiation pattern of no-magnetic antenna in elevation (YZ) plane.....	71
Figure3.8 (a) Measurement of the magnetic patch antenna on magneto-dielectric substrate (b) measured return loss of magnetic antenna and no-magnetic antenna .....	72
Figure4.1 (a) Equivalent circuits for semiconductor switch in (a) OFF state and (b) ON state .....	77

Figure4.2 (a) Cross-section view of the two statues of RF MEMS components (a) No voltage applied (b) Pull-down electrode plate with voltage .....	78
Figure4.3 (a) Layout of tunable band-pass filter based on RF MEMS (b) Simulation and measurement results of tunable band-pass filter .....	79
Figure4.4(a) BST thin film based tunable low-pass filter on silicon substrate. (b) Measured transmission and reflection coefficients of BST thin film based high-pass filter under different voltages .....	80
Figure4.5 (a) 3D view of magnetically tunable bandpass filter based on partially magnetized ferrite substrate (b) Measured transmission coefficients under different magnetized field.....	82
Figure4.6 (a) Layout of CPW slow wave structure based electrically tunable transmission with nano-patterned Py thin films (b) Measured phase shift of CPW slow wave structure based electrically tunable transmission line with different DC current and regular CPW	83
Figure4.7 (a) Engineered smart substrate with zoom-in view of patterned Py film and DC bias line arrays (b) Application of multi-layer engineered substrate embedded with patterned Py thin film.....	88
Figure4.8 (a) Implementation of patch antenna with tunable engineered substrate (b) measured return loss of magnetic antenna under different DC current .....	90
Figure4.9 (a) Implementation of tunable transmission line based phase shifter on engineered substrate (b) Measured phase of transmission coefficient (S12) under different DC current.....	92
Figure4.10 (a) Schematic view of SRRs (b) Equivalent lumped circuit model.....	94
Figure 4.11 (a) (a) SRRs based band-pass filter with $W_f = 0.95mm$ , $W_1 = 0.8mm$ , $W_2 = 0.9mm$ , $W_{1i} = 0.8mm$ , $W_{2i} = 0.9mm$ , $S_1 = 0.4mm$ , $S_{1i} = 0.4mm$ , $S_2 = 0.5mm$ , $dg = 2.2mm$ , $S = 0.3mm$ . (b) Equivalent circuit model of filter.....	96
Figure4.12 Simulated coupling coefficient with different gap .....	98
Figure4.13 Comparison of simulated transmission zeros with different feed structure parameters .....	99
Figure4.14 Simulated transmission coefficient of bandpass filter under the equivalent permeability of different DC current .....	100
Figure4.15 Implementation of bandpass filter on engineered substrate enabled with patterned Py thin film and zoom in view of SRRs and Py patterns on engineered substrate .....	101

Figure4.16 Measured frequency shift of band-pass filter with engineered substrate under different DC current.....	102
Figure4.17 (a) Conventional coupled straight line and (b) Capacitive loaded coupled meander line.....	104
Figure4.18 Optimized dimension of BPF-balun in ANSYS HFSS with $W_{f1} = 1.05mm$ , $W_{f2} = 0.55mm$ , $W_1 = 1mm$ , $W_2 = 1mm$ , $W_{1i} = 0.95mm$ , $S = 0.3mm$ , $S_{1i} = 0.3mm$ , $S_2 = 1.1mm$ , $dg = 2.8mm$ , $dg1 = 3mm$ , $dg2 = 2.9$ .....	106
Figure4.19 (a) Simulated tunable transmission coefficient S12 with symmetric feeding, (b) Tunable transmission coefficient S13 with skew symmetric feeding, and (c) Phase imbalance between two balanced ports.....	107
Figure4.20 Implementation of tunable BPF-Balun with engineered substrate and zoom in view of Py patterns on silicon substrate and BPF-Balun on Rogers 4350 substrate .....	108
Figure4.21 (a) Tunable transmission coefficient S12 with symmetric feeding, (b) Tunable transmission coefficient S13 with skew symmetric feeding, and (c) Phase imbalance between two balanced ports .....	109
Figure5.1 (a) Layout of DC bias line under patterned Py thin film (b) Simulated EBG effects of DC bias lines on engineered substrate .....	113
Figure5.2 (a) Optical image of (a) Patterned Py film with length of 25 $\mu m$ and width of 10 $\mu m$ , and (b) Patterned Py film with length of 45 $\mu m$ and width of 5 $\mu m$ .....	115
Figure5.3 Variations of in-plane anisotropic field with the angular dependences of the romance ratio (M/ Ms) with different Py pattern sizes .....	116
Figure5.4 FMR effects on engineered substrate with different patterned Py thin film ...	118
Figure5.5 Tunable microstrip filter on engineered substrate with (a) one-layer patterned Py thin film with thickness of 100 nm (b) multi-layer patterned Py thin film with thickness of 1 $\mu m$ .....	121
Figure5.6 Patterning orientation of Py thin film with easy axis (a) Perpendicular to DC bias line (b) parallel to DC bias line .....	123
Figure5.7 Hysteresis loop of ferromagnetic material along easy axis and hard axis.....	124
Figure5.8 Electromagnetic field distribution in (a) Microstrip based transmission line (b) CPW based transmission line.....	126



Figure5.9 (a) Microstrip structure based bandpass filter (b) CPW structure based bandpass filter .....	129
Figure5.10 Analysis of effective tuning area for bandpass filter .....	131
Figure6.1 (a) 3D layout of fully electrically tunable engineered substrate (b) Top view of fully electrically tunable engineered substrate.....	138
Figure6.2 Improved layout of engineered substrate with discontinuous electrodes for partly tuning .....	138

## LIST OF SYMBOLS

$\mu$	Permeability
$\varepsilon$	Permittivity
$\delta$	Skin depth
$L$	Inductance
$C$	Capacitance
$Q$	Quality factor
$S$	Scattering parameter

## LIST OF ABBREVIATIONS

BST .....	Barium-Strontium-Titanate Oxide
CPW .....	Coplanar Wave Guide
DC .....	Direct Current
DOE .....	Design of Experiment
EBG.....	Electromagnetic Band Gap
EM.....	Electro Magnetic
FMR .....	Ferromagnetic Resonance
HFSS .....	High Frequency Structure Simulator
IC.....	Integrated Circuits
MEMS.....	Microelectromechanical systems
MICS.....	Medical Implant Communications Service
PCB .....	Printed Circuit Board
PDMS.....	Polydimethylsiloxane
PIFA .....	Planar Inverted-F Antenna
Py .....	Permalloy
PZT .....	Lead Zirconium Titanate
RF.....	Radio Frequency
RFID .....	Radio Frequency Identification
SRR.....	Split Ring Resonator
VNA .....	Vector Network Analyzer

# CHAPTER 1

## INTRODUCTION

### 1.1 Motivation and Background

Wireless communication systems integrated with sensors will play an increasingly important role in improving people's quality of life for tracking, sensing, drug delivery, and local stimulation. In particular, wireless sensor system, allowing in-vivo sensing, biometrics monitoring and diagnostics, has drawn great attentions in modern medical applications. Pacemaker communication [1], glucose monitoring [2], insulin pumps [3] and endoscopy [4] are a few examples of medical treatments that can take advantage of wireless control in sensors and help manage a broad range of medical disorders through preventive and post-surgery monitoring. While some biomedical sensors and their clinical applications prove that wireless physiological monitoring within the human body is feasible, their direct application in the human body for a long time is still limited due to the large dimension of sensors, and without proven safety or effectiveness.

With the requirements on the miniaturized biomedical sensor for high-performance wireless telemetry microsystems, a biomedical pressure sensor within a limited footprint of 3.2mm by 3.2mm is proposed and developed for wireless communication system in medical application. To obtain a high-sensitivity pressure sensor, a methodology of optimization on the EM models of the pressure sensor is presented and analyzed. The pressure sensor system as shown in Figure1.1 is designed with simplified wireless communication system for the telemetry of sensor. This

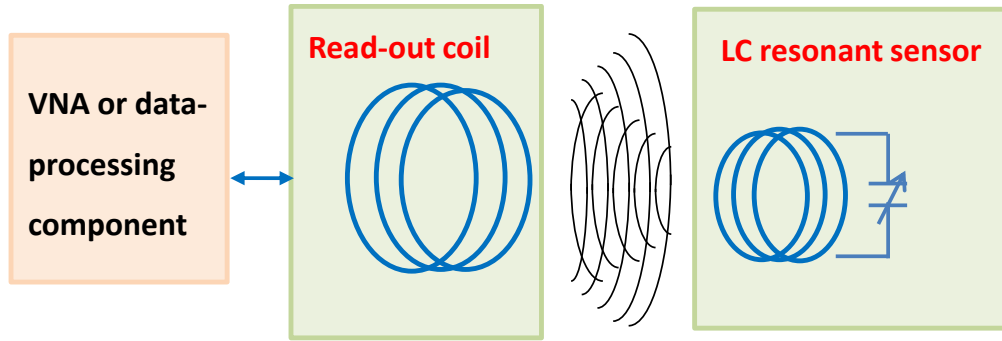


Figure1.1 Wireless telemetry system with a simplified structure for the measurement of LC resonant sensor

wireless system is consisted of a readout coil and a sensor. The communication between the two components can be achieved through inductive coupling of two coils. Although the proposed wireless sensor system can enable the remote pressure monitoring at certain distance, there are still some limitations that prevent the wide application of wireless sensor systems in medical applications: 1) Range: the telemetry distance of this simplified wireless sensor systems is limited within tens of millimeter range due to the low power density from the reflected electromagnetic field. 2) Sensitivity: the sensor information communicated through inductive coupling is sensitive to the noise and telemetry distance. Some improvements should be implemented to the development of wireless sensor system that is suitable for medical applications.

Based on the working mechanism, a wireless communication system can be divided into two categories: active and passive. In active systems, the varied parameters of sensor information are acquired with the assistance of data-acquisition devices and then wirelessly transmitted to external equipment to be further analyzed or to guide treatment. Wire connections between the sensor and other auxiliary components are always required in active systems, and an extra battery is also desired to supply power for

the operation of controlling circuits [5] which in turn helps to get a large communication range. However, battery packs are suboptimal for longtime implantable applications and may cause additional issues and inconvenience, such as large size and limited battery life. In passive systems, the low data-rate information can be directly obtained and transmitted between the sensor and readout coil through near-field coupling within a short distance. The previously proposed wireless sensor system with a simplified communication structure for the measurement of a sensor is such a passive system that its telemetry distance is small due to the weak coupling between the two coils. Therefore, there is a demand for reliable wireless sensor system that can work in a large communication range without a battery supply and with small dimension for medical applications. There are half-active wireless communication systems that can be alternative solution to satisfy the requirements of a reliable wireless sensor system for medical application. It is associated with battery replacement through wireless power harvesting circuits and wirelessly powered auxiliary data-acquisition circuits to work from a remote distance. Currently the development of wireless power harvesting circuits and wirelessly powered auxiliary data-acquisition circuits have undergone significant improvements in Radio-frequency identification (RFID) systems [5-7] for the purposes of wirelessly identifying and tracking tags attached to objects. Similar to the communication mechanism of RFID systems, the sensor based wireless communication system can respond to the wireless interrogation signal from a reader with real-time physical sensor data. With the highly developed integration levels, it is possible to design a reliable wireless sensor system through a combination of an RFID based wireless communication system with embedded sensors to measure and transmit data. With the integrated data collection circuit and

sensors, this kind of half-active RFID based wireless sensor system can be used to identify patients or pharmaceuticals, or monitor blood preservations in a long communication range. An example of half-active wireless telemetry systems with a combination of RFID system and medical sensor is shown in Figure1.2.

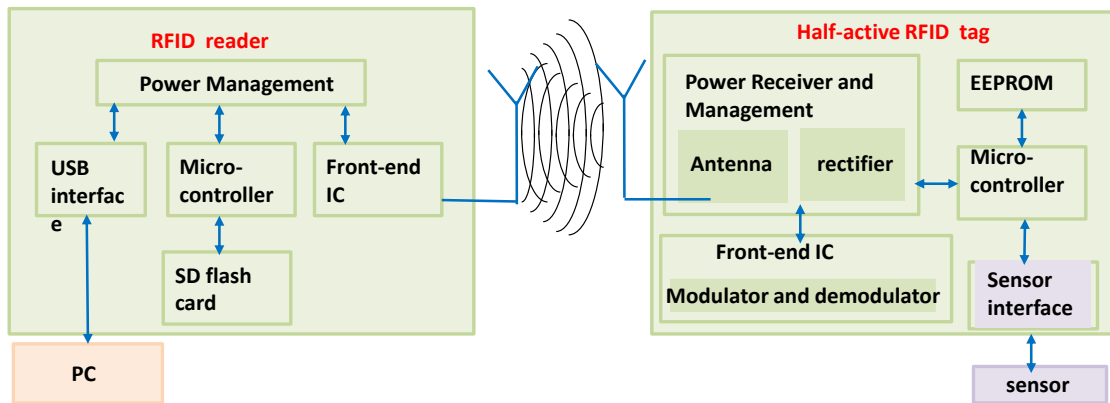


Figure1.2 Half-active RFID based wireless communication system for wireless sensor system

As shown in Figure1.2, with the embedded sensor, the RFID tag acts as the measurement device that is attached or implanted to the object. It contains a coupling element (antenna) and a low-power integrated circuit (IC). The highly integrated circuit is consisted of an analog RF interface, microcontroller, RF-to-dc rectifier, and a sensor interface. Due to the auxiliary circuits required for longer communication range, the number of components in half-active wireless communication system is increased and thus the physical size. The main issue and challenge related to the application of half-active RFID based wireless communication systems in medical systems is how to develop a reliable wireless sensor system with a compact size along with the reliability, feasibility and security in the human body. Further miniaturization on half-active RFID based wireless communication systems is needed.

Despite the progress in semiconductor technology for IC and the considerable increase in the application of ICs in RFID tags, passive components (resistors, capacitors, and inductors, filters, antennas, etc.) are still the major parts of the system and difficult to be miniaturized. Modern wireless communication systems keep stewing its efforts to small scales with more functions. However, passive RF components still occupy a large area and mass fraction of the system. Taking up to 80% of the footprint of transceiver and receiver circuits in wireless communication system, the miniaturization of RF/wireless passive components is the most crucial and urgent problem. Generally the characteristics of the passive RF/wireless components are mainly determined by the electric and magnetic properties of the substrates that are used to support and design these components. The included properties of the substrates are: the permittivity value, permeability value, dielectric loss, magnetic loss, and thermal expansion coefficient of the materials. Based on these features, some approaches such as material-oriented novel substrates, material-related novel component structure, and material-improved novel components are investigated and applied to the miniaturization of passive components.

As one of the most widely used passive RF/wireless components, the antenna serves as a transducer to transmit or receive electromagnetic waves; the antenna's performance is strongly impacted by its physical size. According to the scales of the structure, an antenna can be categorized into two types: resonant antennas (e.g. dipoles, microstrip antenna, etc.) and traveling wave antennas (e.g. spirals, horns, helixes, etc.). Usually a travelling wave antenna has a large dimension ranging from one wavelength to several wavelengths, while the resonant antenna is made according to the physical law requiring the resonant frequency associated with their size comparable to the wavelength.



With the characteristics of low profile, light weight, conformability and easy fabrication on a printed circuit board (PCB), the microstrip patch antenna has advantages over the traveling wave antenna and other resonant antennas but still needs a resonant size close to half wavelength of their resonant frequency. Many methods have been studied and proposed to down-size the patch antenna [8-10]. One approach of minimize the patch antenna is to add extra shorting pins from the metal surface of patch to the ground at different positions, which leads to the development of quarter-wavelength patch antenna called planar Inverted-F Antenna (PIFA) [8]. Generating different types of notches or slots on the surface of the patch antenna is another down-sizing technique which makes use of material-related novel structure to increase the electrical path of the antenna to get a compact size [9]. However, these discussed approaches will cause a decrease of electromagnetic performance, therefore a good compromise between size and performance has to be studied. It has been theoretically and experimentally proven that using magneto-dielectric substrates with both high permittivity ( $\epsilon_r$ ) and permeability ( $\mu_r$ ) is an effective solution to design miniaturized antenna with increased bandwidth and improved radiation efficiency [10]. However, there are no natural low-loss magneto-dielectric substrates that can be applied directly to RF components. Research works have been reported and proposed to develop artificial magneto-dielectric substrates such as inserting metallic resonant particles [11], loading split-ring resonators (SRRs) [12], developing electromagnetic band-gap (EBG) structures [13] or using metamaterials with embedded resonant circuits [14]. Unfortunately these introduced structures are either difficult to implement or make the substrate bulky.

Unlike the previously introduced artificial magneto-dielectric substrates, this dissertation proposes a novel magneto-dielectric substrate which is made of a high resistivity silicon substrate embedded with a patterned permalloy (Py) thin film. The high resistivity silicon is highly considered for the design of the substrate as it can support the integration of silicon based RF components with other technologies such as MEMS and semiconductor components. The theoretical and experimental results show that the proposed magneto-dielectric substrate can be successfully used to design miniaturized RF components. Py ( $\text{Ni}_{80}\text{Fe}_{20}$ ) is a kind of ferromagnetic material with high permeability value ranging from 200 to 9000 [15]. Py is promising material for the construction of magneto-dielectric substrates. Ferromagnetic resonance frequency (FMR) is an important factor to determine the operating frequency range of ferromagnetic materials. The permeability of Py is very high and is tunable only when the working frequency is below FMR frequency as opposed to when the working frequency is above FMR frequency, then the permeability becomes very low and is not predictable. The natural ferromagnetic resonant frequency (FMR) of un-patterned Py film is very small and is usually lower than one GHz which is greatly affected by in-plane uniaxial magnetic anisotropy [16]. The operation frequency of RF components is usually above several GHz. Therefore the FMR of a Py thin film should be as large as possible to make it suitable for RF applications. To increase the FMR, Py thin film is selectively patterned with optimized patterns on the surface of the silicon substrate. The effects of Py pattern geometries on permeability and FMR are thus investigated and analyzed in this dissertation.

There is another consideration for the application of half-active RFID based wireless communication systems in the medical micro-system: the impedance of antenna is sensitive to the human environment, which may cause a frequency shift of the devices and result in low efficiency by the sensor system. In addition, modern wireless communication systems have put more and more requirements on multiple functions that work with multi-standards and multi-bands. Therefore, it is very desirable to develop frequency reconfigurable RF components to satisfy the variable working environment and the multi-function based system. With one component working in different frequency bands, frequency reconfigurable components can further reduce the size of a system by decreasing the number of components. Under these requirements many technologies have been investigated and employed to tune the resonant frequency of antennas, filters, diplexers, etc. These approaches include the application of Radio Frequency Microelectromechanical Systems (RF MEMS) based tunable varactors [17], semiconductor varactors [18], electrically tunable varactors with ferroelectric materials [19], and magnetically tunable inductors with ferromagnetic materials [20]. However, the tunability of all the reported approaches is directly dependent on the design of the individual component, which means that each design needs to be oriented with customized fabrication process for different technology. The difficulties in designing the tunable components lie in how to make the tunable approach cost effective, compatible with other technologies and easily fabricated. Therefore, a unique solution to design arbitrary tunable RF components using an engineered substrate with embedded patterned Py thin film is proposed in this dissertation.

Besides the high permeability value that is suitable to design miniaturized components, the permeability of Py thin film can be both adjusted by the external magnetic field and DC current. However, the magnetically tunable components with ferromagnetic materials cannot meet the requirements of a miniaturized wireless communication system when a large and cumbersome external biased magnetic field is required. The proposed engineered substrate embedded with patterned Py thin film has a smart structure that is suitable to design arbitrary tunable RF components with applied DC current. To implement the DC current on the patterned Py film, an array of DC bias lines are specially designed and added to the layout of the previously introduced magneto-dielectric substrate. With a new structure evolved and developed from a magneto-dielectric substrate, the engineered substrate enabled with patterned Py thin film can be implemented with adjusted DC current and is introduced to design arbitrary electrically tunable RF components in this dissertation.

## 1.2 Chapter Outline

In this dissertation, the research work can be divided into two parts. In the first part, the effort is devoted to designing a biomedical pressure sensor with a limited footprint which works at the Medical Implant Communication Service (MICS) band of 402-405 MHz as designated by the Federal Communications Commission (FCC). A wireless sensor system with a simplified structure is introduced to measure a pressure sensor. Considering the limited footprint for the implantable sensor, the optimization approach for modeling and design of inductively coupled wireless sensor system with a Design of Experiments (DOE) is presented. Since the miniaturization of wireless communication system is a very important factor for its applications in medical areas,

down-sizing technologies are studied in the second part of research work. There are two major approaches for the development of a miniaturized wireless communication system. One is utilizing the simplified structure of a system with a small account of components, which has been introduced and applied in the wireless sensor system to quickly measure the pressure sensor in the first part of this research. Although the simplified wireless sensor can have the sensor data directly transmitted between the two inductive coils, it comes with a small telemetry distance and a weak interference-resistance. The other approach to down-sizing the system is to minimize the communication components. Utilizing some compact RF components such as antennas and filters in the RF front end to assist the data acquisition and transmission, the wireless communication system with an improved structure as shown in Figure1.2 can work through stronger interference-resistance and longer telemetry distance. In addition, there are increasing frequency bands for multi-functions, and tunable RF components can be a promising solution to substitute the multi-circuits working in multi-bands, which in turn can further reduce the size of the system by reducing the number of components. The second part of this research work is focus on developing an engineered substrate enabled with patterned Py thin film to design miniaturized and tunable RF components. A novel magneto-dielectric substrate embedded with patterned Py thin film is first introduced to design miniaturized RF components. By implementing the effects of current-dependent permeability of Py thin film, an engineered substrate with a smart structure evolved from the magento-dielectric substrate is developed and presented for developing electrically tunable arbitrary RF components. Based on these two research tasks, the dissertation is organized as follows:

Chapter 2 will introduce the design and optimization of a high-sensitivity pressure sensor for medical applications. The methodology of the optimization on EM models of sensor and sensor system with Design of Experiment (DOE) method is presented. A wireless sensor system with a simplified inductively coupled structure is introduced for the measurement of the sensor. The theoretical and experimental results are analyzed and presented to show the work of the inductively coupled wireless sensor system.

Chapter 3 will presents the RF characteristics of a magneto-dielectric substrate which make it suitable for down-sizing the patch antenna with improved performance. Without a natural low-loss magneto-dielectric material that could be used as substrate directly, a theoretical overview of various approaches for developing an artificial magneto-dielectric substrate are studied and discussed. The patterning method applied on Py thin film is introduced and analyzed to overcome the limitation of FMR of Py film bellow 1 GHz. A novel magneto-dielectric substrate enabled with patterned Py thin film is thus developed to design miniaturized RF components. The performance of the magneto-dielectric substrate is verified by the implementation of patch antenna and a transmission line based phase shifter.

Chapter 4 will discuss the advantages and disadvantages of current widely applied technologies for developing tunable RF components. To implement DC current on Py thin film, a novel engineered substrate with a specially designed structure evolved from magneto-dielectric substrate is introduced for designing arbitrary tunable RF components. The engineered substrate is fabricated with DC magnetron sputtering technology, while the RF components can be fabricated on arbitrary substrates with printed circuit board

(PCB) technology and then bonded to the top of engineered substrate for implementation. The separated fabrication of the engineered substrate and RF components provides a flexible and cost-effective method to develop tunable components. And the performance of an electrically tunable engineered substrate from DC-current dependent permeability is verified by the implementation of several tunable RF components (one-port patch antenna, two-port phase shifter, two-port band-pass filter and three-port band-pass filtering balun). It proves the efficacy of the design concept of implementing arbitrary tunable RF components on an engineered substrate with patterned Py thin films.

Chapter 5 will focus on analyzing the characteristic effects of the engineered substrate. The limitation of the engineered substrate is affected by the bandgap effects from the DC bias line and FMR of patterned Py thin film on the substrate. The operating frequency of the RF components should be designed below a certain frequency to reduce the effects from these two factors. In order to better understand the tuning mechanism of the engineered substrate, the tuning performance of two different types of structure based components are studied and compared. Approaches to improve the performance of devices on the engineered substrate with less current are also introduced.

Chapters 6 firstly gives a summary of contributions to the dissertation and then presents future work to be performed to improve the tunability and application of the engineered substrate.

## CHAPTER 2

### INDUCTIVELY COUPLED WIRELESS SENSOR SYSTEM

#### 2.1 Introduction

There is an increasing demand for reliable sensor systems capable of sensing and measuring interesting data at a remote or inaccessible place. Combined with different electronics, many types of sensors have been developed with different functions such as wearable sensor to monitor muscle exertion [21], biometric skin sensors to record heart rate variability [22], chest sensors to track body's vital signs [23], mouth sensor to measure muscle energy output [24], and smart teeth sensor with learning algorithms to record the behaviors of coughing, smoking, drinking, speaking and breathing [25], etc. The sensor systems are all playing an important role to enhance the quality of life and healthcare outcomes. However, some of them may need direct wire connections between the sensor and data acquisition electronics, or extra power supply from a battery, which makes them not suitable for the long-time application due to their large physical size, limited lifetime and suboptimal of the battery. In addition, it is difficult to use a wired sensing system in some situations like implantable devices inside the human body [26] or in hermetic environments [27]. Therefore, there is a motivation for developing a wireless sensor system suitable for implantation that can monitor and read the information by returning a 'telemetry' of the interested parameters.



Wireless sensor system is a type of wireless telemetry technique that works by measuring objects and collecting data at remote place without contacting [28]. With the advantages of the real-time monitor, cableless communication, mobility etc., the wireless telemetry technique has been widely used in a variety of fields such as mechanical, chemical or medical application [29-31]. Reference [29] reported a wireless sensor system to monitor turbine engines in high temperatures. Two similar planar spiral inductors with distributed capacitance which serve as a transmitter and receiver respectively are designed to monitor the intraocular pressure wirelessly [30]. A battery-free telemetry system for on-chip pressure sensor measurement is offered in [31]. Among all of the reported wireless sensor systems, the sensors are operating around a relative low frequency range with several or tens of MHz and a large dimension. Therefore, it is relative easy to design a telemetry system with high-quality factor Q which affects the sensitivity of the telemetry system. It is difficult to design a sensor based wireless telemetry systems with compact size and reliable performance at ISM band (402-405MHz).

Congenital heart defects (CHDs) is a chronic condition in which the heart cannot pump blood as well as it should. The associated surgery for this disease requires an immediate intervention to palliate or correct the condition at some point during a person's early lifetime [11-12]. Presently, intra-cardiac pressures in patients are monitored by fluid-filled catheters that traverse the walls of the heart and the body to an external transducer [23-24]. This technique carries with it significant risk of bleeding, infection, and malfunction. There is a critical need to develop medical devices that allow direct and long-term physiological intra-cardiac monitoring and presents little or no bleeding and

infection risks. Recently significant researches have been devoted into the development of a chronic implantable intra-cardiac pressure monitoring system [25-27]. The reported devices generally utilize the principle of passive wireless telemetry that relies on an antenna or an inductively coupled coil to communicate with an implantable sensor to monitor the patients. Little work has been done to optimize the performance of implantable sensor system. To improve the established surgical and delivery method, Chow et al. designed an active fully wireless implantable cardiovascular pressure sensor [28]. An active system is suboptimal for longtime implant applications due to the requirement of an external power supply for data processing circuits. Inductively coupled passive devices, with advantages in safe long-term implanting, structural simplicity, small fabrication footprint and low-cost production, are preferred in chronic intra-cardiac pressure monitoring.

In this chapter, optimization techniques for modeling and design of inductively coupled wireless bio-pressure sensor system under certain design requirements is presented. With recent advances in MEMS and semiconductor technology, the micro-fabricated bio-pressure sensor can be produced as a miniaturized LC resonant circuit and featured with a pressure-dependent capacitance to enable noncontact pressure sensing through inductive coupling between two coils. To make it implantable, the bio-pressure sensor should have a sufficiently small size within the footprint of  $3.2 \text{ mm} \times 3.2 \text{ mm}$  and operate in the Medical Implant Communication Service (MICS) band of 402-405 MHz as designated by the Federal Communications Commission (FCC).

## 2.2 Design and Optimization of Pressure Sensor

Pressure sensor has been widely used in medical applications for sensing and monitoring health conditions. Generally there are two typical pressure sensors: capacitance-based (CB) or resistance-based (RB) sensors. CB sensors can perform with high sensitivity, high resolution and bio-compatibility [33]. However, the complicated 3D structure and high-cost fabrication processes of the CB pressure sensor are obstacles for biomedical application. Although with a simple structure and easy fabrication, the resistance change of RB pressure sensor resulting from the mechanical deformation of material is still difficult to minimize [34], and few resistance-based (RB) pressure sensors are reported.

### 2.2.1 RB Pressure Sensor

A metal RB sensor using Au coated PDMS thin membrane have been initially designed from our collaborator's research in Virginia Commonwealth University as the schematic of the structure of the pressure sensor structure shown in Figure 2.1. Pressure

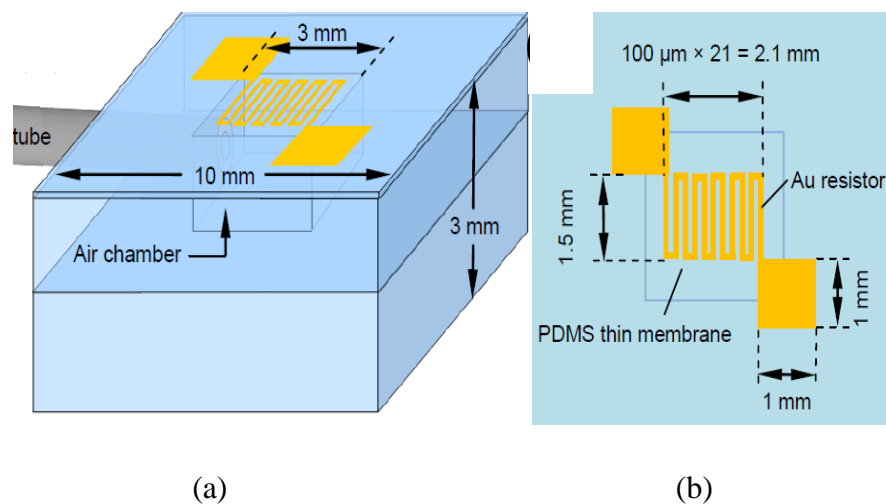


Figure 2.1 (a) 3D view of RB sensor (b) Top view of RB sensor [34]

induced membrane deformation was transduced through a resistive detection technique to produce quantitative measurement of absolute pressure. The strain-induced resistivity of the metal thin film on the RB sensor is changed by the micro-cracks on the surface of Au. And the sensitivity of the pressure sensor is proportional to the density of cracks, the average width and length of the cracks are inversely proportional to the thickness of the residual layer. Although the introduced micro-cracks based RB pressure sensor performs with high linearity in the sensing range, the structure of RB pressure sensor is not suitable for integration with other electronics, and the RB pressure sensor is difficult to apply in the wireless sensor system with a simplified communication system consisted of two inductively coupled coils.

### 2.2.2 Resonant Pressure Sensor

When compared to the RB sensor, the CB pressure sensor is preferred due to its low power consumption, low temperature drift and good long-term stability [36]. Because of the good performance of Au film pattern on a polydimethylsiloxane (PDMS) membrane exhibited from the previously introduced RB pressure sensor [33], a new CB pressure sensor with improved configuration is designed and evolved from the introduced RB pressure sensor using the same thin membrane and air chamber based on silicon substrate.

In order to develop a CB pressure sensor that is easy for measurement and suitable for integration with other electronics, the proposed CB pressure sensor is fabricated as a passive resonant circuit using MEMS technology. The stacking configurations of the components and the deformable surface layer using Au film patterned on a polydimethylsiloxane (PDMS) membrane are the same as the previously

described RB pressure sensor. This proposed resonant CB pressure sensor therefore operates as LC resonant circuit consisted of a planar spiral inductor and a serial MEMS based variable capacitors.

*Configuration of resonant CB pressure sensor:*

With a high sensitivity and biocompatibility, polydimethylsiloxane (PDMS) thin film is applied to keep the sensitivity of implantable pressure sensors when the deflection of the PDMS membrane is transduced. As the cross section of the pressure sensor shown in Figure 2.2, the pressure sensor model consists of two parts: an outside planar spiral Au coil serving as an inductor and a middle parallel-metal plates serving as a series capacitor. The SU-8 based frame structure provides the support for a pressure-deformable air chamber underneath the metal plate of capacitor. The SU-8 based frame structure provides the support for a pressure-deformable air chamber underneath the metal plate of capacitor.

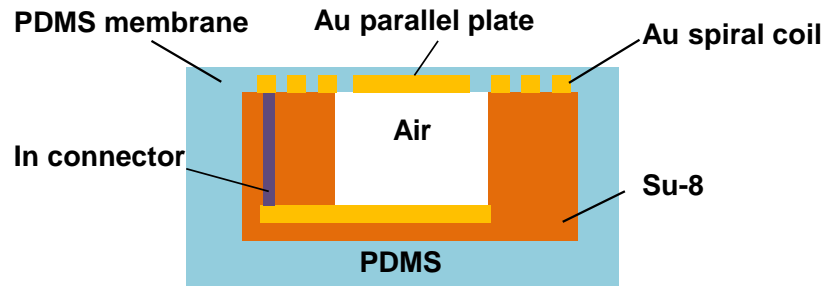


Figure 2.2 Cross-section view of the construction of bio-pressure sensor.

To make it implantable, the whole sensor is encapsulated with a thin layer of bio-compatible PDMS membrane to isolate the sensor from the bio-tissue environment. When the external force is applied, the Au coil will deform into the air chamber, and the capacitance of the sensor is changed. For thin-film Au, when a large strain is applied on the thin film, there is not enough room to deform in the thickness direction. The micro-

cracks which come from the imperfection of grain boundaries might be created in the metal film to compensate for the large deformation. There is a layer of metal residual at the bottom of the cracks, therefore, the Au film is still conducting. There is a trade-off between the sensitivity of micro-cracks and limited pressure which is determined by the thickness of the PDMS membrane. Therefore, the sensitivity of the sensor can be optimized by changing the thickness of the flexible PDMS membrane and the layout of thin Au film based inductor.

### 2.2.3 Characterization of Resonant Sensor

The inductor of the pressure sensor plays an important role in determining the quality factor (Q), resonant frequency ( $f_r$ ) of the sensor and serves as a transmitter in the inductively coupled wireless telemetry system.

#### 2.2.3.1 Inductance of Resonant Sensor

The equivalent circuit model of the LC resonant sensor with a pressure-dependent capacitor on a silicon substrate is characterized with the lumped elements shown in Figure 2.3. In the circuit model,  $L_s$  is the planar spiral inductance of sensor;  $R_s$  is the series resistance of the spiral inductor;  $C_s$  is a series pressure-dependent capacitance;  $C_{ox1}$  and  $C_{ox2}$  are contributed from the parasitic coupling between the planar spiral wires and the loss of silicon substrate;  $R_{si1}$ ,  $C_{si1}$ ,  $R_{si2}$  and  $C_{si2}$  accounts for the parasitic effects of the substrate. As the lumped elements described in the circuit model, there is some parasitic capacitance in the sensor model which can affect the performance of the sensor. The effects of the parasitic capacitance increase as the operating frequency increases. The spiral inductor behaves like a capacitor after the frequency passes the self-resonant frequency (SRF). The inductor must be used below the SRF to guarantee the

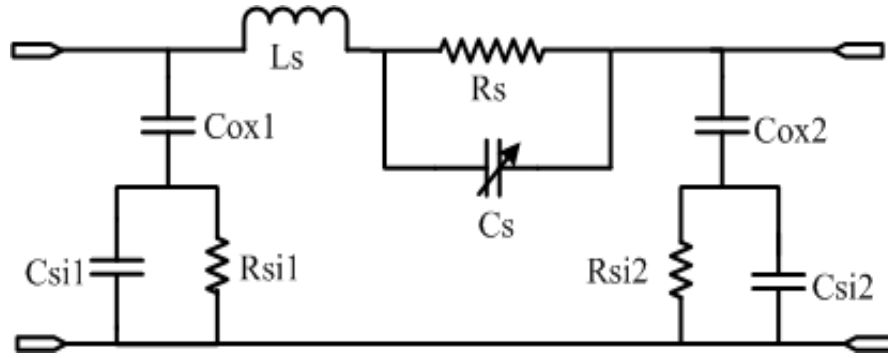


Figure2.3 Equivalent circuit model of resonant sensor with variable pressure-dependent capacitor on silicon substrate

performance, and the SRF can be calculated from the S parameter. The point at which the imaginary part of impedance goes to zero is the SRF of the inductor.

Usually the inductor can be used in a circuit with two modes: one-port mode or two-port mode; different methods are also applied to extract its value. In one-port mode, the inductor is grounded in the circuit and the value can be expressed with following equation [37]

$$L = \frac{Im(\frac{1}{Y_{11}})}{2\pi f} \quad (2.1)$$

This one-port equation includes the parasitic effects from the substrate. When used in two-port mode, there is one end floating in the circuits and the extracted value can be expressed as [38]

$$L = \frac{Im(\frac{1}{Y_{21}})}{2\pi f} \quad (2.2)$$

Without the parasitic effects from the substrate, this two-mode equation has a larger SRF value than that of the one-mode. Regardless of the operation mode, the effective inductor should work at the frequency below its SRF. When designing the proposed resonant

pressure sensor, the inductor of sensor should be designed to make sure that the inductor of sensor used at resonant frequency is far away from the SRF.

### 2.2.3.2 Quality Factor (Q)

The quality factor is a dimensionless parameter that measures the energy loss of a system and has a peak value at the resonant frequency. A large quality factor corresponds to a narrow bandwidth which is desirable in a wireless sensor system. With a narrow bandwidth, the resonant response of the sensor is more narrowly peaked around the resonant frequency and thus can be more easily captured. In the series resonant circuit, the definition of quality factor is expressed as the ratio of the inductive reactance to the resistance.

$$Q_{ind} = \frac{\omega L_s}{R_s} \quad (2.3)$$

where  $\omega$ ,  $L_s$  and  $R_s$  are the angular frequency ( $\omega=2\pi f$ ), inductance and the resistance. It indicates that a high quality factor Q can be achieved by increasing the inductance of the resonant sensor and decreasing the series resistance. However, the parasitic resistance  $R_s$  is increased with the increased physical dimensions of the inductor when more turns are added. Optimization is always required. At low frequency the resistance  $R_s$  could be treated as a constant value given by

$$R_s = \frac{l}{\sigma W t} \quad (2.4)$$

where  $\sigma$  is the conductivity,  $l$  is the length,  $W$  and  $t$  represents the metal width and thickness of metal. However, at high frequency the skin effect will reduce the conducting area of the current [39], which make the series resistance a function of frequency

$$R_s = \frac{\rho l}{W \delta (1 - e^{-\frac{t}{\delta}})} \quad (2.5)$$



where  $\delta$  is the skin depth, defined as

$$\delta = \sqrt{\frac{1}{\pi f \mu \sigma}} \quad (2.6)$$

However, in most conditions the value of the lumped elements cannot be easily determined which make it difficult to calculate the quality factor. Design and optimization of the resonant sensor with EM models in HFSS is a more convenient way to derive the quality factor with Y parameters from simulation results.

$$Q_{ind} = \frac{Im(\frac{1}{Y_{11}})}{Re(\frac{1}{Y_{11}})} \quad (2.7)$$

The quality factor of a planar spiral inductor increases with the frequency first, and then decreases by the high resistance loss due to the skin effect. Optimization on interested parameters to obtain the maximum quality factor at desired working frequency is necessary.

### 2.2.3.3 Resonant Frequency of Sensor

Resonant frequency of the pressure sensor is mainly determined by the planar spiral inductor coil and series connected pressure-dependent capacitor. Without including the parasitic effects from the wire traces and substrate, the resonant frequency of the sensor can be roughly expressed as

$$f_r = \frac{1}{2\pi\sqrt{L_s C_s}} \quad (2.8)$$

The varied capacitance with different applied pressure leads to a change in resonant frequency  $f_r$ . With limited footprint and working band (402-405MHz), the outside area of planar spiral Au wire for inductor and middle part for capacitor need to be optimized to have the sensor work with best performance at resonant frequency.

#### 2.2.4 Optimization Methodology

According to the introduction in the previous section, the pressure sensor consists of an inductor and a series connected capacitor. The configuration of these two elements can be respectively described with the two structures in the configuration of the sensor: the outside area for planar spiral Au wires and middle part for parallel metal plates. As the quality factor expressed in equation (2.3), it is expected to design the resonant sensor with large inductance value for high quality factor. However the parasitic resistance may also increase as the spiral turns and physical area for more spiral Au wires increase. Therefore a large inductor may have a small quality factor due to the increased parasitic resistance. In addition more parasitic capacitance among the adjacent spiral trace wires is added to the inductor resulting in a lower SRF. The analysis of the characteristics of the sensor offers basic knowledge for the optimization of inductance within a limited footprint. All the parameters can be identified and derived from the S parameters of 3D EM models in ANSYS HFSS. The methodology of design and optimization is implemented with the process shown in Figure 2.4.

The target of the optimization is to maximize the performance of the sensor at the desired working frequency of 402MHz in a limited footprint of 3.2 mm by 3.2 mm. The minimum trace width is defined with 25  $\mu\text{m}$  due to the limitation of fabrication. The inductor of the sensor is modeled with the outside planar spiral Au coil and optimized to make sure that the quality factor gets a peak value at or near the target frequency. The optimization process on the model of the outside coil on mutually related geometrical parameters such as trace width, trace gap, trace turns and inner diameter of the coil is repeated until the maximum quality factor is obtained around the desired frequency of

402 MHz The middle parallel-metal plate is then added as the series capacitor of the sensor. The LC resonant circuit based bio-pressure sensor thus can be fully modeled. According to the theory of series resonant circuits [35], the transmission coefficient  $S_{12}$  of the sensor model is expected to have a peak value at its resonant frequency. According to the optimization process shown in Figure 2.4, there are two optimized sensors satisfying the design requirements with optimized performance: one has a relative small inductance and large capacitance; the other has a large inductance but small capacitance.

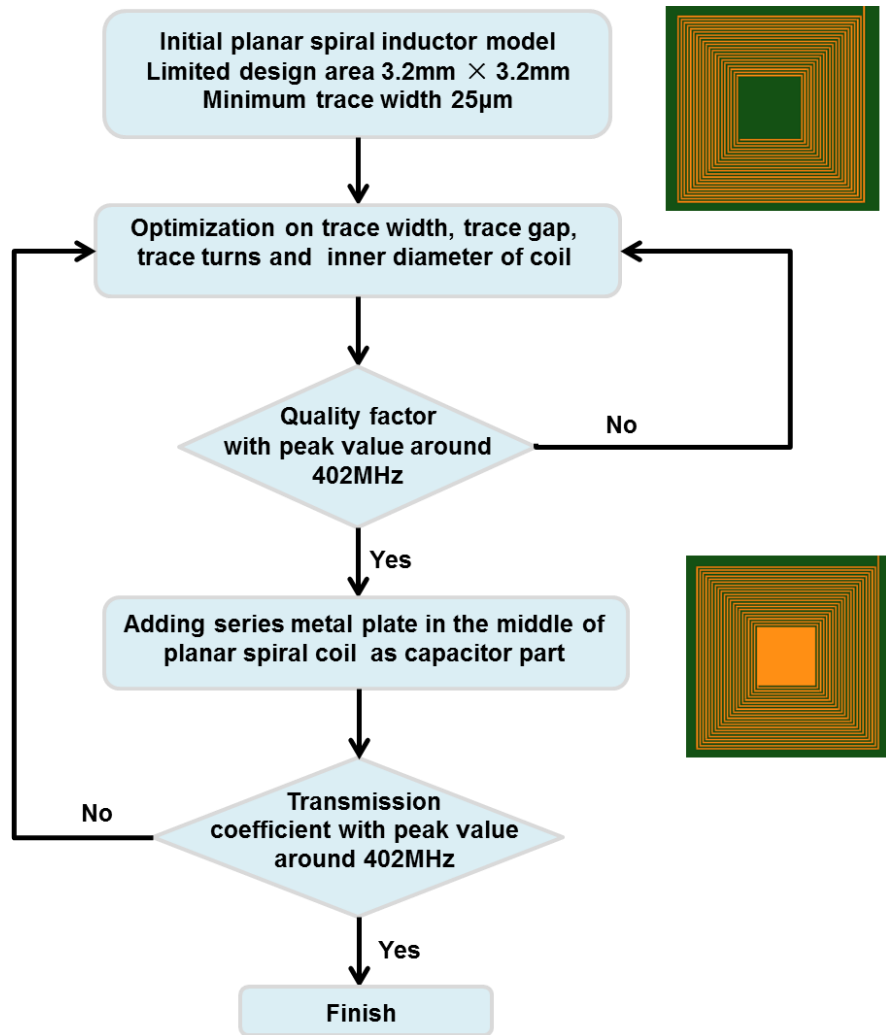


Figure 2.4 Optimization methodology of resonant sensor with EM structure

## 2.2.5 Lumped Elements of Optimized Resonant Pressure Sensor

The size of resonant pressure sensor has a large effect on its performance. With the limited footprint, there are two optimized sensors satisfying the requirements. The top views of the two optimized dimensions are shown in Figure 2.5 (a) and Figure 2.5(b) respectively with a cross-section view shown in Figure 2.5(c).

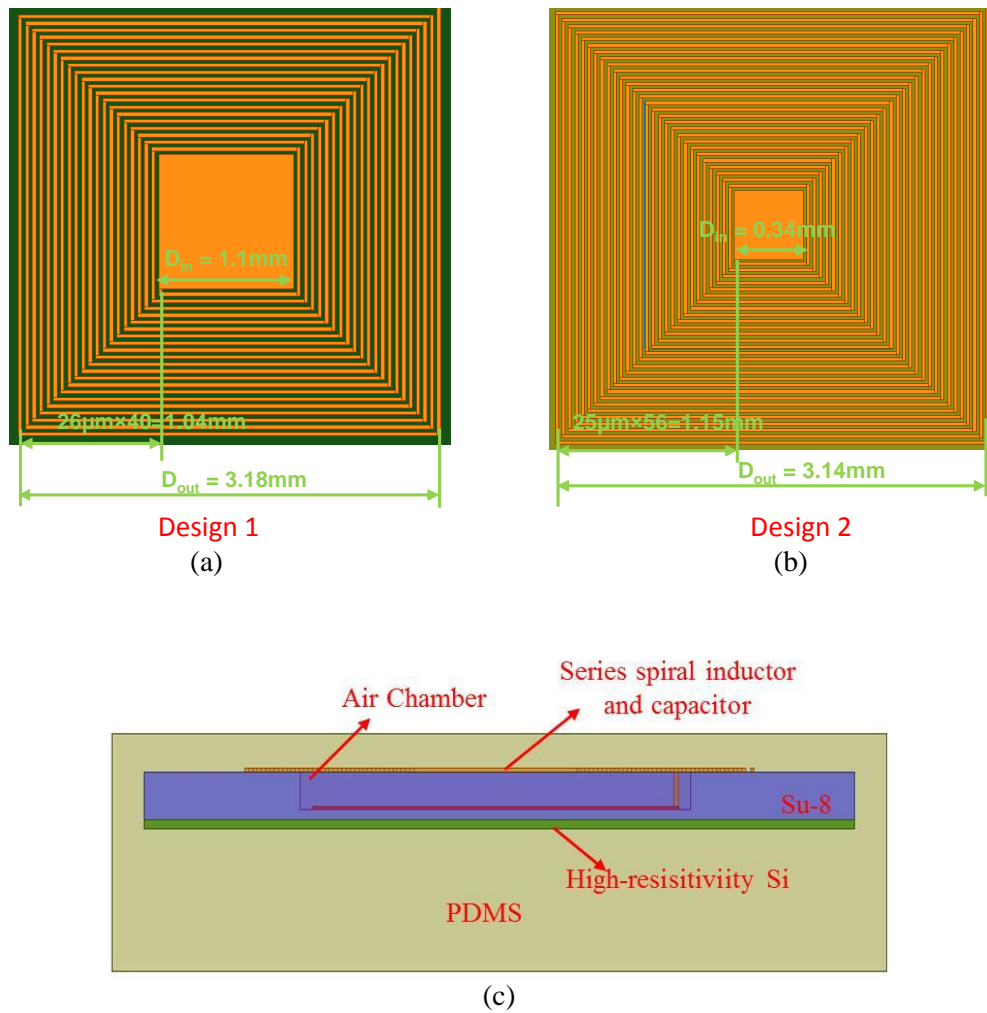


Figure 2.5 Top view of optimized dimension of resonant pressure sensor for (a) Design 1 (b) Design 2 (c) Cross-section view of optimized resonant pressure sensor

As shown in Figure 2.5, design 1 has a relatively larger capacitance with less coil turns for inductor, and design 2 has a larger inductance but smaller capacitance. Both designs have an optimized resonant frequency around 402MHz. To better understand the effects of different inductance and capacitance on the performance of pressure sensor, a simplified equivalent schematic model for the sensor is created in ADS as shown in Figure 2.6.

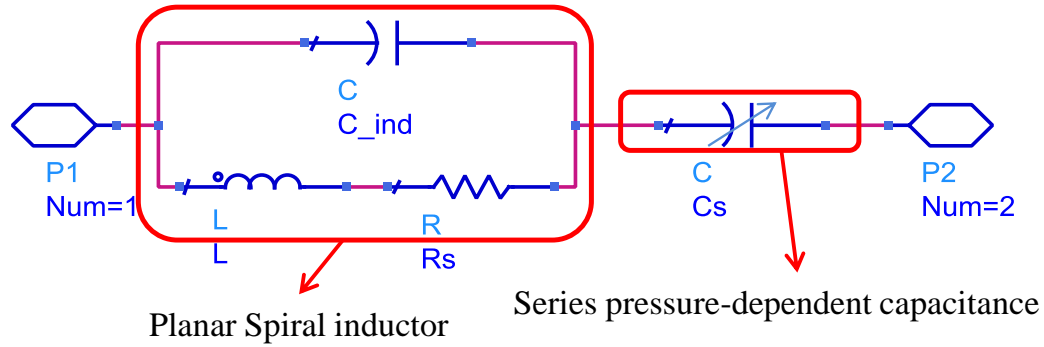


Figure 2.6 Optimized quality factor Q of planar inductor coil

The configuration of the planar spiral Au wires is represented by an inductor with a series resistance and a parallel capacitor. The middle metal plate of the sensor is represented by a variable capacitor. According to the circuit model, the admittance of the planar spiral Au wires and impedance of the structure of resonant sensor could be separately expressed as

$$Y_{ind}(\omega) = j\omega C + \frac{1}{R_s + j\omega L_s} \quad (2.9)$$

$$Z_s(\omega) = \frac{R_s + j\omega L_s}{1 + j\omega C R_s - \omega^2 C L_s} + \frac{1}{1 + j\omega C_s} \quad (2.10)$$

At very low frequency range, the admittance and impedance can be roughly simplified as

$$Y_{ind}(\omega) = \frac{1}{R_s + j\omega L_s} \quad (2.11)$$

$$Z_s(\omega) = \frac{1}{1+j\omega C_s} \quad (2.12)$$

Thus the inductance of the planar spiral coil can be roughly derived from the following equation at very low frequency range

$$L_s(\omega) = \frac{1}{\omega * Im(Y_{ind}(\omega))} \quad (2.13)$$

And the capacitance of the series LC resonant sensor at very low frequency can be roughly calculated with

$$C_s(\omega) = \frac{1}{\omega * Im(Z_s(\omega))} \quad (2.14)$$

### 2.3 Modeling Analysis of Resonant Pressure Sensor

The characteristics of the resonant sensor can be derived or calculated from the simulation of EM models in HFSS.

#### 2.3.1 Simulation of Optimized Sensor

For a series LC circuit, maximum power can be transmitted from port 1 to port 2 at the resonant frequency where is reflected as the maximum transmission coefficient. The optimized transmission coefficient  $S_{21}$  of sensor as a function of the frequency is shown in Figure2.7 (a). It shows that the insertion loss of design 1 is around -4dB at the resonant frequency of 402MHz while the insertion loss of design 2 is around -8dB at resonant frequency of 402MHz. The insertion of design 2 is larger than that of design 1 due to the higher series resistance from the longer trace wires. According to equation (2.14), the simulated capacitance of the sensor can be roughly calculated as a function of frequency shown in Figure2.7 (b). The capacitance of design 1 at lower frequency range has a relative stable value and the estimated capacitance at 402MHz is 0.4952 pF. The

capacitance of design 2 at 402MHz is 0.238pF which is smaller than that of design 1 due to the smaller metal area.

To obtain a high sensitivity sensor, the inductor of the sensor is expected to work best at the resonant frequency. The optimized inductor of the resonant sensors thus have the maximum quality factor  $Q$  centered at 402MHz as shown in Figure 2.8 (a). The optimized quality factor of the inductor from the planar spiral coil for design 1 has a peak value of 17.2 around 402MHz while capacitance for design 2 has a peak value of 14 which is smaller than that of design 1 due to larger resistance loss from longer trace wires. As shown in Figure 2.8 (a), at low frequency range, the quality factor increase proportional to the frequency with a constant low-frequency resistance. As the frequency increases, the resistance of the inductor becomes a complex function of frequency as the expression in equation (2.4) due to skin effects. After the peak value, the quality factor begins to reduce with the increased frequency. The last optimized and calculated inductance from the planar spiral coil of the resonant pressure sensor is shown in Figure 2.8 (b). It shows that the effective inductance value at low frequencies can be treated as a constant value and the estimated inductance of design 1 is 0.33 $\mu$ H around the resonant frequency of the sensor while the inductance of design 2 is estimated as 0.683 $\mu$ H. The SRF of the optimized inductor for design 1 is around 800MHz which is far away from the operating frequency of the resonant sensor while the SRF for design 2 is around 740 MHz.

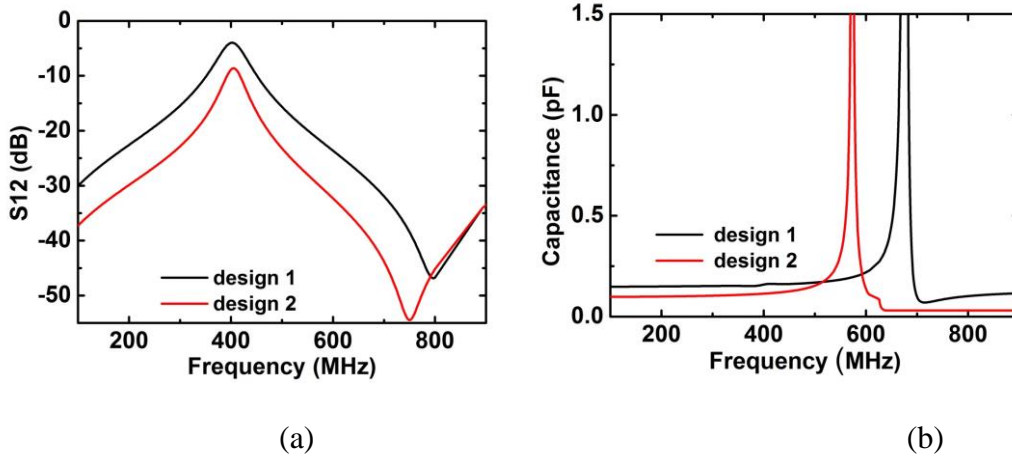


Figure 2.7 (a) Transmission coefficient of  $S_{21}$  as a function of frequency (b) Calculated capacitance as a function of frequency.

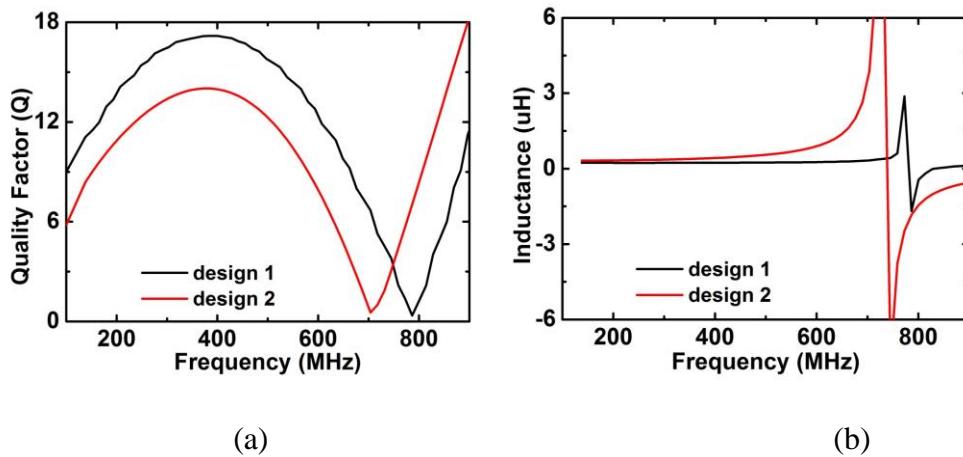


Figure 2.8 (a) Quality factor of the inductor derived from the planar spiral coil of resonant pressure sensor (b) Calculated inductance from the planar spiral coil of resonant pressure sensor

According to the equation (2.8), the resonant frequency of the sensor for design 1 and design 2 can be roughly calculated from the derived inductance and capacitance is 395MHz and 396MHz, which are close to the simulated resonant frequency of 402MHz.



The optimized geometrical parameters and derived characteristics of two designs are summarized in Table 2.1.

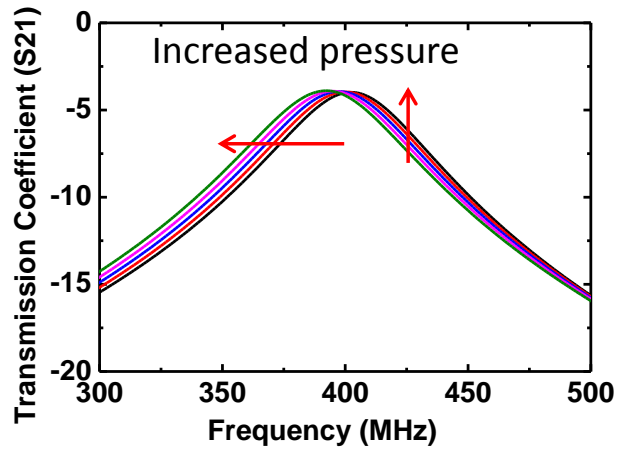
Table 2.1 Summary of optimized Sensors

Geometry Parameters and derived factors	Design 1	Design 2
Size	3.18mm×3.18mm	3.14mm×3.14mm
Number of turns	20	28
Trace width	26μm	25μm
Trace gap	26μm	25μm
Inner diameter	1.1mm	0.34mm
Quality factor (Q)	17	14
Inductance ( $L_s$ )	0.33μH	0.638μH
Capacitance ( $C_s$ )	0.4952 pF	0.238pF
Insertion loss (S12)	-4dB	-8dB

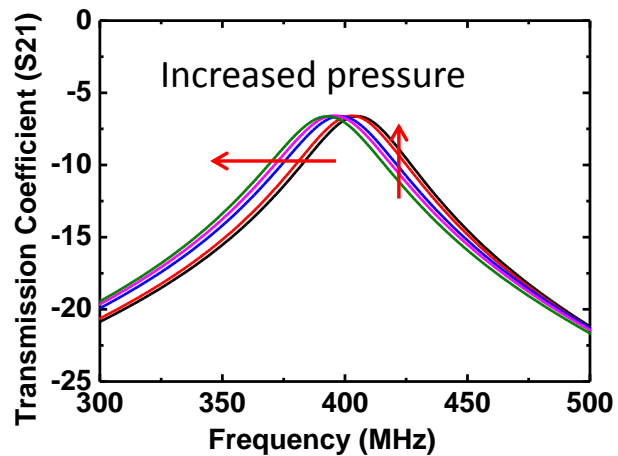
### 2.3.2 Analysis of Pressure Sensitivity of Two Designs

The sensitivity of the sensor to the change of pressure can be simulated by the deformation of the air chamber in the configuration of the sensor. The height of the air chamber is changed gradually from 200um to 180um with an increased step of 5um, and the resonant frequency of the sensor is thus changed with the different height of the air chamber due to the change of capacitance. The shifted resonant frequency of the two designs to the change of the air chamber is shown in Figure2.9 (a) and Figure2.9 (b) respectively. It shows that the resonant frequency of sensor for design 1 can shift from

402MHz to 393MHz, while the resonant frequency of sensor for design 2 can shift from 402MHz to 395MHz when the air chamber is deformed from 0 $\mu$ m to 20  $\mu$ m. The sensitivity of design 1 to pressure is better than that of design 2 because of the larger capacitance.



(a)



(b)

**Figure 2.9:** Sensitivity of the resonant sensor to the deformation of the air chamber. (a) Frequency shift of resonant sensor for design 1 with gradually deformed air chamber. (b) Frequency shift of resonant sensor for design 2 with gradually deformed air chamber.

## 2.4 Modeling Analysis of Wireless Sensor System

Wireless telemetry technique provides a convenient approach to wireless monitoring of the performance of the wireless sensor system in a remote place without physical contact or wire connection. A simple wireless sensor system can be easily realized with two closely spaced and inductively coupled coils for power and data telemetry. A wireless sensor system with a simplified structure consists of an optimized readout coil and the resonant pressure sensor, which is proposed for quick measurement of the sensor. This section will have a numerical analysis of the operating mechanism of the wireless telemetry link and present the design criteria of the readout coil for the telemetry of resonant sensor.

### 2.4.1 Principle of Inductively Coupled Wireless Sensor System

The principle of inductively coupled wireless sensor system is based on the change of electromagnetic energy between the external readout coil and the inductance of the resonant pressure sensor. From Ampere's law [40] the electromagnetic field, generated by the inductive coil, going through the spiral coil of sensor will induce a current across the sensor. In turn, the induced current on the sensor generates back electromagnetic fields on the readout coil which could be added to the former electromagnetic field of the sensor system. The electromagnetic field can be expressed with the impedance of the system for the measurement purposes. To express the impedance of the wireless sensor system, an equivalent schematic of the circuit model for the proposed wireless sensor system is described in Figure 2.10.

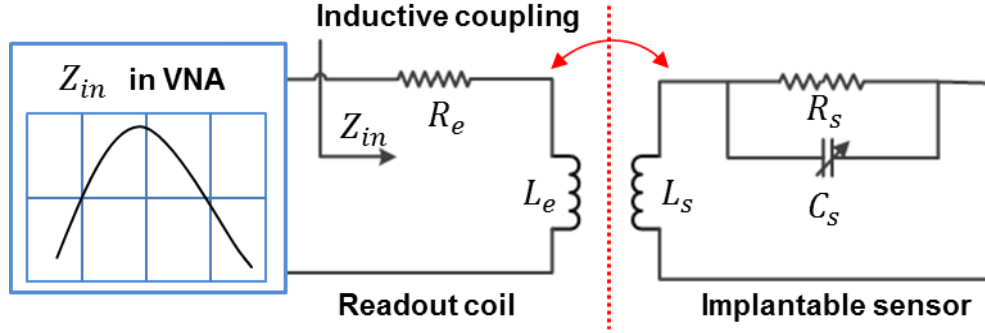


Figure 2.10 Equivalent telemetric circuit model

As shown in Figure 2.10, the external readout coil is represented by an inductor  $L_e$  and a parasitic resistance  $R_e$ . The pressure sensor is consisted of an inductor  $L_s$ , a resistance  $R_s$ , and a tunable capacitance  $C_s$ .  $Z_{in}$  represents the input impedance of the sensor system. Therefore the intrinsic impedance of the readout coil  $Z_e$  and sensor  $Z_s$  can be expressed separately as the function of frequency with following equations.

$$Z_e(\omega) = R_e + j\omega L_e \quad (2.15)$$

$$Z_s(\omega) = j\omega L_s + \frac{R_s}{1+j\omega R_s C_s} \quad (2.16)$$

Due to the inductive coupling between the two inductors, extra reflected impedance from the inductor of the resonant sensor is added to the measured impedance of readout coil, which has been proved in [41]. So the input impedance of the wireless sensor system is

$$Z_{in}(\omega) = R_e + j\omega L_e + \frac{(\omega M)^2}{Z_s(\omega)} \quad (2.17)$$

where  $M = k\sqrt{L_e L_s}$  is the mutual inductance between the readout coil and inductor of the resonant sensor.  $k$  is the coupling coefficient of two coils. Combing equation (2.16) and (2.17), the new input impedance is expressed as

$$Z_{in}(\omega) = R_e + j\omega L_e + \frac{(\omega M)^2 R_s}{(R_s - \omega^2 R_s C_s L_s)^2 + \omega^2 L_s^2} + j \frac{(\omega M)^2 (\omega R_s C_s) (R_s - \omega^2 R_s C_s L_s) - \omega L_s}{(R_s - \omega^2 R_s C_s L_s)^2 + \omega^2 L_s^2} \quad (2.18)$$

It shows that the measured impedance of the wireless sensor system is inversely proportional to the impedance of the sensor. Defining the resonant frequency  $f_0$  is the value at which the real part of the impedance of the wireless telemetry system is at a maximum [42]. Then solving the real part of the equation as following method

$$\frac{dRe(Z_{in}(\omega))}{d\omega} = \frac{d}{d\omega} \left\{ R_e + \frac{(\omega M)^2 R_s}{(R_s - \omega^2 R_s C_s L_s)^2 + \omega^2 L_s^2} \right\} = 0 \quad (2.19)$$

The resonant frequency of the system is derived as

$$f_0 = \frac{1}{2\pi\sqrt{L_s C_s}} \quad (2.20)$$

It also reflects that the capacitance of pressure sensor has the function of resonant frequency.

$$C_s = \frac{1}{L_s(2\pi f_0)^2} \quad (2.21)$$

It means that the real part of input impedance of the wireless sensor system from the readout coil has an induced peak value at the resonant frequency of the sensor. Since the sensor is featured with a pressure-dependent capacitance, the resonant frequency of the sensor is also pressure sensitive. Therefore, it is an effective approach to monitor the real part of the peak impedance from the readout coil to get the pressure-dependent resonant frequency of the sensor.

## 2.4.2 Characterization of Inductively Coupled Wireless Sensor System

The performance of sensor in the wireless sensor system is theoretically analyzed from the inductive sensitivity and pressure sensitivity in this part.

### 2.4.2.1 Inductive Sensitivity of Inductively Coupled Wireless Sensor System

The inductive sensitivity is associated with the inductive efficiency which dictates how much power can be transmitted between the coil of sensor and readout coil.

It represents the signal strength and peak value of the induced input impedance from the readout coil. According to the inductive coupling link in series resonance, the inductive efficiency is defined as the ratio of inductive power transmitted to the implantable coil over the power supplied to the readout coil [43]:

$$\eta = \frac{kQ_e 2\pi f C_s R_s}{(1+k^2 Q_e + 1/Q_s)(2\pi f C_s R_s + 1/Q_s)} \quad (2.22)$$

where  $Q_e$  is the quality factor of the readout coil, and  $Q_s$  is the quality factor of the sensor which can be derived as  $Q_s = 2\pi f L_s / R_s$  in series circuit. In order to achieve the high inductive sensitivity, high quality factor and high inductance from the sensor and the readout coil that is needed. Another approach to increase inductive sensitivity is to increase the coupling coefficient  $k$  which is dependent on the telemetry distance, size and orientation of two inductive coils.

#### 2.4.2.2 Pressure Sensitivity of Inductively Coupled Wireless Sensor System

The pressure response of a bio-pressure sensor is manifested by the resonant frequency as a function of pressure-dependent capacitance. The pressure sensitivity of the bio-pressure sensor can be expressed as the following equation from the previous derivation in [44]

$$S_p = \left. \frac{\partial f_{min}(P=0)}{f_{min}(P)} \right|_{P=0} \frac{\partial P}{\partial P} \quad (2.23)$$

The frequency shift of the induced peak value of input impedance of sensor system is proportional to the change of the square root of the pressure-dependent capacitance, which is described by

$$\frac{f_{min}(P=0)}{f_{min}(P)} = \frac{f_0}{f_0 + \Delta f} = \frac{1}{2\pi\sqrt{L_s C_s}} / \frac{1}{2\pi\sqrt{L_s (C_s + \Delta C_s)}} \rightarrow \frac{\Delta C_s}{C_s} = -2 \frac{\Delta f}{f_0} \quad (2.24)$$

where  $\Delta f$  is the shift in resonant frequency with and without applied pressure. Since the resonant frequency of the pressure sensor is monitored through the peak value of the induced input impedance, it is reasonable to transform  $\Delta f$  into a function of the input impedance. According to the analysis of the equivalent voltage and current in the equivalent circuit of wireless sensor system [45], when the pressure sensor is excited at resonance, the equivalent input impedance  $Z_{eq}(f)$  of system can be simplified as:

$$Z_{eq}(f) = j2\pi f L_e (1 + jk^2 Q_s) \quad (2.25)$$

$$Z_{Re}(f) = 2\pi f L_e k^2 Q_s \quad (2.26)$$

where  $f_0$  is the resonant frequency of the sensor under no pressure and  $f = f_0 + \Delta f$  is the resonant frequency under a applied pressure.  $Z_{Re}(f)$  is the real input impedance  $Z_{eq}(f)$ . The transformed  $\Delta f$  can be further calculated as:

$$\Delta f = \frac{2\pi f}{Q_s} \sqrt{\left(\frac{Z_{Re}(f)}{Z_{Re}(f_0)}\right)^2 - 1} \quad (2.27)$$

The pressure sensitivity is related to the variation of capacitance as

$$|\Delta C_s| = 2 \frac{\Delta f}{f_0} C_s = \frac{4\pi f}{f_0} \frac{C_s}{Q_s} \sqrt{\left(\frac{Z_{Re}(f)}{Z_{Re}(f_0)}\right)^2 - 1} \quad (2.28)$$

The change of pressure is considered to be linear with the shifted resonant frequency of the sensor and the change of capacitance [46]. According to equation (2.28), a large capacitance is desired to achieve good pressure sensitivity. To work in the desired frequency range, a large capacitance will accompany with a small inductance in the confined footprint, which in turn may result in poor inductive sensitivity. It is difficult to have a fully optimized capacitance and inductance in the sensor on mutually related geometrical parameters with the best performance under the design requirements.

### 2.4.3 Modeling of Wireless Sensor System

The inductively coupled wireless telemetry link for the pressure sensor can be modeled and simulated with a readout coil and the sensor as two inductive coils within certain telemetry distance as shown in Figure 2.11. The second coil can be represented by the planar spiral Au wire of the sensor. The primary coil is implemented with a printed spiral coil. To reduce the effects from misalignment and size mismatch, the readout coil is modeled with the same shape of planar spiral Au coil of sensor for each design.

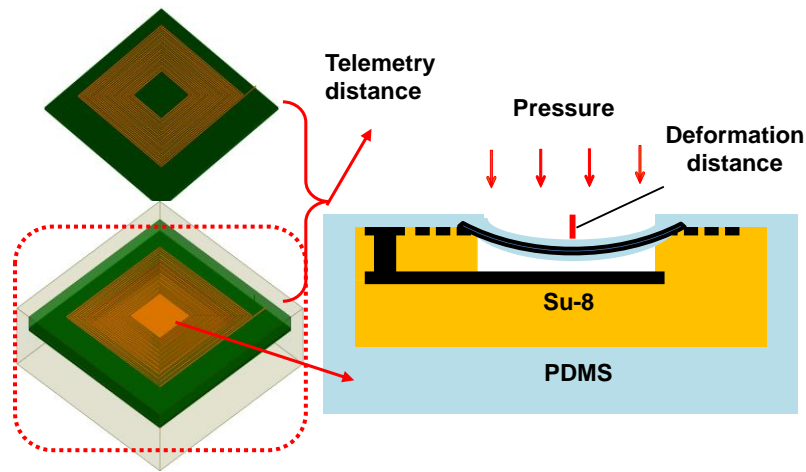


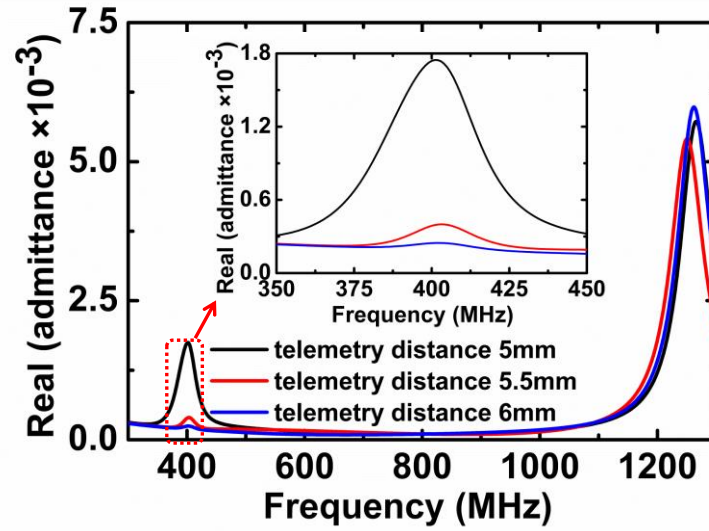
Figure 2.11 EM models of wireless sensor system for the analysis of inductive sensitivity and pressure sensitivity

#### 2.4.3.1 Simulated Inductive Sensitivity of Wireless Sensor System

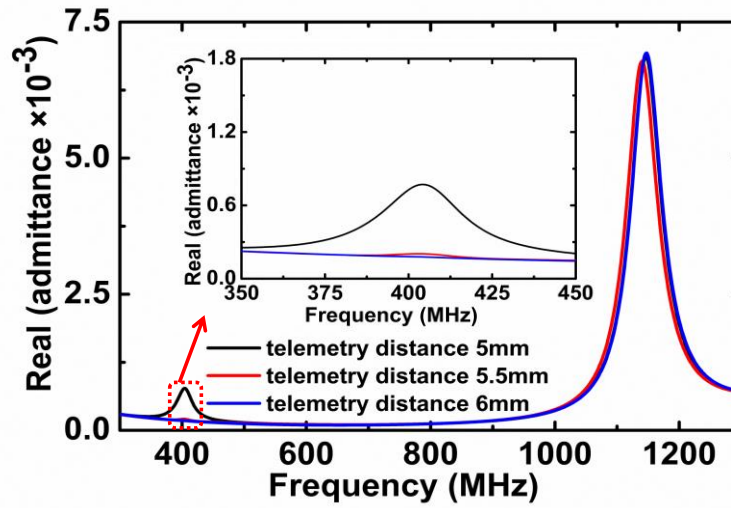
With the aligned readout coil and sensor, the inductive sensitivity of the wireless sensor system can be modeled and evaluated with the change of telemetry distance. According to equation (2.18), (2.19) and (2.20), the resonant frequency of the sensor can be identified from the peak value of induced impedance of the readout coil. Since the readout coil is modeled as a two-port structure with the parasitic capacitance in the



equivalent circuit, the resonant frequency of the sensor is deduced from the peak value of the admittance of readout coil. The simulated admittance of readout coil shows two peak values for the wireless sensor system is shown in Figure 2.12.



(a)



(b)

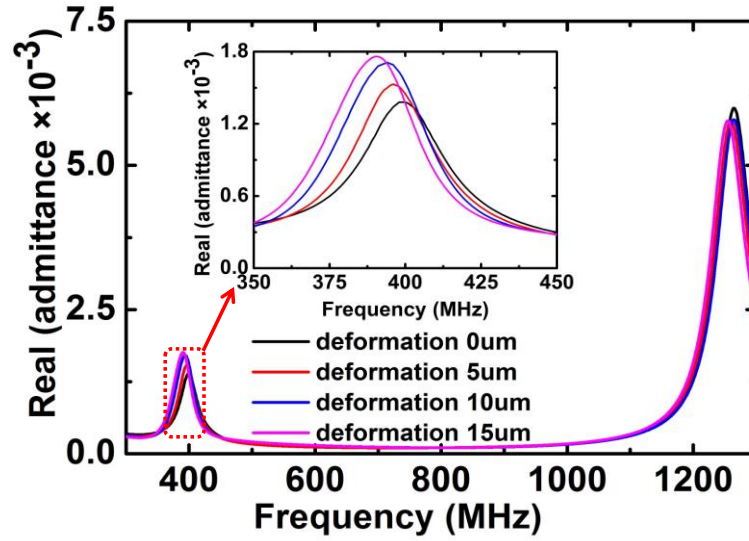
Figure 2.12 Analysis of inductive sensitivity for (a) Design 1 (b) Design 2 at different telemetry distance

The large peak value of admittance represents the SRF of the readout coil, while the small one indicates the induced resonant frequency from the sensor. The magnitude of the induced peak value, representing the strength of inductive sensitivity, is reduced with the increased telemetry distance and stay at the same frequency. It proves that the resonant frequency of sensor can be monitored from the peak value of induced admittance of the readout coil, and is not affected by the telemetry distance. The telemetry distance only affects the inductive sensitivity but not the resonant frequency of the sensor. As the inductive sensitivity of the two designs shown in Figure 2.12, design 1 has a much larger and sharper peak value than that of design 2 when compared at the same telemetry distance. The higher inductive sensitivity for design 1 is consistent with the higher quality factor of design 1 than that of design 2. Although design 2 has larger inductance, the increased inductance in limited footprint results in higher loss from parasitic resistance which in turn reduces the quality factor and increases the insertion loss. Therefore, design 1 shows higher inductive sensitivity than design 2.

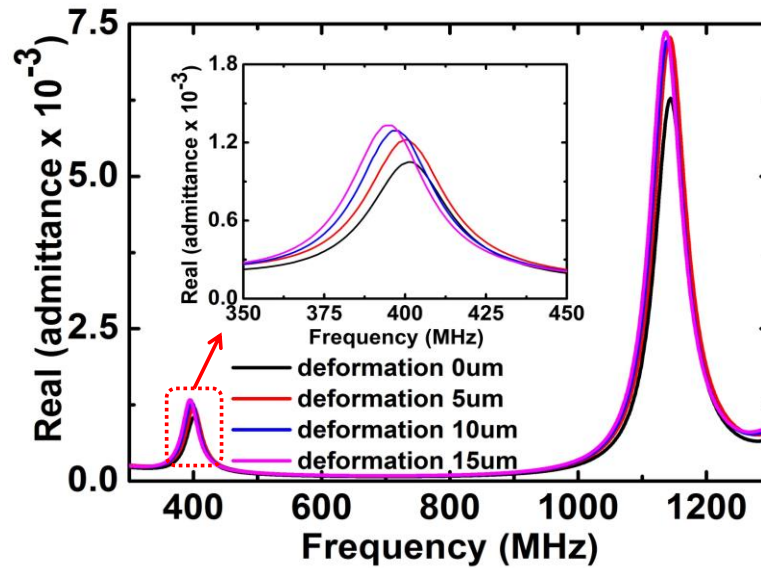
#### 2.4.3.2 Simulated Pressure Sensitivity of Wireless Sensor System

Similar to the inductive sensitivity, the pressure sensitivity of the wireless sensor system can be modeled and imitated with the change of deformation induced on the surface of the sensor by different change in pressure. The simulation of the shifted resonant frequency of the sensor under different pressures with the changed height of the air chamber is shown in Figure 2.13. The results show that the shifted resonant frequency of the sensor can be measured and sensed from the admittance of the primary coil. The measured resonant frequency of design 1 in simulation can shift from 403MHz to 395MHz with the deformation gradually changing from 0  $\mu\text{m}$  to 15  $\mu\text{m}$ , while the

resonant frequency of design 2 shifts from 402 MHz to 396 MHz. It shows that design 1 has larger pressure sensitivity than design 2, which confirms the predicted tendency from (2.28) that the shifted frequency range is larger for the sensor with a larger capacitance.



(a)



(b)

Figure 2.13 Analysis of pressure sensitivity for (a) Design 1 (b) Design 2 with different deformation induced by the pressure

## 2.4.4 Design of Primary Coil

### 2.4.4.1 Rules of Choosing Primary Coil

Spiral wire wound coils, made of filament wires in the form of twisted circular shapes, have been widely used in inductive links for many years. According to the twisted shapes, there are three types of spiral coils: planar, solenoid and toroidal. With the same length of wire, the types of solenoid and toroidal types have larger inductance than that of planar coils, but smaller electromagnetic field outside of the axis of the coils [47]. The solenoid and toroidal coils need to be designed with big dimensions to provide a large electromagnetic field, which in turn reduces the coupling coefficient between the primary coil and the inductor of resonant sensor due to the great difference between the physical dimensions. In addition, it is hard to shrink down the size of solenoid and toroidal coils using the standard micro fabrication techniques with substrates. With accurately defined geometries, the planar spiral coil is the best choice for a good inductive coupling link in the proposed wireless telemetry system when keep relative matched physical geometries.

The on-chip planar spiral coils will suffer from the extra loss and weakened performance from the parasitic effects of the substrates and parasitic capacitance with the ground. Some theories and experiments [48] have proven that planar spiral coils without a substrate can provide a better quality factor  $Q$  than the on-chip ones. As the primary coil of the wireless telemetry system, the desired planar spiral coil should have a self-resonant frequency much higher than the resonant frequency of the sensor. To obtain an induced peak value at resonant frequency of the sensor from the measured results of the primary coil, a narrow bandwidth for high  $Q$  primary coil is needed. Several hand-made

wire-wound coils that can be used as the primary coil of the proposed wireless telemetry system are shown in Figure 2.14. The diameter and the total length of the wires are the variable parameters that can be optimized to get the desired primary coil of wireless telemetry system for the proposed sensor.

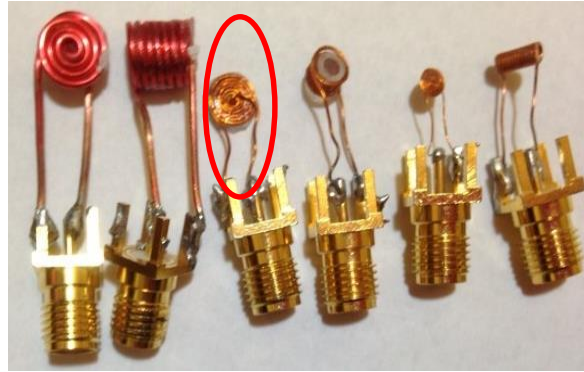


Figure 2.14 Different types of hand-made spiral inductor for measurement

With these hand-made spiral coils, the SRF of the coils could be measured directly from the VNA and the quality factor of coils could be quickly analyzed in MATLAB with the measured results. Therefore, it is more efficient to optimize the hand-made coil from the measurement results than the on-chip ones designed initially from the EM models in HFSS. These hand-made coils can save time needed for simulation and fabrication. The optimization on the primary coil obeys the following rules:

- (1) SRF of the planar spiral coil is mainly determined by the total length of the coil. The longer wire has a bigger inductance and a smaller SRF.
- (2) It is desired to increase the quality factor with large inductors, thus the spiral coil is expected to be designed with longer wire. However, the increased turns of the coil can increase the cross surface of coil which in turn increased the parasitic capacitor. So the length of coil can both affect the SRF and quality factor.

(3) Coil wire with a larger diameter is preferred to reduce the resistance loss and increase the quality factor  $Q$ . However, the thicker wire can easily cause bigger gap between traces which will reduce the mutual inductance among the trace wires. A tradeoff between the diameter and length of coil wire should be considered when designing an inductor with desired value.

(4) The physical dimensions of the primary coil should be similar to the planar coil of the resonant sensor to increase the coupling coefficient of two coils.

Because of the series resistance loss from the trace wire, the quality factor of the planar spiral coil cannot be increased directly with the increased inductor from the increased number of turns. Optimization can be implemented according to the measurement results. The effects of the diameter and total length of coils on the SRF of the primary coil, inductance and the parasitic capacitance is described in following Table 2.2.

Table 2.2 Varied diameter and total length of coils on SRF, inductor and capacitor

<b>Parameters</b>	<b>SRF</b>	<b>L</b>	<b>C</b>	<b>Q</b>
<b>Diameter of wires</b> ↑	↓	↑	↑	—
<b>Length of coils</b> ↑	↑	↓	↓	—

As described in Table 2.2, the changeable tendency of the quality factor cannot be directly predicted from the varied diameter and total length of coils. The highlighted coil in Figure 2.14 is the last optimized one used in the proposed wireless telemetry system.

#### 2.4.4.2 Measurement of Primary Coil

The telemetry distance between the readout coil and the sensor is smaller than the wavelength of the working frequency in the near field [49], which is directly affected by the coil size. The small size of the bio-pressure sensor limits the telemetry distance of the system. The readout coil must therefore be carefully designed to improve the inductive sensitivity with the increased telemetry distance. Serving as a receiver located outside the body, the readout coil can be designed with more flexibility in term of sizes to increase the inductance. However, the inductance of readout coil is only effective below SRF of the readout coil. In other words, even with the flexibility in term of size, the inductance of the readout coil is still subject to the limitation of the SRF. Similar to the optimization of the model of outside coil of the sensor, a planar hand-wound readout coil is optimized on selected factors such as the available diameters of trace wires, the number of turns and the length of trace wires. As the measurement results shown in Figure 2.15, the optimized readout coil has a maximum quality factor of 25 around the resonant frequency of the sensor and an effective inductance of 0.37  $\mu\text{H}$  with SRF of 950 MHz. With the measured S parameters from the VNA, the quality factor and the coil inductance can be calculated from equation (2.7) and (2.13) in MATLAB. The design of the coil is then revised until a maximum quality factor around the resonant frequency of the sensor is achieved. The hand-wound coil provides an efficient approach to build the wireless sensor system with reduced time from simulation to fabrication.

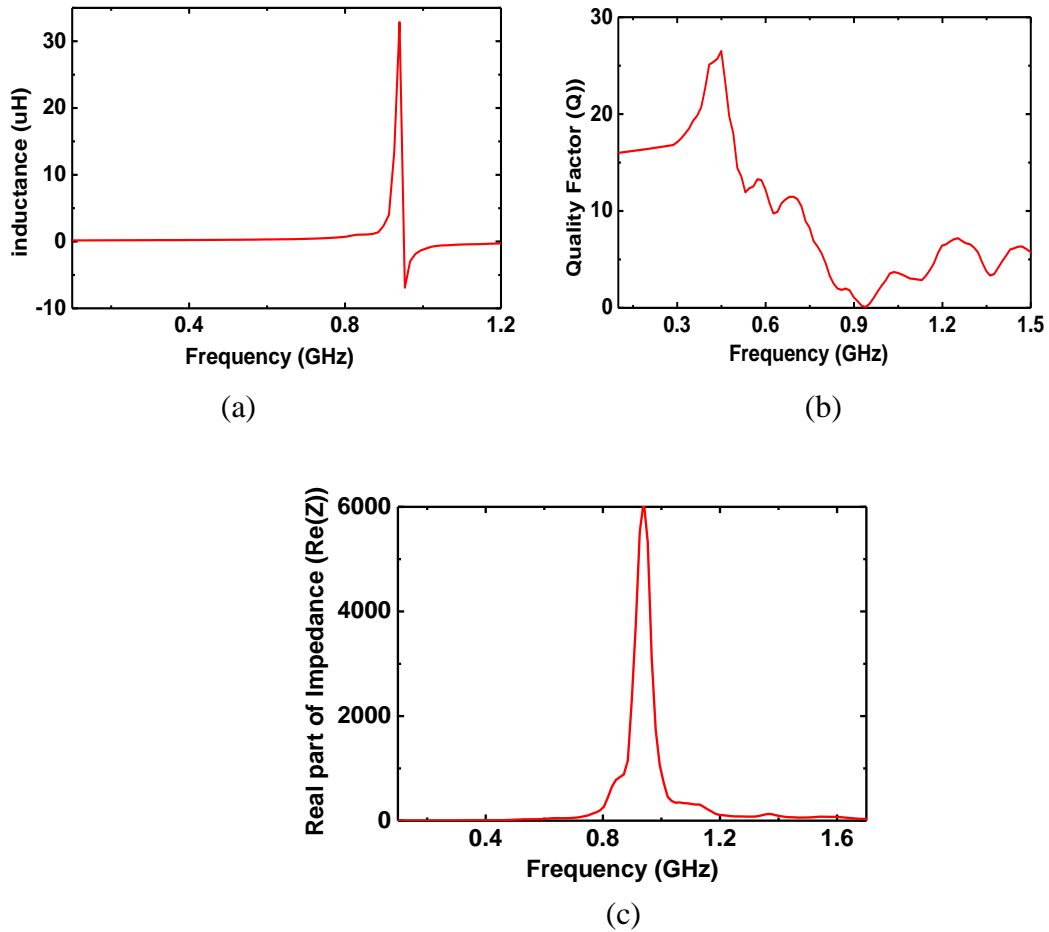


Figure 2.15 (a) Measured inductance of primary coil (b) Measured quality factor of primary coil (c) Measured characteristic impedance of primary coil

## 2.5. Experiment of Wireless Sensor System

According to the previously simulated model of the inductive sensitivity and pressure sensitivity of the resonant sensor for design 1 and design 2, the performance of design 1 is better than that of design 2. Therefore design 1 is chosen and fabricated for the wireless sensor system as in the picture shown in Figure 2.16. With the optimized primary coil and resonant sensor prepared, the setup of wireless sensor system with a simplified structure can be made.





Figure 2.16 Fabricated resonant pressure sensor from design 1

### 2.5.1 Measurement Setup of Wireless Sensor System

Generally the working regions of the wireless sensor system could be divided into three parts: near-field, transition region, and far-field. With selected primary and second coils, the working mechanism of these regions is mainly determined by operating frequency and telemetry distance. The proposed simplified wireless telemetry system works depending on the inductive coupling between the two coils. Thus the interested working range for this wireless telemetry system is near-field which is defined as the one-wavelength range. According to the power efficiency, the near-field region could again be divided into a reactive region and a radiative region. Previous research [49] demonstrated that the reactive region within the distance of  $\lambda/2\pi$  which can provide better power efficiency. To have an effective measurement on the proposed resonant sensor, the primary coil of the telemetry system is expected to be putted at a distance less than 12 cm with the resonant frequency of sensor around 400MHz.

The measurement setup of the wireless telemetry system with an inductively coupled structure is shown in Figure 2.17. The sensor was located inside a specially

designed pressure house with a 10 mm-thick wall and the readout coil is was put on the top surface of the pressure house. The tested telemetry distance is enough for the medical application because of the thickness of the biological tissue is usually less than 10 mm [44]. The applied pressure was provided by a manual pressure pump (3D instruments, LLC.) and monitored by a pressure gauge (Omega, DPG5600B-05G). The frequency response of the sensor is wirelessly interrogated by the readout coil with a port connected to R&S ZVA67 VNA for direct measurements. The measured S parameters from R&S ZVA67 VNA were transformed to Z parameters in MATLAB to get the resonant frequency of the sensor.

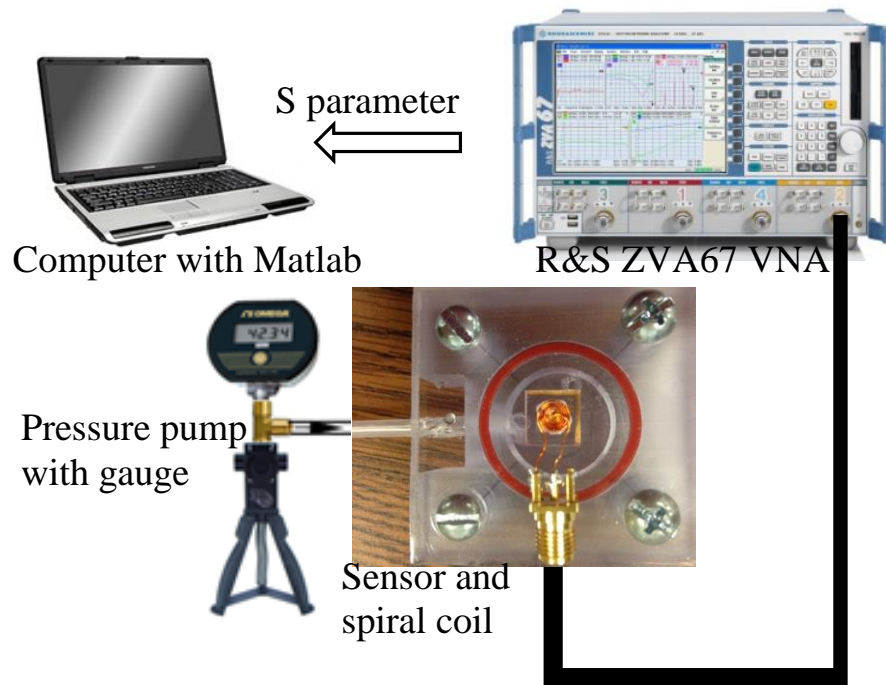
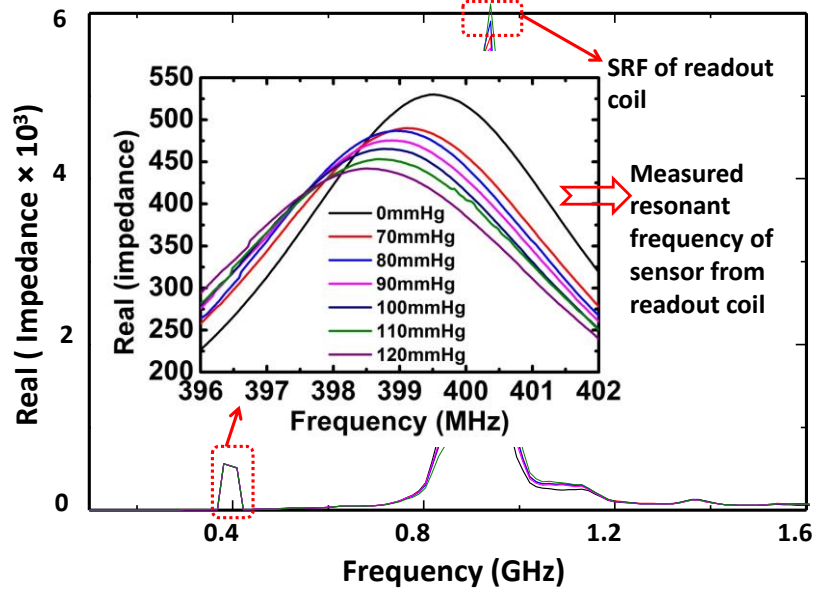


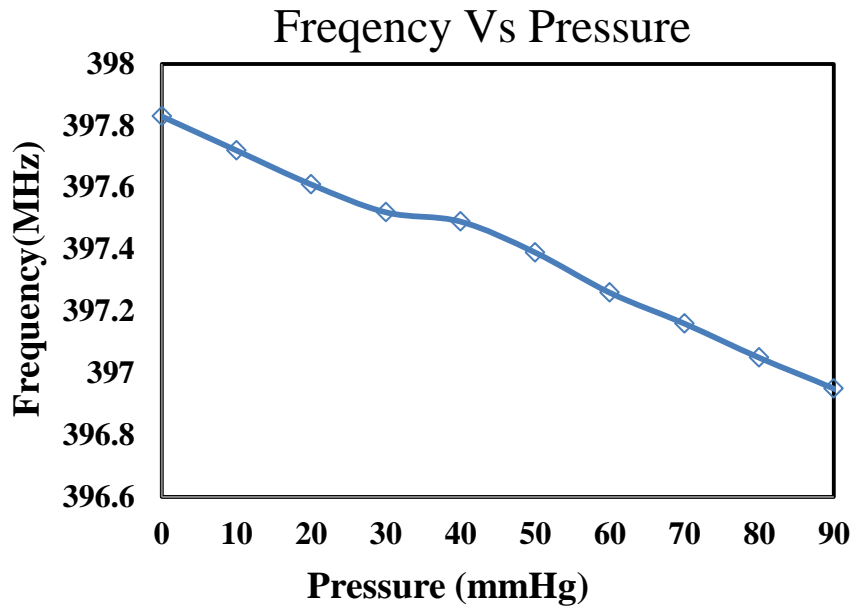
Figure 2.17 Experimental setup of wireless telemetry system for the measurement of resonant pressure sensor

The analyzed measured real impedance of readout coil in the wireless sensor system is shown in Figure 2.18 (a). There are two peak impedance values: one represents the SRF of the readout coil and the other is induced by the sensor at its resonant frequency. The resonant frequency of the sensor is shifted from 399.58 MHz to 398.95 MHz when the applied pressure increases from 0 mm Hg to 120 mm Hg in steps of 10 mm Hg because of the gradually increasing capacitance. The magnitude of the induced impedance becomes smaller and wider as the pressure increases. This is likely due to the decreased quality factor of the sensor caused by the increased capacitance and the increased parasitic resistance.

The response of the pressure sensor has an average pressure sensitivity of 5.3 KHz/mm Hg at a telemetry distance of 10 mm as shown in Figure 2.18 (b). The measured resonant frequency of the sensor is smaller than the simulation results. This is partly due to the extra parasitic capacitance between the sensor and the readout coil. In addition there is some parasitic coupling capacitance between the primary coil and the pressure house. Although the quality factor of the proposed resonant pressure sensor is small due to the limitation of the physical dimensions and operating frequency, the measured results proved the function of the proposed wireless sensor system with an inductively coupled structure. Compared with other pressure sensors operating at the same frequency, this proposed pressure sensor shows the high sensitivity at around 400 MHz and the overall performance of the sensor system can be further improved by using a better fabricated readout coil with high inductance as well as high quality factor to improve the inductive sensitivity.



(a)



(b)

Figure 2.18 (a) Measured phase of impedance of the primary coil at the resonant frequency of pressure sensor with different pressure (b) Resonant frequencies of pressure sensor with different pressure

All the simulations and experimental results demonstrate that the proposed wireless sensor system with inductively coupled structure can effectively measure the performance of sensor under different pressure. Through theoretical analysis of the working mechanism of the wireless sensor system, the hand-made coil can provide an easy and quick method to measure the performance of pressure sensor. However, the coupling coefficient of the two inductive coils exacts a limitation on the sensitivity of the wireless sensor system, which makes it only work within a small distance that is usually smaller than  $\lambda/2\pi$ .

## 2.6 Conclusions

This chapter mainly presents the model and optimization of pressure sensor system within a limited footprint operating around 402MHz (MICS band). A wireless sensor system with inductively coupled coils is introduced for quick measurement of the resonant sensor. In addition, properly assigning the inductance and capacitance of sensor is important to achieve a resonant frequency in WICS band with the best performance. In order to maximize the performance of system under the design requirements, RF characteristics that affect inductive sensitivity and pressure sensitivity are theoretically analyzed first, and then the Design of Experiments (DOE) method is applied to model and to optimize the EM models of the sensor and the sensor system on the derived RF characteristics. The large number of combined groups of values in factorial simulations is thus reduced to a few performance related design factors. By monitoring the induced peak impedance of the readout coil, the pressure-dependent resonant frequency of the sensor can be detected and measured. The experimental results show that the optimized wireless sensor system has a relatively high average pressure sensitivity of 5.3

KHz/mmHg at a telemetry distance of 10 mm. With a hand-made coil as the primary coil, this presented wireless sensor system provides an efficient method to measure the performance of resonant sensor. With the inductively coupled structure, the implanted part of wireless sensor system is only a small bio-pressure sensor which can satisfy compact requirements in biomedical application. However, the operating range of the inductively coupled wireless sensor system is limited to a small distance and has poor noise-resistance performance.

Generally the dimension of the wireless sensor system is a critical factor for its application in the micro-medical system. There are two major approaches that can be used to down-size a wireless sensor system. One is utilizing the inductively coupled structure which has been presented in this chapter. The limited telemetry distance and weak interference-resistance limit the wide application of this simplified wireless sensor system. The other approach is to minimize the RF components of the improved wireless sensor system. Utilizing some miniaturized RF components such as antennas, filters, etc. to assist the data transmission between the sensor and the read-out circuit, the improved wireless sensor system with data processing circuits (e.g. half-active RFID systems) can work with stronger interference-resistance and longer distance. In addition, modern wireless communication systems have more and more requirements on the miniaturization of the RF components for the portable devices. And tunable RF components can be a promising solution to substitute the multi-circuits working in multi-bands, which in turn can further reduce the size of system with reduced components. The following chapters will mainly focus on the technologies for developing miniaturized and tunable RF components.

## CHAPTER 3

### MAGNETO-DIELECTRIC SUBSTRATE WITH PATTERNED PY THIN FILM FOR THE MINIATURIZATION OF RF COMPONENTS

#### 3.1 Introduction

Miniaturization is not only desired for wireless sensor systems in medical applications, but also for wireless communication systems. Modern wireless communication systems impose stringent requirements on RF blocks, especially passive RF components which typically outnumber the active parts more than 10 to 1 [50]. Recent advances in semiconductor and IC technologies have enabled the miniaturization of most transmit and receive modules in front-end ICs, but many RF components are still difficult to be integrated with other components. Electrical properties of dielectric materials are one of the main factors in the miniaturization of RF electronics. Most miniaturized passive RF components such as antennas, filters, diplexers, dividers, etc., are made with high dielectric, low-loss materials, but the strong capacitive coupling effect between ground and metal surface decreases their performance.

Magneto-dielectric material, with both effective permeability and permittivity value more than unity ( $|\epsilon_{\text{eff}}| > 1$ ,  $|\mu_{\text{eff}}| > 1$ ), have attracted great attention among researchers due to their electromagnetic properties in miniaturizing planar patch antenna without deteriorating its performance by a great amount [51]. Despite its promising performance, there is no low-loss magneto-dielectric material in nature that can be readily

for used. Many researches have been investigated and proposed to develop artificial magneto-dielectric substrates such as inserting metallic resonant particles [11], developing electromagnetic band-gap (EBG) structures [12] or metamaterials with embedded resonant circuits [13]. Unfortunately these developed substrate structures are either difficult to implement or become bulky.

This chapter, introduces a new approach of developing magneto-dielectric substrate with patterned Py thin film. The patterning method plays an important role in decreasing the magnetic loss and improving the ferromagnetic resonant frequency (FMR) of Py films. The improved FMR is a critical factor for the possible application of magnetic material in the gigahertz range. The RF characteristics of magneto-dielectric substrates are introduced, and the following section presents a brief overview of the popular approaches in developing artificial magneto-dielectric materials or substrates. After analyzing the magnetic properties of ferromagnetic materials, the nano-patterning method is proposed to reduce magnetic loss and improve the FMR of the Py thin film. A novel nano-patterned Py thin film enabled magneto-dielectric substrate is thus developed to design miniaturized RF components. The miniaturized property of the proposed magneto-dielectric substrate is demonstrated by the implementation of patch antenna.

### 3.2 Merits of Magneto-dielectric Material

The studies in [52] have presented that magneto-dielectric material with a low-loss property is a promising candidate for down-sizing components. The merits of the RF properties of the magneto-dielectric material are studied here.



### 3.2.1 Miniaturization with Magneto-dielectric Material

One of the most interesting motivations in developing magneto-dielectric material is designing a miniaturized patch antenna without deteriorating its performance. Although the miniaturization of the patch antenna can be achieved with high permittivity substrate, the strong capacitive coupling effects between the antenna and ground plane will concentrate most energy in the high permittivity region which results in the low radiation efficiency and narrow bandwidth. Another problem of the high-permittivity substrate stems from the great difference of characteristic impedance between the substrate and free space which makes impedance matching difficult. It has been theoretically and experimentally proven that a magneto-dielectric substrate with high permittivity and permeability could reduce the antenna size with increased bandwidth and improved radiation efficiency [53]. According to theory behind patch antenna, the dimensions of patch antenna is inherent to its wavelength in the medium of the substrate and expressed as

$$L_a = 0.49 \times c/f \sqrt{\mu_0 \mu_r \varepsilon_0 \varepsilon_r} \quad (3.1)$$

where  $c$  is the velocity in free space,  $\mu_0$  and  $\varepsilon_0$  represents the permeability and permittivity respectively in free space, while  $\mu_r$  and  $\varepsilon_r$  refer to the relative permeability and permittivity in substrate, and  $f$  is the operating frequency of the antenna. It shows that the size of the patch antenna can be effectively reduced by the miniaturization factor  $n = \sqrt{\varepsilon_r \mu_r}$  with both high permeability and permittivity value from magneto-dielectric substrate.

### 3.2.2 Wide Impedance Matching with Magneto-dielectric Material

The impedance matching is a crucial parameter in miniaturized RF components. The great difference of the characteristic impedance between the substrate and free space will result in impedance mismatch which will result in losses due to high reflection from the incident wave between substrate and free space. With permeability  $\mu$  more than unity, electromagnetic wave traveling between magneto-dielectric material and free space has a smaller impedance mismatch than the one traveling between a high dielectric material and free space. Any medium that can support the propagation of electromagnetic wave have the characteristic impedance related with the transmission. And the characteristic impedance of the medium can be defined as the ratio of the electric field to the magnetic field. Assume the medium is lossless, and then the characteristic impedance of the medium can be simplified to the relation between the permeability and the permittivity of the medium.

$$\eta = \sqrt{\frac{\mu_0}{\epsilon_0}} \cdot \sqrt{\frac{\mu_r}{\epsilon_r}} = \eta_0 \cdot \sqrt{\frac{\mu_r}{\epsilon_r}} \quad (3.2)$$

where  $\eta_0$  represents the characteristic impedance in free space. The impedance mismatch between two mediums can be described by the reflection and transmission of an incident electromagnetic wave on a boundary of two mediums with different permeability and permittivity as shown in Figure3.1. The incident electromagnetic wave from medium 1 is divided into two parts on the boundary, one part is transmitted successfully into medium 2, while the other part is reflected back to medium 1 with an opposite propagation direction. If the medium is lossless, the transmission and reflection coefficients between two mediums can be expressed by the characteristic impedance of two mediums as:

$$\Gamma = \frac{\eta_0 - \eta_1}{\eta_0 + \eta_1} \quad (3.3)$$

$$T = \frac{2\eta_0}{\eta_0 + \eta_1} \quad (3.4)$$

where  $\eta_0$  is the characteristic impedance in free space represented by medium 1,  $\eta_1$  is the characteristic impedance in medium 2. According to equations (3.3) and (3.4), the best impedance matching can be achieved when the reflection coefficient goes to zero with  $\eta_0 = \eta_1$ . As the description in equation status (3.2), the characteristic impedance  $\eta_1$  of medium 2 can become close to  $\eta_0$  in free space when the relative permeability of the substrate become close to the permittivity ( $\mu_r \rightarrow \epsilon_r$ ). Usually the normal dielectric substrates have relative permeability  $\mu_r = 1$ , while the permeability  $\mu_r$  of magneto-dielectric substrate is more than one. Therefore, the RF components designed with

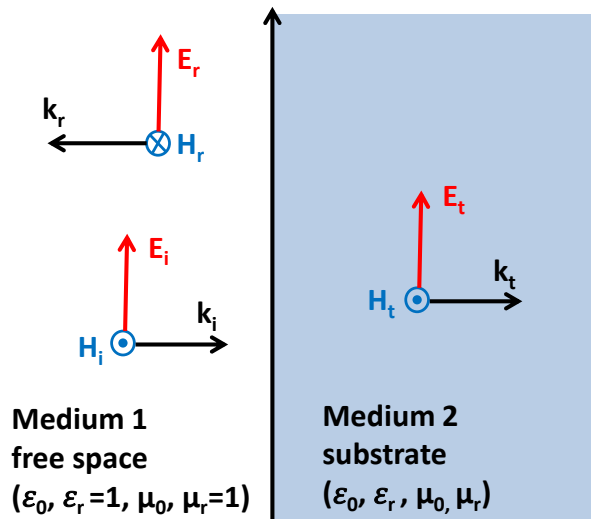


Figure3.1 Reflection and transmission of an incident electromagnetic wave on a boundary of two mediums with different permeability and permittivity

magneto-dielectric substrate have a better impedance match than normal dielectric substrate.

### 3.2.3 Wide Bandwidth with Magneto-dielectric Material

The bandwidth of the patch antenna is affected by both the electric and magnetic properties of the substrate, but better bandwidth can be obtained with the magneto-dielectric substrate. According to the transmission line model of patch antenna from Hansen and Burke [54], the zero-order bandwidth of the patch antenna (defined as  $VSWR \leq 2$ ) can be expressed as

$$BW = \frac{96 \sqrt{\frac{\mu_r t}{\epsilon_r \lambda_0}}}{\sqrt{2}[4+17\sqrt{\mu_r \epsilon_r}]} \quad (3.5)$$

where  $t$  is the thickness of the substrate,  $\lambda_0$  is the wavelength in free space. Further simplified the equation related to the permeability as [52]

$$BW \cong \frac{4\sqrt{\mu_r} \frac{t}{\lambda_0}}{\sqrt{2}\sqrt{\epsilon_r}} \quad (3.6)$$

According to equation (3.6), the bandwidth increases with an increase in relative permeability of substrate. Since the permeability of the magneto-dielectric substrate is greater than the normal dielectric substrate, the bandwidth of the patch antenna thus can be improved with the magneto-dielectric substrate.

### 3.3 Characterization of Magnetic Material

Although the previously introduced artificial magnetic material with submerged resonant structures can generate equivalent magnetic properties from their specially designed structure, it is the submerged structures that make the magneto-dielectric substrates become bulky and difficult to implement with other electronics. Magnetic material with natural magnetic properties is more attractive to be used in magneto-

dielectric substrates. However, there is a general challenge to obtain low-loss magnetic material with high permeability that is suitable for a magneto-dielectric substrate working in the gigahertz range. The interaction of electromagnetic wave with magnetic material is affected by its intrinsic magnetic properties; therefore it is necessary to study the magnetic properties of magnetic material.

### 3.3.1 Magnetization of Magnetic Material

The magnetic nature of magnetic material is affected by many factors, such as the magnetic moments of ions, atoms and electrons in the materials. The magnetic moments in materials also respond differently and the behavior varies with the environment. There are three sources for the magnetic moments: electron spin, electron orbital momentum from the nucleus and the changes in from orbital momentum induced by an applied external magnetic field ( $H_{ex}$ ) [53]. The magnetization  $M$  of magnetic materials is described as the magnetic moment per unit volume of material. How easily the material gets magnetization is quantified by its magnetic susceptibility  $\chi_m$  as the expression in [54]:



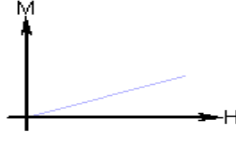

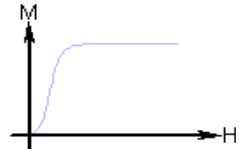

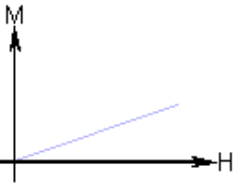
$$\chi_m = M/H_{ex} \quad (3.7)$$


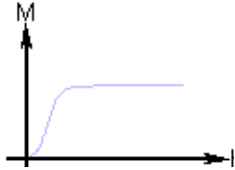
where  $M$  refers to the material's magnetization (A/m),  $H_{ex}$  represents the applied magnetic field. The permeability, a quantitative evaluation of how the material gets its magnetization, is defined as the ratio of total magnetic flux to the magnetic field generated in the material [55] :

$$\mu = \frac{B}{H} = \frac{\mu_0(H_{ex}+M)}{H_{ex}} = \mu_0(1 + \chi_m) \quad (3.8)$$

An applied external magnetic field always tries to align the magnetic moment of atoms along with the field direction. According to the response to the external magnetic field, magnetic materials can be classified into five main groups: diamagnetic, paramagnetic, ferromagnetic, anti-ferromagnetic and ferrimagnetic materials. The magnetic properties of these materials [53, 54, 55] can be classified with their magnetic properties including magnetic susceptibility, atomic magnetic behavior and tendency of susceptibility as shown in Table 3.1.

Table 3.1 Classification of magnetic materials based on magnetic properties

Type of magnetic material	Magnetic susceptibility	Atomic Magnetic behavior	Susceptibility
Diamagnetic	Negative and small	No magnetic moment	
Paramagnetic	Positive and small	Randomly oriented magnetic moments 	
Ferromagnetic	Positive and large, function of applied magnetic field, microstructure dependent	Parallel aligned magnetic moments 	
Anti-ferromagnetic	Positive and small	Mixed parallel and anti-parallel aligned magnetic moments 	

Ferrimagnetic	Positive and large, function of applied magnetic field, microstructure dependent	Anti-parallel aligned magnetic moments 	
---------------	--	---	---

As shown in Table.3.1, ferromagnetic material has highly parallel aligned magnetic moments ( $\mu$ ) which result in large net magnetization along a particular direction and can keep the net magnetization even in absence of an external magnetic field, while paramagnetic and diamagnetic materials exhibits very small or no magnetic moments under the applied magnetic field. Compared to other magnetic materials, ferromagnetic material has a high and relatively stable permeability which is greatly desired for the design of magneto-dielectric substrate. However, ferromagnetic material has some fundamental limitations in achieving the desired magnetic properties which are suitable for the design of a magneto-dialectic substrate applied in RF application. The fundamental limitations on the magnetic properties of the ferromagnetic materials will be discussed in the following section.

### 3.3.2 FMR of Magnetic Material

Ferromagnetic resonance (FMR) is one of the most importance magnetic properties used to evaluate the performance of the magnetic material. Assuming that the ferromagnetic material is put in magnetic fields alternating at high frequencies, heat effects due to resonance of the magnetic material can be observed at a certain frequency which is defined as the FMR of the material. At FMR, the electron spins of materials oscillating heavily which cause the generation of heat [55]. That is to say that the FMR can be used to evaluate the energy loss of magnetic material. For the ferromagnetic

material with loss, the equation describing the magnetic moment contains a damped ratio  $\alpha$ . According to Landau Lifshitz Gilert (LLG) equation [56], the magnetic moment related to the direction of the applied external magnetic field is expressed as

$$\frac{d\vec{M}}{dt} = -\mu_0\gamma\vec{M} \times \vec{H}_{ex} + \frac{\alpha}{M}(\vec{M} \times \frac{d\vec{M}}{dt}) \quad (3.9)$$

where  $\vec{M}$  refers to the sum of magnetic moments over a volume,  $\gamma$  is the gyromagnetic ratio,  $\vec{H}_{ex}$  is the applied external magnetic field.

Due to the loss from magnetic friction, the energy supplied by the applied external magnetic  $\vec{H}_{ex}$  field is translated into heat in the ferromagnetic material. The polarization of external magnetic field and magnetic moment  $\vec{M}$  is shown in the Figure3.2, where  $H_0$  represents the horizontal part of the magnetic field. When the applied magnetic field  $\vec{H}_{ex}$  rotates opposite to the direction of the magnetic moments  $\vec{M}$ , the magnetic material exhibits low loss. Therefore, electromagnetic wave propagated in ferromagnetic material has a ferromagnetic resonance with a peak loss for a clockwise polarization of external magnetic field  $\vec{H}_{ex}$  which coincides with that of magnetic moments  $\vec{M}$  and a flat low loss for opposite polarization. High ferromagnetic resonance above working frequency is the

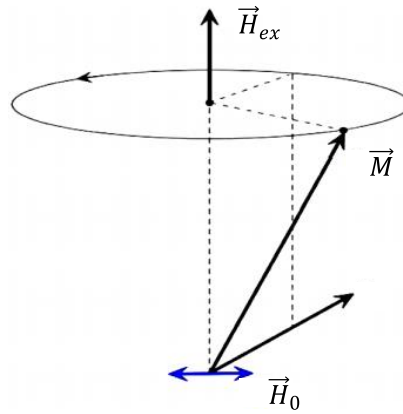


Figure 3.2 Precession of spinning electron in a steady magnetic field [57]



most basic requirement for the application of ferromagnetic material in RF components, and the improvement of FMR with improved effective magnetic field anisotropy can be used.

### 3.3.3 Magnetic Anisotropy of Ferromagnetic Material

Magnetic anisotropy evaluates how much the magnetic property of magnetic material to have directional dependence and associated with the alignment of the magnetic moment in a preferred direction. There is a preferred direction in magnetized material called easy axis representing the direction of spontaneous magnetization [53]. In magnetically isotropic material, it is defined that no magnetic moment is oriented in a preferred direction.

Magnetic anisotropy is highly desired for the small hysteresis in ferromagnetic material. The magnetized process is full of the concentration of the domain wall motion and domain rotation. Magnetic domains are defined as a region having parallel spins that

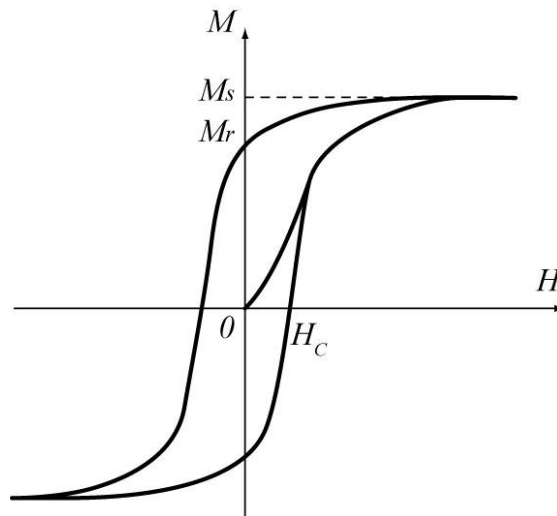


Figure 3.3 Hysteresis of the magnetization  $M$  versus an applied magnetic field [58]

can result in spontaneous magnetization [55]. The full cycle of magnetization and demagnetization is called a hysteresis loop, and a sample of a hysteresis loop in magnetic material is shown in Figure 3.3.  $M_s$  refers to the saturation magnetization,  $M_r$  represents remnant magnetic field and  $H_c$  represents coercivity. All of referred parameters are dependent on the magnetic anisotropy of material and the approaches of synthetization. Generally a narrow area of hysteresis is required for the application of magnetic material in RF components. Among all the magnetic materials, ferromagnetic material has the relative small hysteresis area [55].

The magnetic anisotropy is mainly determined by three sources: magneto-crystalline, shape and stress. Magneto crystalline anisotropy is an intrinsic property of the material. That is to say that the magneto crystalline anisotropy cannot be changed by the shape and size of material. Stress anisotropy, associating with the spin-orbital coupling generated by the change of spin orbits, needs to be avoided when the magnetic material is used many times [59]. The shape anisotropy is an important anisotropy for the magnetic material due to its artificially controllable property by the shape of material. Having an

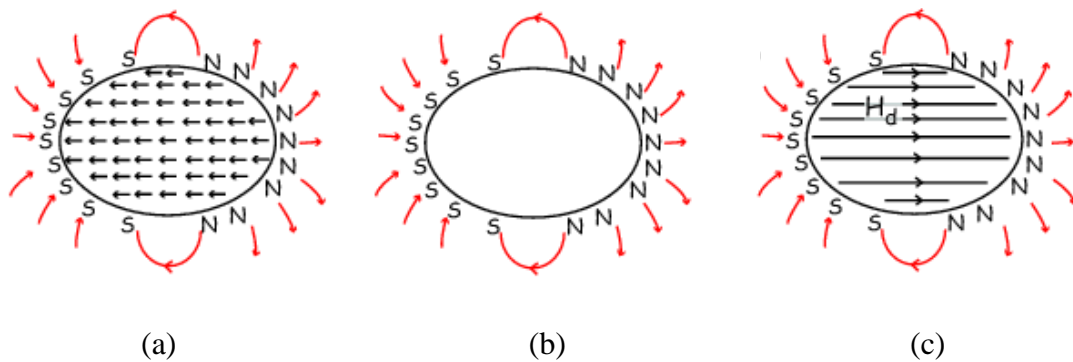


Figure3.4 (a) Internal magnetizations within ferromagnetic material (b) Identical external field from surface monopoles (c) The internal “demagnetizing” field from induced surface monopoles [60]

inherent net magnetic moment along certain preferred direction even in absence of an external magnetic field, there will be magnetic charges or poles induced at the surface of the ferromagnetic material. The generated magnetic charges or poles can be identified as the north and south poles as shown in Figure 3.4.

The surface charges generated from external magnetic fields produce magnetic field with the direction represented by the surface monopole orienting from the north poles to south poles. The external magnetic fields also induce internal demagnetizing fields due to the continuation of field. With an action in an opposite direction to the magnetization that external field produces, the internal field is called the demagnetizing field. The total net magnetic anisotropy of ferromagnetic material can be expressed as magnetized field minus the internal demagnetizing field ( $H_{ani}=H_{mag} - H_{demag}$ ), where  $H_{mag}$  is the inherent magnetic anisotropy and  $H_{demag}$  is the demagnetizing field generated by the magnetized body. High demagnetizing field contributes to reducing the total net magnetic anisotropy. In order to increase the total net magnetic anisotropy field, decreasing the demagnetizing field is one of the effective methods. As shown in Figure 3.4(c), increasing the distance between the north poles and south poles along the easy axis of material body can be an easy way to decrease the demagnetizing field when the internal field from north poles to south poles become far away from each other. Developing the shape of material body with high aspect ratio of the length to width along the easy axis of magnetization can serve this function. In the following section, a patterning method applied on the Py thin film is introduced and discussed to increase the magnetic anisotropy and FMR.

### 3.4 Magneto-dielectric Substrate with Patterned Py thin Film

As presented in the previous section that FMR and magnetic anisotropy are two important magnetic properties that affect the performance of ferromagnetic materials in device realization. The following sections introduce the approach of using Nano-patterned film to improve the magnetic properties and propose a novel magneto-dielectric substrate made with nano-patterned ferromagnetic thin film.

#### 3.4.1 Nanocomposite Ferromagnetic Film

Ferromagnetic material consisting of nanoscale particles can provide a special way to address the limitations on magnetic properties. The magnetic properties of a magnetic body made of small grains depend on the counter play of the local magnetic anisotropy energy and ferromagnetic exchange energy [60]. For large grains, the magnetization is determined by different magnetic directions along the easy axis of single grains, so multiple domains are formed in the large grains. The magnetization process is determined by the magneto-crystalline anisotropy [61]. With the reduced magnetic particle size in the nanoscale region, the single domain in small grains can stabilize to cover the grain size and exchange length. In addition, magnetic exchange interactions among the magnetic particles forces the formation of magnetic moments aligned in parallel, thus the magnetization of magnetic material follows the easy axis of each small grain. Therefore, the effective anisotropy of magnetic body is the average magnetic behavior over several small grains and obtains a reduced magnitude. For example, Ni-Fe- based nanocomposite material have higher permeability at microwave frequencies than those made of bulk Ni- Fe- composites [62]. With Nano sized magnetic particles, the induced eddy currents within the particles are also small and can be negligible, and thus

lead to smaller loss in nanocomposites when compared with that of bulk sized ferromagnetic materials.

### 3.4.2 Patterning approach on Ferromagnetic Thin Film

According to the description in the previous section about shape anisotropy, the strategy applied in the engineered substrate is to increase the shape anisotropy field of Py thin film by a big margin from rectangular slim bars while keeping the magnetic loss introduced by Py at a tolerable range. Studies in [63] have shown that patterning ferromagnetic thin films into narrow strips could effectively improve its FMR with the induced shape anisotropy field. To better understand the pattern geometry effects of magnetic properties such as FMR, permeability value, theoretical principles are used and compared. The external magnetic field applied along the easy axis of magnetization can increase the FMR frequency by increasing the anisotropy field as described in Kittel's law [64],

$$f_r \approx \frac{\gamma}{2\pi\sqrt{1+\alpha^2}} \sqrt{H_k(4\pi\epsilon M_s - H_k)} \quad (3.10)$$

where  $\gamma(= 1.76 \times 10^{11} \text{ T}^{-1} \text{ s}^{-1})$  represents the gyromagnetic ratio,  $M_s$  is saturation magnetization,  $\alpha$  is the damp constant,  $H_k$  represents effective uniaxial anisotropy field of un-patterned film, and  $\epsilon$  is the overall effective demagnetization factor. The in-plane demagnetization factor is taken into account for the created shape anisotropy field due to the selective patterning. According to equation (3.24), the FMR  $f_r$  shifts correspondingly toward higher value with the increment of length-to-width ratio. With the calculated FMR  $f_r$ , the frequency dependent permeability of the patterned thin film can be easily derived from Lorentzian Law according to Lifshitz-Gilbert's equation [65]

$$\mu(f) = 1 + \frac{\mu_s - 1}{1 + if/f_a - f^2/f_r^2} \quad (3.11)$$

where  $\mu_s = 1 + 4\pi M_s/H_k$ ,  $f_a = \gamma H_k/2\pi\alpha$ , and for a very thin ferromagnetic thin film with  $4\pi M_s \gg H_k$ . The induced shape anisotropy field can increase the damping constant  $\alpha$ , thus in turn broadens the permeability spectrum [66]. For the permeability in the film plane along its hard axis, the real and imaginary parts of permeability can be written related to the FMR  $f_r$  respectively.

$$\mu(f)' = 1 + \frac{4\gamma^2 M_s^2 (f_r^2 - f^2)}{(f_r^2 - f^2)^2 + (2\alpha f_r f)^2} \quad (3.12)$$

$$\mu(f)'' = \frac{8\gamma^2 M_s^2 (\alpha f_r f)}{(f_r^2 - f^2)^2 + (2\alpha f_r f)^2} \quad (3.13)$$

Equations (3.26) and (3.27) indicate that the real and imaginary parts of the permeability along hard axis are decreased with the increment of FMR  $f_r$ . It means that larger permeability value comes with bigger loss of the ferromagnetic material. Thus there is a compromise between high FMR  $f_r$  and large permeability value when choosing optimized pattern sizes. The choice of Py patterns will play an important role in decreasing the magnetic loss and increasing FMR.

### 3.4.3 Construction of Magneto-dielectric Substrate with Patterned Py thin Film

According to the presented approaches, the magnetic properties of the Py film can be improved with nanocomposite patterns. Besides the magnetic materials, the selection of the dielectric substrate is also important not only for dielectric performance, but also for easy integration with other components. In this respect, a high resistivity silicon substrate is highly considered as one of the most attractive choices. Because it can support heterogeneous integration of magneto-dielectric substrate based components with other technologies based devices such as MEMS, semiconductor components, etc. A 3D

view of the construction of the proposed magneto-dielectric substrate enabled with patterned Py thin film is shown in Figure3.5. The Nano-patterned Py thin film with a thickness of 100nm is deposited on the silicon substrate using DC magnetron sputtering process performance in air atmosphere with controlled N<sub>2</sub> admixture. The Py thin film is patterned into an array of 15um by 20um strips with a 10um gap among them. To implement with the proposed magneto-dielectric substrate, RF components can be fabricated on arbitrary substrates with printed circuit board (PCB) technology and then bonded to the top of magneto-dielectric substrate. The separated fabrication of the magneto-dielectric substrate and RF components provides a flexible and cost-effective method to develop miniaturized components with magneto-dielectric substrate.

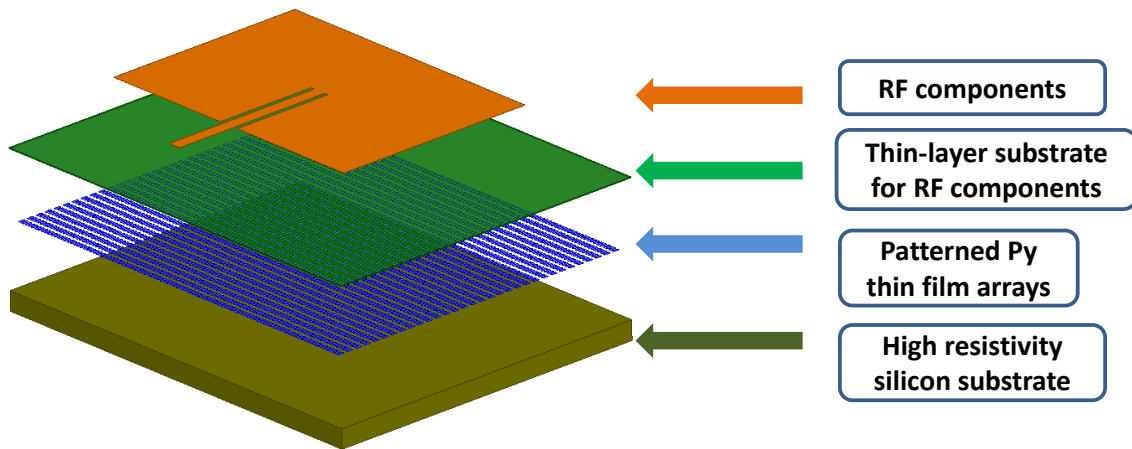


Figure3.5 Trimetric view of the construction of the patterned Py thin film on high resistivity silicon substrate

### 3.5 Implementation of Magneto-dielectric Substrate

The effects of miniaturization on RF components with this proposed magneto-dielectric substrate is demonstrated by the implementation of a patch antenna.

#### 3.5.1 Simulation of Patch Antenna

The LCP (permittivity  $\epsilon_r$  of 3.16) with a thickness of 100um is selected as the supporting substrate of patch antenna. The top view and side view of the EM model of the implemented magnetic antenna are shown in Figure 3.6 (a) and (b). Generally the length and width of patch antenna on a homogeneous substrate can be calculated directly from the theory behind the patch antenna. With the implementation on a multi-layered heterogeneous substrate, the equations for designing patch antenna with calculated width and length are no longer suitable. The design of patch antenna on multi-layered substrate with magnetic properties or without magnetic properties can be realized through the optimization on EM models in HFSS. The last optimized dimension of no-magnetic antenna working around 2.5GHz is shown in Figure 3.6 (a).

According to [67], magnetic property of Py thin film with an estimated permeability of 1900 can be used in the EM models of the magnetic antenna. The effects of the magnetic properties of nano-patterned Py thin film on the magnetic antenna are exhibited from the overall multi-layered substrate. The simulated return losses (S11) of patch antenna on multi-layered substrate with magnetic properties and without magnetic properties are respectively shown in Figure 3.7 (a). It shows that the resonant frequency of the patch antenna on a multi-layered substrate without magnetic properties is 2.5GHz as a result of optimization on the EM model. However, the resonant frequency of patch antenna can shift to a lower frequency of 2.43GHz on multi-layered substrate with



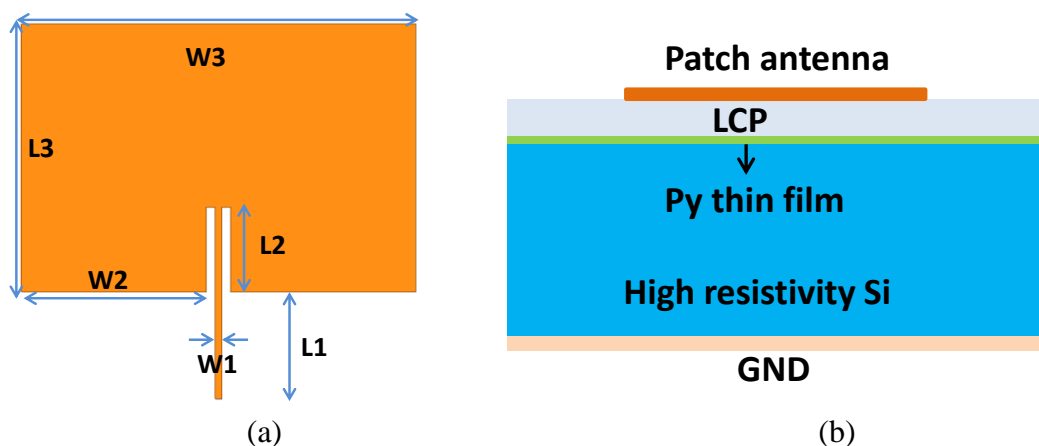
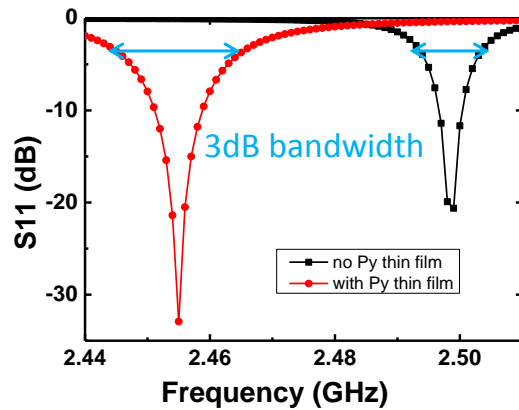
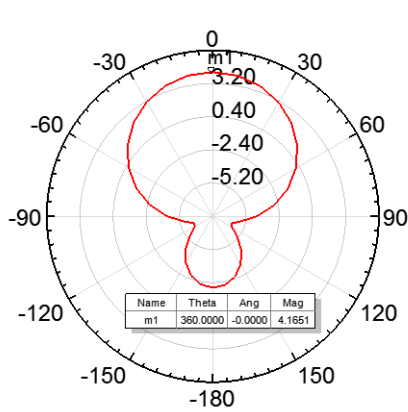


Figure 3.6 (a) Top view of the no-magnetic patch antenna with optimized dimensions:  $L1=8\text{mm}$ ,  $L2=6.34\text{mm}$ ,  $L3=21.4\text{mm}$ ,  $W1=0.45\text{mm}$ ,  $W2=13.175\text{mm}$ ,  $W3=28\text{mm}$  (b) side view of the patch antenna on magneto-dielectric substrate

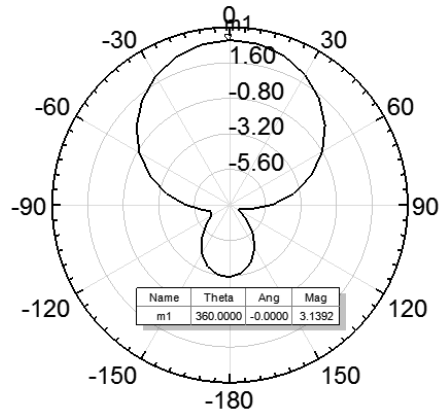
magnetic properties. The same dimension of patch antenna working on magnetic substrate has a smaller resonant frequency than that of the non-magnetic antenna. This is due to the miniaturization factor increasing from  $\sqrt{\epsilon_r}$  of the non-magnetic substrate to  $\sqrt{\mu_r \epsilon_r}$  of the magnetic substrate as described in the previous section for the merits of magnetic-dielectric materials. Compared to the 3dB bandwidth of non-magnetic antenna with a bandwidth of 8 MHz, the bandwidth of magnetic antenna is increased to 16 MHz which shows an increase of 50% bandwidth over the no-magnetic one. The simulated gain of the magnetic antenna on elevation plane is also better than that of the no-magnetic antenna as the results shown in Figure 3.7 (b) and (c). A list of the performance of the no-magnetic antenna and magnetic antenna is shown in Table 3.2. The simulated performance shows that the magneto-dielectric substrate made with patterned Py thin film can be used to design a miniaturized antenna without detreating its performance.



(a)



(b)



(c)

Figure 3.7 (a) Simulated return loss of patch antenna on multi-layered substrate with magnetic properties in an ideal case and without magnetic properties. (b) Radiation pattern of magnetic antenna in elevation (YZ) plane. (c) Radiation pattern of non-magnetic antenna in elevation (YZ) plane

Table 3.2 Listed performance comparison between magnetic antenna and non-magnetic antenna

$\mu_r$	Central Frequency	BW	Gain	Efficiency
1	2.5GHz	8MHz	3.14dB	42.34%
1900	2.43GHz	18MHz	4.16dB	57.82%

### 3.5.2 Measurement of Patch Antenna

The fabrication of the magneto-dielectric substrate and patch antenna are independent from each other with different methods. As described in the previous section, the patterned Py thin film is deposited on high-resistivity silicon using DC magnetron sputtering method while the patch antenna is fabricated on LCP substrate with PCB technology. The magnetic antenna is implemented through bonding the LCP substrate to the top surface of the magneto-dielectric substrate as shown in Figure 3.8 (a). Figure 3.8 (b) shows the measurement results of patch antenna on a magneto-dielectric substrate and non-magnetic antenna on normal silicon substrate.

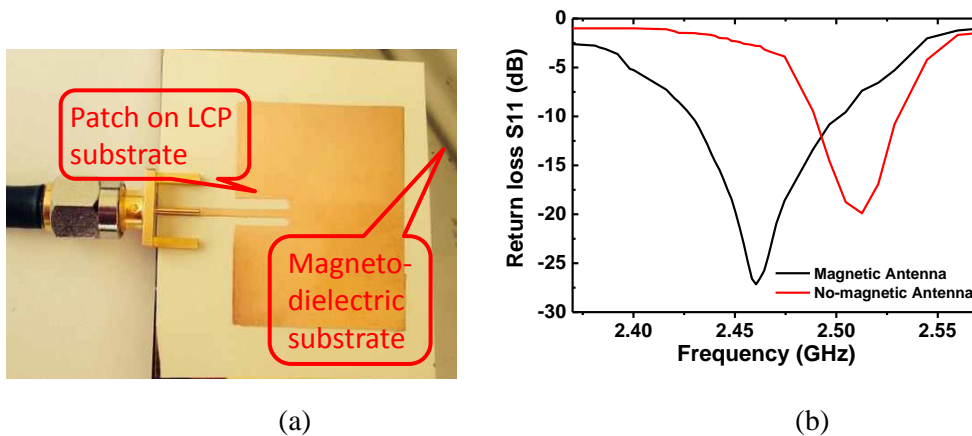


Figure 3.8 (a) Measurement of the magnetic patch antenna on magneto-dielectric substrate (b) Measured return loss of magnetic antenna and non-magnetic antenna.

As shown in Figure 3.11 (b) the resonant frequency of the non-magnetic antenna on a pure silicon substrate is 2.524GHz which is higher than the simulated resonant frequency. This is partly due to the air gap between the patterned Py thin film and LCP substrate. The measured resonant frequency of the magnetic antenna is around 2.455GHz which is also higher than the simulated results. One reason is partly due to the air gap

between the patterned Py thin and another one is related to the roughly estimated permeability of patterned Py thin film in the simulation. The applied permeability in the simulation is higher than that in the practical design. According to the measurement results of the two antennas, it demonstrates that the magneto-dielectric substrate can be applied for designing miniaturized components. It is a cost effective and easy method to re-use the magneto-dielectric substrate for designing different RF devices.

### 3.6 Conclusions

This chapter presented a novel approach in developing a magneto-dielectric substrate with Nano-patterned Py thin film on high-resistivity silicon. The substrate is fabricated with DC magnetron sputtering technology to develop patterned Py thin film, which is independent from the fabrication process of the implemented RF components. After analyzing the magnetization moments, the Nano-patterning approach is introduced to improve the two important magnetic properties of the Py thin film. Based on antenna theory and experimental results, implementation of patch antenna on magneto-dielectric substrate demonstrates that the effect of magnetic properties of patterned Py thin film on the overall multi-layer substrate can be used to design miniaturized antenna and the magneto-dielectric substrate shows a more effective miniaturization factor ( $n = \sqrt{\epsilon_r \mu_r}$ ) than that of a normal dielectric substrate ( $n = \sqrt{\epsilon_r}$ ).

## CHAPTER 4

# ENGINEERED SUBSTRATE WITH PATTERNED PY THIN FILM FOR ELECTRICALLY TUNABLE RF COMPONENTS

### 4.1 Introduction

Besides the miniaturization for mobile convenience, modern wireless communication system also exerts requirements on multi-frequency bands to support multiple communication standards. The need for a multi-band operation, a diversity phase shifter, and adaptive impedance matching prompted the development of tunable RF components. And the tunable RF components can further reduce the size of the system with a reduced number of components when several circuits can be substituted by one. In addition, tunable RF components are a promising solution to adapt to the varied antenna impedance for a wireless sensor system under different environments. To satisfy the requirements of multi-bands and multi-stands, a variety of reconfigurable or tuning technologies have been investigated and applied in RF components. These include the direct change to the schematic model of unit circuits by varying capacitance or inductance, using electrically, magnetically, or chemically sensitive materials to change the electromagnetic properties of tunable material based structures and therefore change their electrical length or alter the geometry of the unit cell through stretching, shifting, or deforming the structure [68]. The main difficulties in designing tunable components are

how to make the tunable approach cost effective, compatible with other technologies and easily fabricated.

Chapter 3 has demonstrated the effects of magnetic properties of a patterned Py thin film on the overall multi-layer substrate for designing a miniaturized antenna. Besides the magnetic properties suitable for miniaturized components, the permeability of Py can be adjusted both by an external magnetic field and a DC current. The difficulty is that magnetically tunable components cannot meet the miniaturization requirement when a large and cumbersome external biased magnetic field is used, and thus electrically tunable components are developed. With a new structure developed from previously magneto-dielectric substrate, a novel engineered substrate enabled with patterned Py thin film is proposed to design arbitrary electrically tunable RF components in this chapter. The popular technologies for reconfigurable RF components are firstly reviewed and introduced. Then the effects of magnetic properties of patterned Py thin film on the engineered substrate with reconfigurability properties is analyzed and demonstrated with the implementation of different types of tunable RF components (one-port patch antenna, two-port phase shifter, two-port band-pass filter, three-port band-pass filtering balun).

#### 4.2 Reconfigurable Technologies

The basic idea of reconfigurable RF components is developing tunable elements in a circuit model or equivalent circuit model such as capacitive switches, varactors, variable inductors and resonators. This section will review the popular technologies for developing tunable elements and specify their functionality, typical applications as well as advantages and disadvantages.

#### 4.2.1 Tunable Semiconductor Components

Semiconductor varactors, making use of the voltage-dependent depletion region of space charge area, are widely developed and applied voltage-controlled capacitances including Schottky diode varactor, p-i-n diode varactor and MOS varactor. With a high permittivity semiconductor as the dielectric material of the varactor, the value of the semiconductor varactor becomes large. In addition, the semiconductor varactor follows the standard fabrication process that can be easily integrated with other components. However, the nonlinear behavior of the diode varactor cannot function properly in a high frequency range [69], which limits their applications in the high frequency spectrum.

Because of the different electrical properties of the depletion region under forward and reverse voltage, the semiconductor diodes can act as tunable switches with two operating statuses: a resistance in ON status with forward voltage and a capacitance in OFF status with reverse voltage. As the switch model shown in Figure 4.1 (a), when reverse voltage is applied, the switch works in OFF status with a low capacitance value  $C_{off}$ , which results in a high impedance. When working in ON status, the semiconductor diode acts as a small resistance  $R_{on}$  under forward voltage as shown in Figure 4.1 (b). For practical application, a small resistance  $R_{on}$  is always preferred to achieve better performance. However, small resistance  $R_{on}$  can increase  $C_{off}$  which reduces the tunable ratio expressed by  $C_{on}/C_{off}$  [70]. With two operating statuses, the semiconductor diode can be only tuned digitally, which is not suitable for analog tunable requirements.

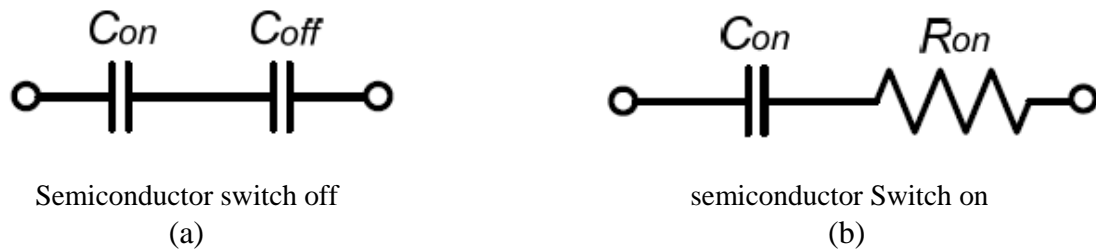


Figure 4.1 Equivalent circuits for semiconductor switch in (a) OFF state and (b) ON state.

#### 4.2.2 Tunable RF MEMS components

RF MEMS are defined as microsystems manufactures featured with movable mechanical micro-parts capable of reconfiguring the characteristics of RF MEMS devices. The RF MEMS components are generally composed of a thin metal beam which can be pulled down by an electrostatic force applied between the pull-down electrode and the bottom metal plate [71] as shown in Figure 4.2. Similar to semiconductor components, tunable RF MEMS elements can be classified into two types: varactors and switches. The difference between the RF MEMS switches and varactors lies in the applied tunable voltage. The RF MEMS switch is controlled by digital voltages, which only have two operating statuses – ON or OFF. The RF MEMS varactor can be adjusted by analog voltages that allow continuous tunable capacitance. Therefore, the RF MEMS varactor is expected to have better tuning performance. Nevertheless, the implementations of RF MEMS varactors may suffer from deform distortion when the position of the thin membrane gets changed with the applied voltage [72].



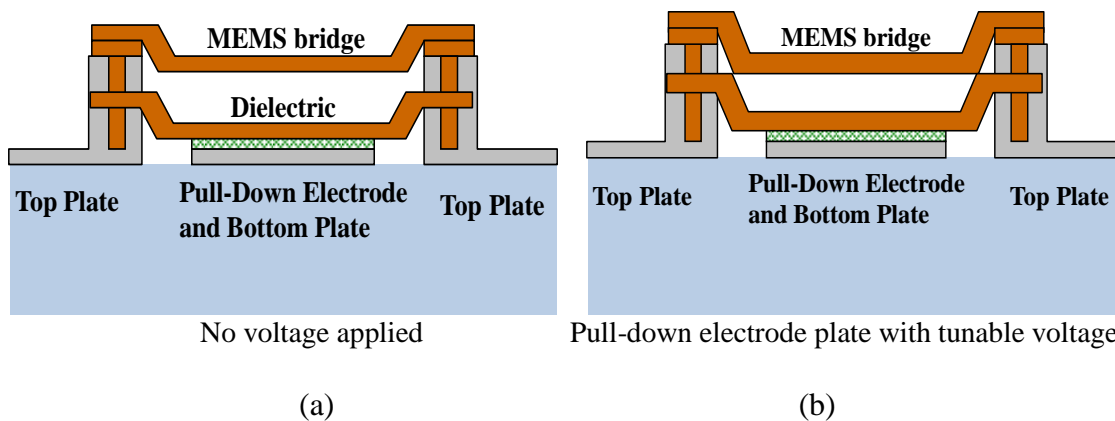


Figure 4.2 Cross-section view of the two statuses of RF MEMS components (a) No voltage applied (b) Pull-down electrode plate with voltage

Unlike the conventional PIN diode, RF MEMS components can be used to design novel tunable RF components with some desirable features including small size, linearity, low insertion loss, large power handling capability and good isolation, and have been widely developed and applied in intelligent wireless communication systems. An example of a tunable band-pass filter based on RF MEMS switch with layout and working performance is shown in Figure 4.3. This bandpass filter is tunable with the three groups of states exhibited by the switches. However, there are some disadvantages that restrict the wide application of RF MEMS in wireless communication systems. Firstly, the stringent requirements for hermetic packaging is desired for the application of RF MEMS components and the required hermetic package is not compatible with standard fabrication process, which increases the cost of the RF MEMS based devices. Secondly, the combination of a small tuning capacitance range and large controlling analogue or digital voltage restricts their RF performance. In addition, the reliability of RF MEMS components is sensitive to many factors that the complicated design and

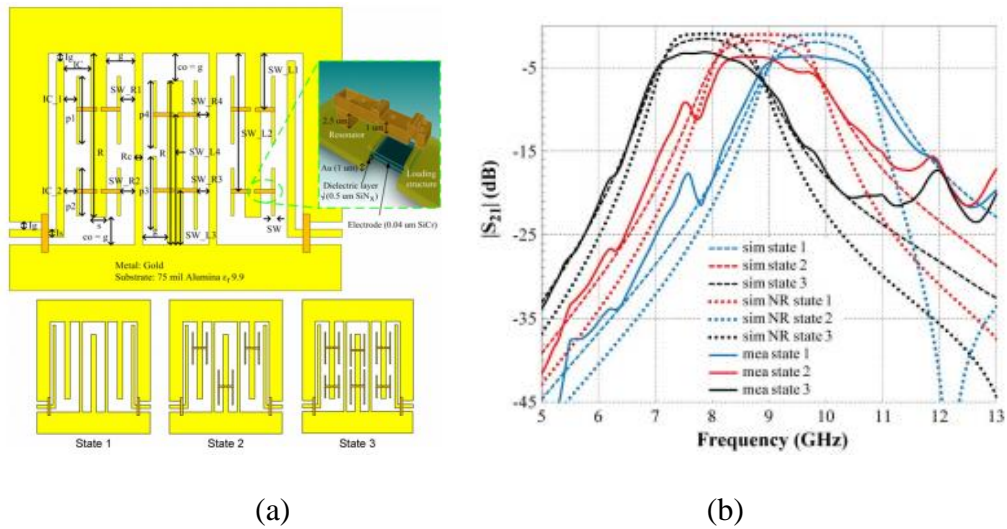


Figure 4.3 (a) Layout of tunable band-pass filter based on RF MEMS. (b) Simulation and measurement results of tunable band-pass filter [73].

fabrication process may hamper their wide application in wireless communication systems where reliability is required.

#### 4.2.3 Tunable Ferroelectric Materials

With a DC voltage-dependent permittivity, ferroelectric materials have great promise in the development of electrically tunable varactor. Ferroelectric materials are incorporated or loaded by RF components in the form of thin films. With tunable capacitance induced by the change in effective permittivity value of ferroelectric materials, RF components designed with ferroelectric materials can thus be tuned by DC voltage. By varying the thickness of the ferroelectric thin films, the operating voltages and tunable frequency range can be adjusted accordingly. Barium-Strontium-Titanate oxide (BST) and Lead Zirconium Titanate (PZT) are two of the most commonly used ferroelectric materials for tunable RF components. Generally it is important to characterize the electrical properties of ferroelectric materials before starting the design

of RF components. Studies in [74], an EM model based on computer-aided design is developed first to analyze the properties of BST thin film from 1 to 16 GHz. Then coplanar waveguides (CPWs) and inter-digital capacitor (IDC) are fabricated with BST thin film. With the characterized properties of ferroelectric films, tunable RF components can be accurately designed. An example of the layout and performance of tunable low pass filter enabled with BST thin film on silicon substrate is shown in Figure4.4. With the applied DC voltage, the permittivity of the BST thin film is varied which can change the capacitance and thus the tunable cut-off frequency.

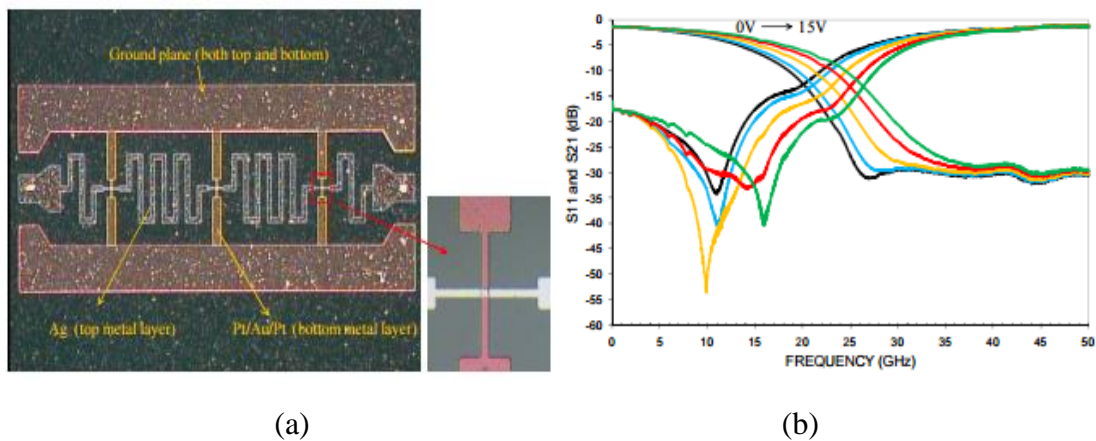


Figure4.4 (a) BST thin film based tunable low-pass filter on silicon substrate (b) Measured transmission and reflection coefficients of BST thin film based high-pass filter under different voltages [75].

Different from the movable mechanical parts of RF MEMS components, the ferroelectric material based varactor has a response time much smaller than that of a MEMS switch. Compared to the tunable components based on semiconductor or MEMS technology, the ferroelectric materials based tunable devices offer some desired features including easy integration, reproducibility and low cost on fabrication ,but low quality

factor  $Q$  [76]. Integrated with high-permittivity ferroelectric layers, the tunable devices can be designed with smaller size. The required RF characteristics of ferroelectric thin films are highly dependent on the quality of the thin films which are mainly determined by the fabrication process and type of material. The merits of tunable ferroelectric materials are limited by the compromise between better tuning frequency range and higher losses from transmission line.

#### 4.2.4 Tunable Magnetic Materials

Besides the high permeability value, the permeability of ferromagnetic materials and ferrites can be tuned both by the external magnetic-field and DC current, which make them another promising method to design tunable RF components. Similar to the effects of permittivity, the permeability has the same contribution to the propagation constant and the phase. Any changes from the biased magnetic field will change the effective permeability of ferrites or ferromagnetic materials. As described in the equation ( $c = 1/\sqrt{\mu\varepsilon}$ ), the square root of the permeability is inversely proportional to the velocity of electromagnetic wave. Therefore, a number of magnetically tunable RF components have been developed by using bulk ferrites or ferromagnetic material as key tuning elements. An example of a magnetically tunable bandpass filter based on a partially magnetized ferrite substrate is presented in [74] as shown in Figure4.5. A total frequency tuning range of 7% is achieved from 5.77GHz to 6.22GH with a varied magnetic bias changed from 0Oe to100Oe.

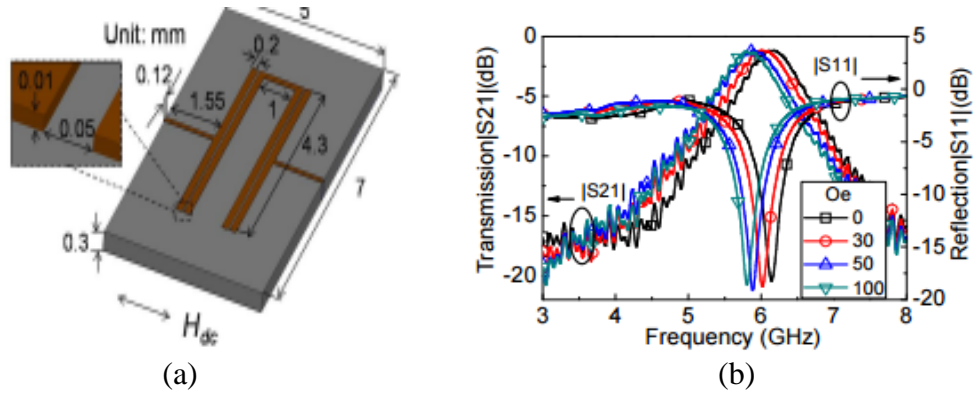


Figure 4.5 (a) 3D view of magnetically tunable bandpass filter based on partially magnetized ferrite substrate (b) Measured transmission coefficients under different magnetized field [77]

However, the introduced magnetically tunable components with ferrites have a bulk volume. In addition, with a cumbersome external biased magnetic field, magnetically tunable RF components cannot satisfy the miniaturization requirements of portable devices in modern wireless communication even when substituting the bulk ferrites with light ferromagnetic materials. Recently researchers have turned more efforts to develop electrically tunable RF components with ferromagnetic materials. Compared to ferrites, ferromagnetic materials have high saturation magnetization, relatively high ferromagnetic resonance frequency (FMR) and low processing temperatures that are suitable for RF applications [78]. As discussed in chapter 3, the main difficulty in using ferromagnetic material for tunable RF components is the small FMR limited within sub-gigahertz range. The nano-patterning method has been proposed to improve the FMR up to several gigahertz [64]. A CPW slow wave structure based electrically tunable transmission with nano-patterned Py thin film is developed in our group for the first time [79] as shown in Figure 4.6. Having a nano-patterned Py thin film along the signal line, DC current applied on the signal line can offer a tunable DC magnetic field to adjust the

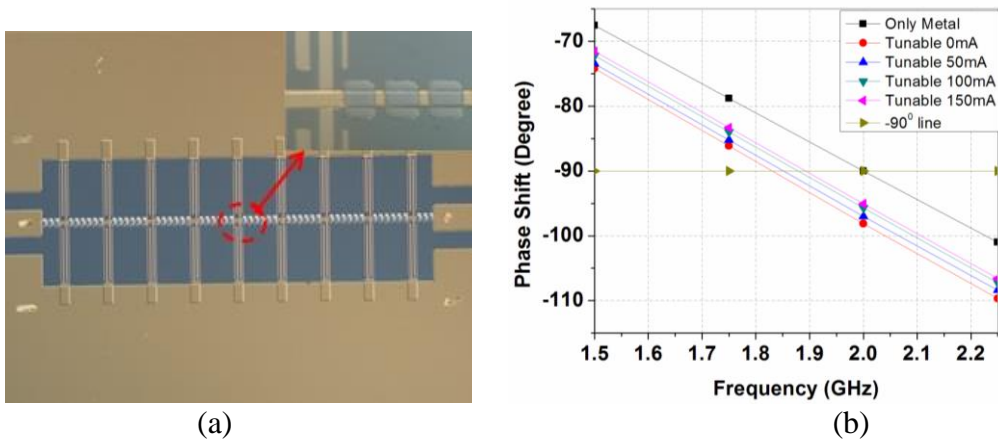


Figure 4.6 (a) Layout of CPW slow wave structure based electrically tunable transmission with nano-patterned Py thin films (b) Measured phase shift of CPW slow wave structure based electrically tunable transmission line with different DC current and regular CPW [79].

permeability of the Py film. A  $90^\circ$  phase shift of the CPW slow wave structure based transmission line can thus be turned from 1.84GHz to 2GHz when the DC current is changed from 0mA to 150mA. It proves that ferromagnetic material can be suitable to design electrically tunable components up to the gigahertz range after patterning.

#### 4.2.5 Comparison of Different Types of Tuning Technologies

According to the brief overviews of several types of reconfigurable technologies, each technology has its own advantages and disadvantages in the performance of components and tunable properties. Semiconductor technology is a cost-effective approach to design tunable RF components with a medium sized footprint and a low tuning voltage. However, the tunable semiconductor based varactors suffers from transmission losses, nonlinear tunable behavior and inter-modulation noises. Although RF MEMS based tunable components exhibit a linear performance, they are highly

sensitive to the fabrication process and package quality. In addition their response time in MEMS is slow and that limits their performance. Ferroelectric materials, loaded with RF components in the form of thin films, provide a highly tunable range and most importantly can be easily integrated with other devices. However, these devices suffer from dielectric loss, high tuning voltage and low quality factor. For tunable magnetic materials, although magnetically tunable ferrites based RF components are bulky and hard to handle, electrically tunable ferromagnetic thin film can be a promising technology. With a high and DC current-dependent permeability, ferromagnetic thin film based electrically tunable RF components can be designed with a high quality factor and compact size. The response time and power consumption of ferromagnetic material can also be improved and limited in a moderate range [77]. A comparison of performance and tunable properties among different tuning technologies is listed in Table 4.1 in terms of tunability, quality factor, response time, power consumption and size [73, 75,77,79].

Table 4.1 Comparison of different types of tuning technologies

Type of Tuning Technologies	Semiconductor	RF MEMS	Ferroelectric	Ferromagnetic
Tunability	High	Low	Moderate	Moderate
Quality factor Q	Low	High	Moderate	High
voltage or current	Low	High	Moderate to High	Moderate to High
Response time	Moderate	High	Fast	Moderate
Power consumption	Low	High	Moderate to High	Low to Moderate
Physical size	Medium	Medium to large	Small	Small

### 4.3 Electrically Tunable Py Patterns Enabled Engineered Substrate

As described in previous section, tunable RF components have been widely investigated and developed with semiconductor, RF MEMS, ferroelectric materials and ferromagnetic materials. However, the device realization utilizing the above technologies is directly dependent on the design of individual components meaning that each tunable component needs to be oriented with special technology requiring several complicated layers of layout and customized fabrication processes, which makes the application of tuning technology lack of flexibility and re-productivity. To provide a tuning method with more flexibility, an electrically tunable engineered substrate enabled with patterned Py thin film is proposed in this section. With the tunability realized on the engineered substrate, it is suitable to design arbitrary tunable RF components based on this substrate. The effects of DC current on the permeability of nano-patterned Py thin film is discussed and analyzed, and a new configuration of an engineered substrate for adding bias DC current is evolved from the magneto-dielectric substrate and proposed in the following section.

#### 4.3.1 DC Current Dependent Permeability of Nano-patterned Py Thin

The DC-current dependent permeability of the ferromagnetic material is related to the effective magnetic anisotropy field. Before analyzing the effects of DC current on permeability, the relationship between the DC current and FMR is analyzed. FMR represents the main loss mechanism of the ferromagnetic material, at which the energy is absorbed by the ferromagnetic body. As described in chapter 3, the FMR of the ferromagnetic thin film should be designed as high as possible to allow operation at a high frequency range. From Kittel's formula [80]:



$$f_{FMR} = \frac{\gamma}{2\pi} \sqrt{(H_{bias} + H_{ani} + (N_y - N_z)4\pi M_s)(H_{bias} + H_{ani} + (N_x - N_z)4\pi M_s)} \quad (4-1)$$

where  $H_{bias}$  is the bias field,  $H_{ani}$  is inherent anisotropy field of material,  $\gamma$  is the gyromagnetic ratio,  $(N_y - N_z)$  and  $(N_x - N_z)$  are the contributions to magnetic anisotropy due to the patterned shape anisotropy, and  $M_s$  is the saturation magnetization. The gyromagnetic ratio  $\gamma$  and saturation magnetization and  $4\pi M_s$  which are determined by the type of ferromagnetic material have a fixed value that cannot be changed. The inherent anisotropy field  $H_{ani}$  in Kittel's equation is determined by the quality of the ferromagnetic material. Demagnetizing factors  $(N_y - N_z)$  and  $(N_x - N_z)$  depend on the aspect ratio of length to width of the Py patterns. The bias field  $H_{bias}$  can be created by the DC current or permanent magnet. The maximum Ampere's field contributed from the DC current can be approximately expressed as [81]:

$$H_{dc} = \frac{I}{2w} \quad (4-2)$$

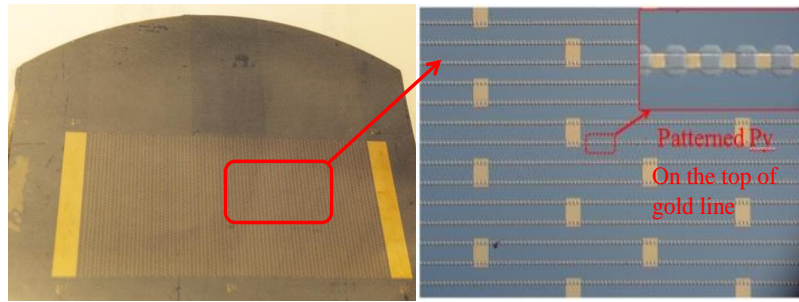
where  $I$  represents the DC current,  $w$  is the width of the DC bias line. Take the 10um width DC bias line as an example ( $H_{dc} = I/2w = 200mA/2 \times 10\mu m = 10KA/m$ ). An estimated inherent and shape magnetic anisotropy of 45.75KA/m from nano-patterned Py thin film under no DC current can be estimated from our group's previous work [82]. The induced 10KA/m magnetic anisotropy generated by 200mA DC current is thus comparable with inherent and shape anisotropy. Therefore the change of the external magnetic field from different DC currents can be used to tune the magnetic anisotropy of ferromagnetic material. And the relative permeability of the ferromagnetic film can be expressed as [83]:

$$\mu_{reff} = 4\pi M_s / H_{eff} + 1 \quad (4-3)$$

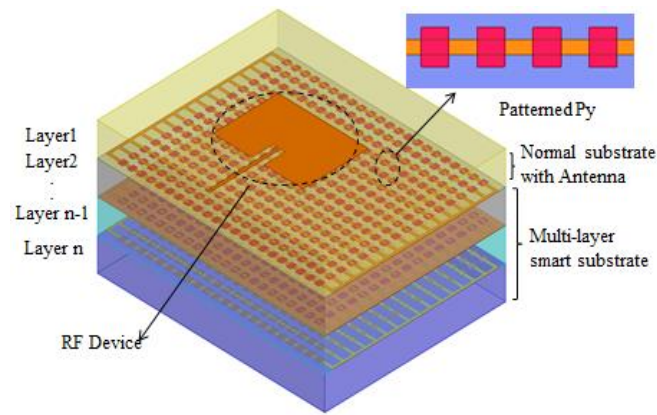
where  $H_{eff}$  is the effective magnetic anisotropy field in the ferromagnetic film. It shows that the effective permeability of the ferromagnetic film is inversely proportional to the effective magnetic anisotropy field  $H_{eff}$ . Since the applied DC current can significantly affect the magnetic anisotropy field along the easy axis, the FMR can thus increase with the increased magnetic anisotropy field, while the effective permeability is decreased. A great amount of experiments [79, 81, 83] have showed that the effective permeability of patterned Py thin film is decreased with increased DC current.

#### 4.3.2 Construction of Electrically Tunable Engineered Substrate

An electrically tunable engineered substrate enabled with patterned Py thin film is proposed in this section. In order to apply DC current on the patterned Py thin film, the structure of engineered substrate shown in Figure4.7 (a) is developed and evolved from the previous magneto-dielectric substrate. Keeping the same patterned Py thin film on the high-resistivity silicon as the magneto-dielectric substrate, an array of DC bias lines with a thickness of 10nm are specially designed and arranged under the patterned Py thin film. Since the gold line arrays have very high conductivity and small dimensions, the extra loss introduced by the gold line can be limited to a tolerable range. The approach of implementing the engineered substrate with RF components is shown in Figure4.7 (b). RF components fabricated on an arbitrary substrate can be bonded with one-layer or multi-layered engineered substrate. The RF components are fabricated with PCB technology while the Py thin film is deposited and patterned using the DC magnetron sputtering method, which provide a flexible approach to design arbitrary tunable RF components.



(a)



(b)

Figure 4.7 (a) Engineered smart substrate with zoom-in view of patterned Py film and DC bias line arrays (b) Application of multi-layer engineered substrate embedded with patterned Py thin film

#### 4.4 Implementation of Tunable Engineered Substrate

Implementation of the engineered substrate with arbitrary RF components is presented in this section. Tunable patch antennas and transmission line based phase shifters are typical devices where the potential of miniaturization and electrical tunability of the engineered substrate are most effectively demonstrated. RF components designed with the engineered substrate can be equivalent to circuit models with a permeability-dependent inductor that can be adjusted by DC current. The resonant frequency of

microstrip resonators can be adjusted by the tunable inductors. Therefore, a variety of tunable RF components based on microstrip resonators can be designed on the engineered substrate. The tunable filter is one of the most considered devices since the resonant frequency of the filter can be adjusted by the tunable inductor. Apart from the antenna, phase shifter, filters, three-port devices such as a balun or a power divider are other representative components which are important in microwave systems. The implementation of different types of tunable RF devices (e.g., antenna, phase shifter, filter, and balun) fabricated on printed circuit boards with the engineered substrate are presented and characterized in this section, which demonstrates the flexibility and a unique method in designing electrically tunable arbitrary RF components on the engineered substrate.

#### 4.4.1 Electrically Tunable Patch Antenna

The antennas always have wide applications in modern wireless communication system. To obtain the tunable property of the engineered substrate, a conventional transmission line fed patch antenna as described in chapter 3 is firstly implemented with the engineered substrate. The equivalent permeability of the whole engineered substrate under different DC currents is derived when matching the resonant frequency of the measurement results with that of the simulation results from the EM models.

##### 4.4.1.1 Measurement of Tunable Patch Antenna

After finishing the fabrication on the LCP substrate, the patch antenna was bonded to the top surface of the engineered substrate as shown in Figure 4.8(a). Combined with two DC probes to supply tunable DC current on the Py film, a Rhode &

Schwarz ZVA67 Network Analyzer was used to measure the resonant frequency of designed patch antenna under different DC currents which is represented by the valley bottom of the return loss. According to the theory behind the patch antenna, the resonant frequency can be roughly calculated as  $f = 0.5L/\sqrt{\mu_r\epsilon_r}$ , where L is the length of antenna;  $\mu_r$  is the equivalent relative permeability of the whole multi-layer substrate. The tunable permeability of the patterned Py thin film exerts an effect on the overall multi-layer substrate; the resonant frequency of the antenna therefore is tuned under different DC current as the performance shown in Figure 4.8 (b). The resonant frequency of the antenna shifted from 2.455GHz to 2.498GHz when DC current is increased from 0mA to 500mA. The return loss initially increased with the increase of DC current and obtained minimum value when DC current went up to 300mA. This is due to the characteristic impedance of the patch antenna being best matched with the fed transmission line at 300mA. The measured performance of the patch antenna also shows that the relative permeability of Py thin film is decreased with the increase of DC current, and a tunable frequency range of 43MHz could be achieved with 500mA current.

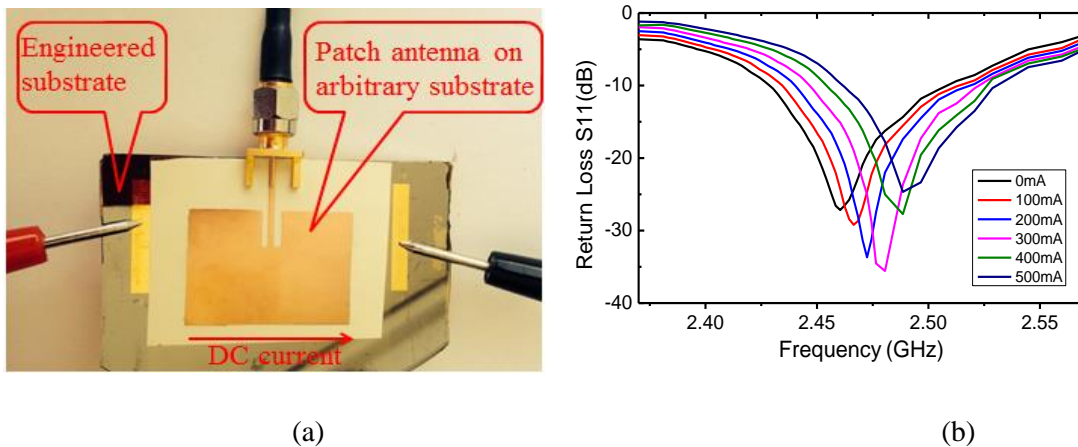


Figure 4.8 (a) Implementation of patch antenna with tunable engineered substrate (b) measured return loss of magnetic antenna under different DC current

#### 4.4.1.2 Equivalent Permeability of Engineered Substrate

With the assistance of equivalent EM models in ANSYS HFSS, equivalent permittivity and permeability of the overall multi-layer substrate can be extracted when the simulated return loss S11 of patch antenna get matched with the measurement results. The equivalent permittivity of the multi-layer substrate is firstly obtained as 7.81 by assigning no magnetic properties to the Py thin film, The equivalent relative permeability of Py thin film under different current is then derived one by one with the matched return loss between the measurement and simulation results. According to the simulation and experimental results, the derived equivalent permeability of the overall multi-layer substrate is listed in Table 4.2.

Table 4.2 Equivalent permeability of the multi-layer substrate with the effects of patterned Py film

DC Current	Resonant Frequency	Equivalent permeability	Equivalent permittivity
No Py	2.52GHz	1	7.81
0mA	2.455GHz	1.14	7.81
100mA	2.463GHz	1.134	7.81
200mA	2.471GHz	1.130	7.81
300mA	2.481Gz	1.123	7.81
400mA	2.49GHz	1.109	7.81
500mA	2.498GHz	1.102	7.81

#### 4.4.2 Tunable Phase Shifter

Similar to the patch antenna, a tunable transmission serving as a phase shifter was firstly fabricated on LCP substrate with a thickness of 100nm and implemented with the engineered substrate as shown in Figure 4.9 (a). The characteristic impedance of a lossless transmission line is equal to the square root ratio of inductance to capacitance  $Z = \sqrt{L/C}$ . The inductance of the transmission line can be adjusted by the tunable equivalent permeability of the overall substrate. When the magnetic property of the multi-layer substrate is changed by the DC current, the phase of transmission line could also be tuned as a phase shifter. Without the presence of the patterned Py film, the transmission line presents a phase shift of  $90^\circ$  at 2.29GHz. Through changing the DC current from 0mA to 400mA, the  $90^\circ$  phase shift of transmission line can shift from 2.15 GHz to 2.21GHz as shown in Figure 4.9(b). Suitably selecting tuning the DC current, a  $90^\circ$  phase shift can be achieved in a desired frequency. It shows that the electrically tunable engineered substrate provides a continuous tuning method.

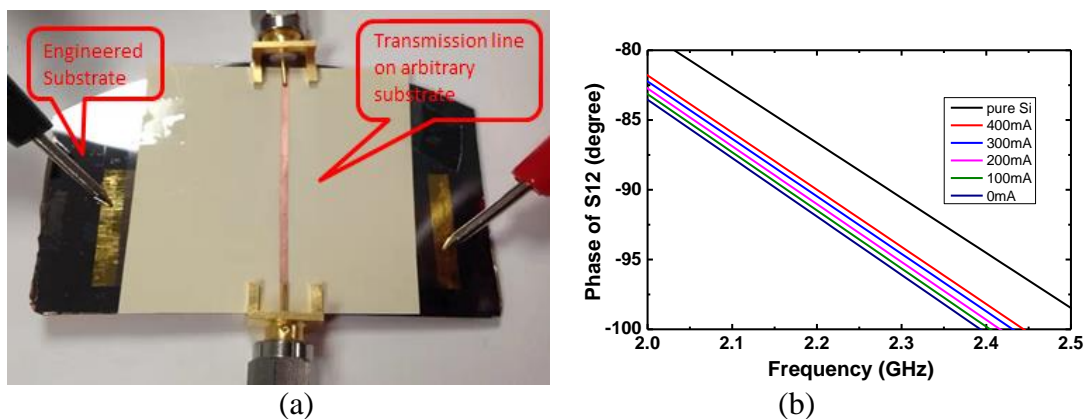


Figure 4.9 (a) Implementation of tunable transmission line based phase shifter on engineered substrate (b) Measured phase of transmission coefficient (S12) under different DC current

### 4.4.3 Tunable Bandpass Filter

#### 4.4.3.1 Introduction

As one of the key components in a transceiver and a receiver to reduce spurious and unexpected signals from the noises or other channels, tunable band-pass filters with compact size and a cost-effective fabrication process are critically needed to satisfy the requirements of reconfigurable RF components in modern wireless communication systems which are small and light weight. The desire for frequency tunability within broadband receiving and transmitting systems usually necessitates switching between multiple fixed-tuned circuits [84]. The use of tunable filters and resonators can reduce losses within complex multiband systems. A lot of tunable filters have been realized with the reconfigurable technologies as examples introduced in the previous section. However, the tunability of all the reported filters are directly dependent on the individual configuration of the filter, which is required to be oriented with customized fabrication process for each specific design. Although compared with different technologies, magnetically tunable inductors with ferromagnetic materials can provide a high quality factor, they cannot meet the miniaturization requirements of the modern communication systems when a large and cumbersome external biased magnetic field is required.

This section presents the implementation of an electrically tunable bandpass filter with the proposed engineered substrate enabled with patterned Permalloy (Py) thin film. The high-permeability Py thin film exhibits a strong current-dependent permeability that can be adjusted by DC current; the equivalent permeability of the engineered substrate thus can be electrically tunable. Planar filter structure has been adopted as a promising



approach to implement compact size. The metamaterial based resonators—split-ring resonators (SRRs) are utilized as the basic structure of the designed filters.

#### 4.4.3.2 SRRs Based Resonators

There are many types of resonators that can be used for designing filters, such as lumped element based resonators, waveguide resonators, dielectric resonators loaded cavities and transmission line resonator .etc. Considering the requirements of compact size and light weight, transmission line based resonators are preferred elements for designing planar-structure filters [85]. The application of metamaterial in filters relies on the resonate-type transmission line. SRRs, as one type of metamaterial resonators, have been developed and derived into quasi-lumped elements for the miniaturization of the planar devices [86]. As shown in Figure4.10 (a) the SRRs are composed of two microstrip line shaped rings separated with a gap, both ends of the rings are loaded with open-stubs oriented at opposite sides. Equivalent inductance and capacitance can be estimated when significant coupling between the two rings exists [87]. An equivalent LC resonant circuit for the structure of SRRs is shown in Figure4.10 (b).

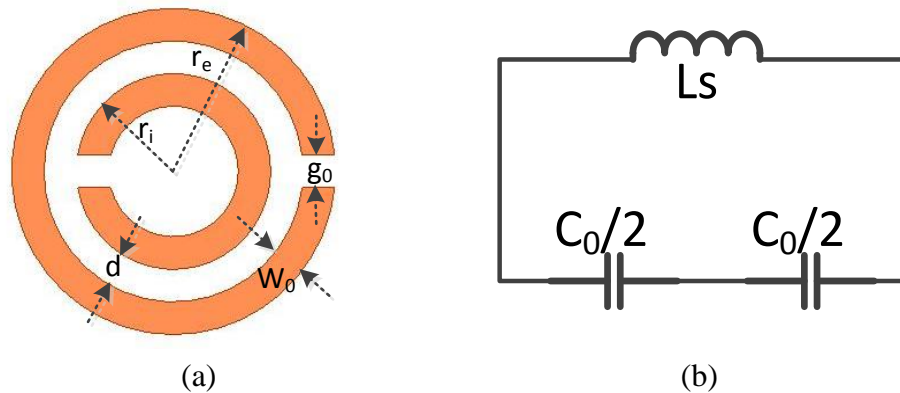


Figure 4.10 (a) Schematic view of SRRs (b) Equivalent lumped circuit model

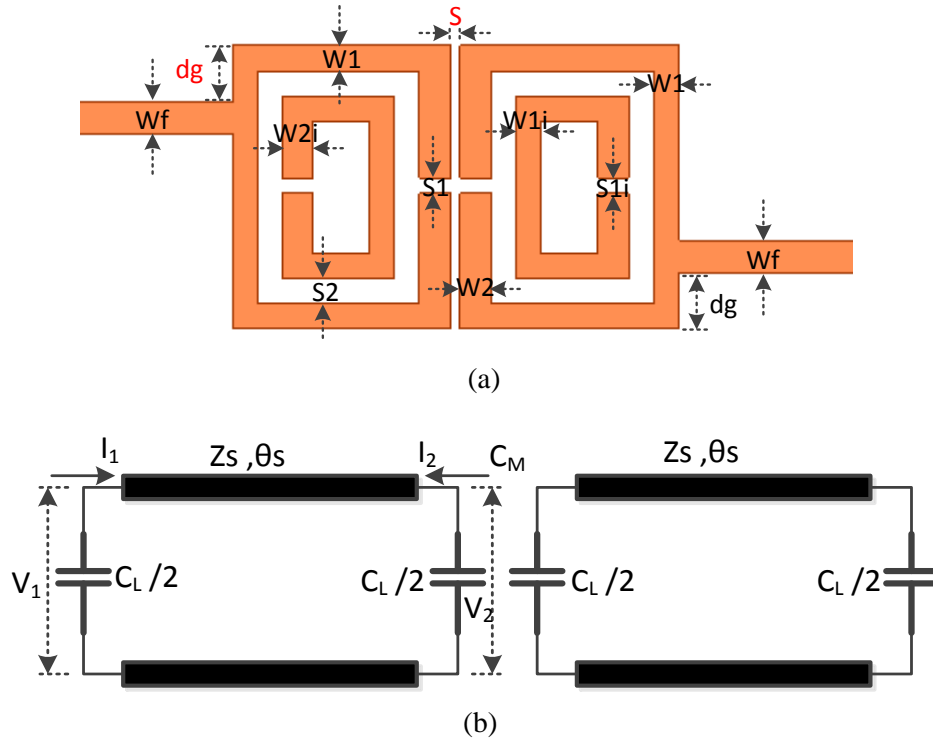
The inductance  $L_s$  is the self-inductance of metal rings, and the capacitance  $C_0/2$  is contributed from the gap between the rings and the split regions of each half ring, it can be expressed with  $C_0 = 2\pi r_0 C_p$ , where  $r_0 = (r_e + r_i)/2$  is the average radius of SRRs,  $C_p$  is the capacitance per unit length along the gap between SRRs, which has been proven in [87]. The capacitance of each half of SRRs is connected in series; the resonant frequency  $f_0$  of the SRRs is given by.

$$f_0 = 1/\sqrt{\pi(L_s C_0)} = 1/(0.45\sqrt{\pi r_0 L_s C_p}) \quad (4-5)$$

Compared with a straight transmission, the SRRs based resonators have more capacitance which is introduced from the coupling rings and the gap of split rings. It also shows that the required resonant wavelength of SRRs is smaller than half-wavelength transmission line resonators at the same resonant frequency, which makes SRRs a good choice for compact filter design.

#### 4.4.3.2 SRRs Based Bandpass Filter

SRRs can be used for band-pass filter design by putting several SRRs together with certain directions, gaps or combing with some other elements [88]. A simplified narrow band-pass filter designed with two-section rectangular shaped SRRs is shown in Figure 4.11 (a). These two SRRs are arranged side by side with a gap facing with each other. The excitation of the SRRs based filter can be generated from part of the transmission line. The serial SRRs are expressed as lossless transmission line resonator loaded with two capacitors in the proposed SRRs based band-pass filter. The equivalent circuit model of the filter is shown in Figure 4.11 (b).



**Figure 4.11:** (a) SRRs based band-pass filter with  $W_f = 0.95mm$  ,  $W_1 = 0.8mm$  ,  $W_2 = 0.9mm$  ,  $W_{1i} = 0.8mm$  ,  $W_{2i} = 0.9mm$  ,  $S_1 = 0.4mm$  ,  $S_{1i} = 0.4mm$  ,  $S_2 = 0.5mm$ ,  $dg = 2.2mm$ ,  $S = 0.3mm$  (b) Equivalent circuit model of filter

As described in Figure4.11. (b),  $C_M$  is mutual capacitance between two SRRs,  $C_L$  is the loaded capacitance from the split gap,  $Z_s$  and  $\theta_s$  represent the characteristic impedance and electrical length of the unloaded transmission line respectively. According to the  $ABCD$  parameters of  $\pi$ -Network transmission matrix [89], the input and output response of the open end transmission line resonators can be described by

$$\begin{bmatrix} V_1 \\ I_1 \end{bmatrix} = \begin{bmatrix} A & B \\ C & D \end{bmatrix} \cdot \begin{bmatrix} V_2 \\ -I_2 \end{bmatrix} \quad (4-6)$$

$$A = D = \cos\theta_s - 0.5\omega C_L Z_s \sin\theta_s \quad (4-7)$$

$$B = jZ_s \sin\theta_s \quad (4-8)$$

$$C = j(\omega C_L Z_s \cos\theta_s + 1/Z_s \sin\theta_s - 1/4\omega^2 C_L^2 Z_s \sin\theta_s) \quad (4-9)$$

where  $\omega$  is the angular frequency. For open end resonators, the standing wave is subject to the boundary condition with  $I_1 = I_2 = 0$  at resonant frequency. Then certain network parameters can be determined, and  $A = V_1/V_2 = -1$  at first resonant frequency  $f_0$ ,  $A = V_1/V_2 = 1$  at first spurious resonant frequency  $f_1$ . Solving these equations with the values in (4-7), (4-9), the two Eigen equations yields: [90]

$$\theta_{s0} = 2 \tan^{-1}(1/\pi f_0 Z_s C_L) \quad (4-10)$$

$$\theta_{s1} = 2\pi - 2 \tan^{-1}(\pi f_1 Z_s C_L) \quad (4-11)$$

where  $\theta_{s0}$  and  $\theta_{s1}$  represent the electrical length of the SRRs at the first resonant frequency and first spurious resonant frequency respectively. When loaded capacitance  $C_L$  become zero, the equation (4-10) and (4-11) yields:  $\theta_{s0} = \pi$ ,  $\theta_{s1} = 2\pi$ , which functions as open end half-wavelength resonators. While increasing the loading capacitance, the resonant frequency can shift to a lower value with the same electrical length. It indicates that SRRs is an effective structure to design a compact filter.

#### 4.4.3. Bandwidth Optimization on Bandpass Filter

The coupling between adjacent SRRs has been neglected in the former equations. The equations to analyze the fundamental resonant frequency of SRRs only give a rough estimation of the filter design. To get the desired performance, the bandpass filter designed on the engineered substrate is optimized in the EM simulator ANSYS HFSS. The final optimization dimensions of the bandpass filter are shown in Figure 4.10(a). The bandwidth and stopband rejection are the two critical factors for a narrow-bandwidth bandpass filter. This section will give a description of the optimization of coupling distance and feeding position, which are the main factors to determine the bandwidth and stopband rejection of the filter respectively. It has been proven by previous studies [91]

that two peaks of resonant point can be obtained by two different coupling modes- electric wall and magnetic wall, when the coupling resonators are over-coupled. Taking the mutual capacitance into consideration, two resonant frequencies at different modes can be expressed as [92]

$$f_{p1} = \frac{1}{2\pi\sqrt{L_s(C_L+C_M)}} \quad (4-12)$$

$$f_{p2} = \frac{1}{2\pi\sqrt{L_s(C_L-C_M)}} \quad (4-13)$$

where  $f_{p1}$  and  $f_{p2}$  represents resonant frequencies at different modes. Using  $f_{p1}$ ,  $f_{p2}$ , the coupling coefficient  $k$  can be calculated as

$$k = \frac{f_{p2}^2 - f_{p1}^2}{f_{p2}^2 + f_{p1}^2} \quad (4-14)$$

The bandwidth of the filter is expected to be inversely proportional to the coupling coefficient  $k$ , while the insertion loss follows the opposite trend. Changing the coupling distance  $S$ , the relations of the bandwidth between the coupling gap distance  $S$  and coupling coefficient  $k$  are obtained as shown in Figure 4.12. Choosing a balance between the insertion loss and bandwidth, the finally optimized coupling distance  $S$  is 0.3mm.

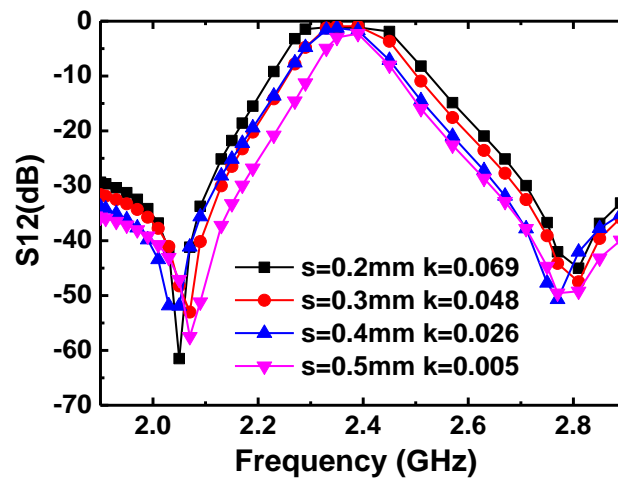


Figure 4.12 Simulated coupling coefficient with different gap

#### 4.4.3.2 Stopband Rejection Optimization

The stopband rejection of the filter is mainly determined by the feed position. There are two types of relative feed points for half-wavelength transmission line resonators, symmetric or screw symmetric [93]. The electrical length of the upper and lower paths to the feed point is not the same when the SRRs take the screw symmetric feeding method, two transmission zeros could be generated near the passband and thus increase the stopband rejection. To observe the tunable range of the filter, a narrow band-pass filter is desired. The proposed filter is designed with the screw symmetric feeding method as shown in Figure 4.11 (a). Taking an optimization on the relative feeding points of the screw asymmetric structure, different transmission zeros could be generated. As shown in Figure 4.13, the larger the difference of the electrical delay between the upper and lower paths, the closer the two transmission zeros. Also a sharp edge could be obtained with less insertion loss. The last optimized feeding position is  $dg = 2.2\text{mm}$  near the edge with an insertion 0.8dB.

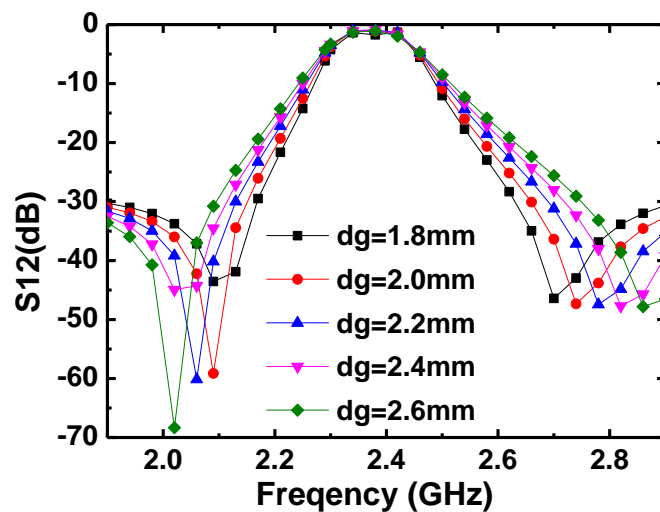


Figure 4.13 Comparison of simulated transmission zeros with different feed structure parameters

#### 4.4.3.3 Simulation Results of Tunable Bandpass Filter

With the equivalent permeability of the overall multi-layer substrate listed in Table 4.2, the tunable properties of the bandpass filter designed on the engineered substrate can be simulated with EM models in ANSYS HFSS and the results are shown in Figure4.14. It shows that the center frequency of the simulated bandpass filter can shift from 2.28GHz to 2.35GHz continuously with the change of equivalent permeability of the overall multi-layer substrate.

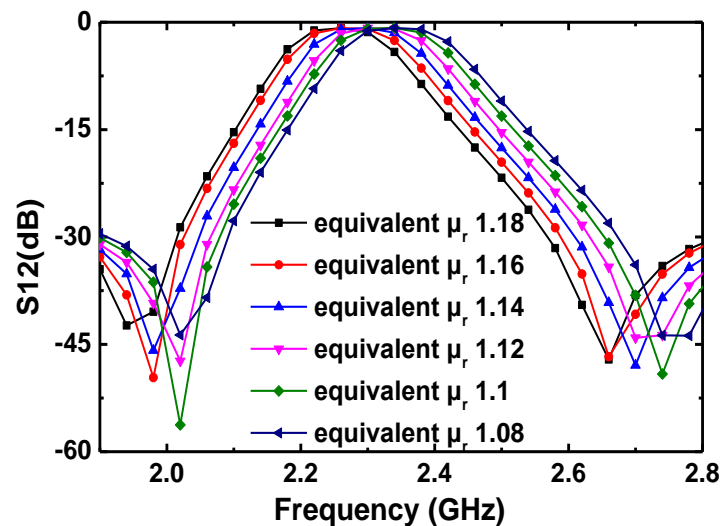


Figure4.14 Simulated transmission coefficient of bandpass filter under the equivalent permeability of different DC current

#### 4.4.3.4 Measurement Results of Bandpass Filter

The tunable property of the developed filter could be directly achieved through tuning the RF characteristics of the engineered substrate with DC current; the filter thus can be designed and fabricated with arbitrary state of art technology. The implementation of the bandpass filter with the engineered substrate with patterned Py thin film is shown in Figure4.15. The bandpass filter is fabricated separately on a liquid crystal polymer

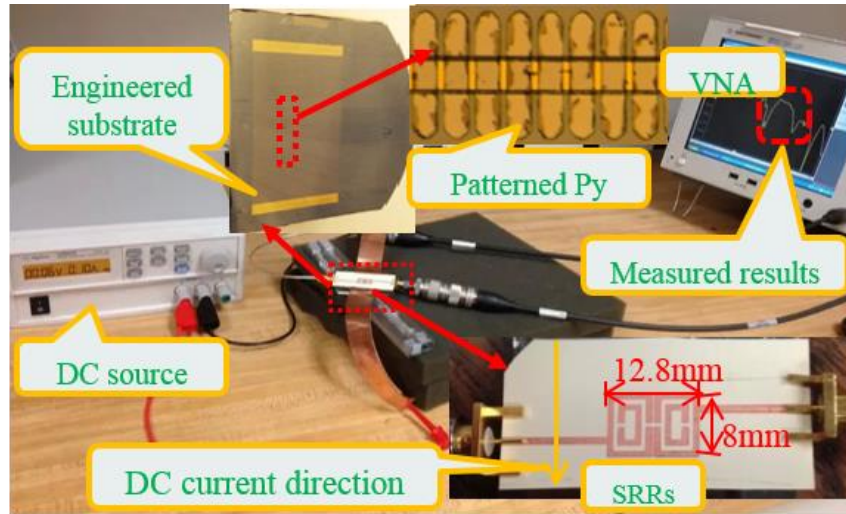


Figure 4.15 Implementation of bandpass filter on engineered substrate with patterned Py thin film and zoom-in view of SRRs and Py patterns on engineered substrate

(LCP) substrate with a thickness of 100 $\mu$ m and then bonded together with the engineered substrate. This described engineered smart substrate is made of patterned 100nm thick Py thin films on high resistivity silicon, Py was grown by DC magnetron sputtering method and was patterned as an array of 15 $\mu$ m  $\times$  40 $\mu$ m rectangles with a 5 $\mu$ m gap among them to create self-biased magnetic field. An array of gold lines with thickness of 10nm was deposited between the Py patterns and silicon to provide a DC current path for electrically tuning.

The final optimized dimensions of the filter are 12.8mm  $\times$  8mm as shown in Figure 4.15. Two feeding lines are extended to the edge of the substrate for convenient measurement, and the proposed filter is measured with a network analyzer in the frequency range of 0.1- 4GHz. Applying DC current from 0mA to 800mA through the gold bias lines, the center frequency of the band-pass filter can shift from 2.42GHz to 2.56GHz continuously as shown in Figure 4.16 with an insertion loss of less than 5dB. It



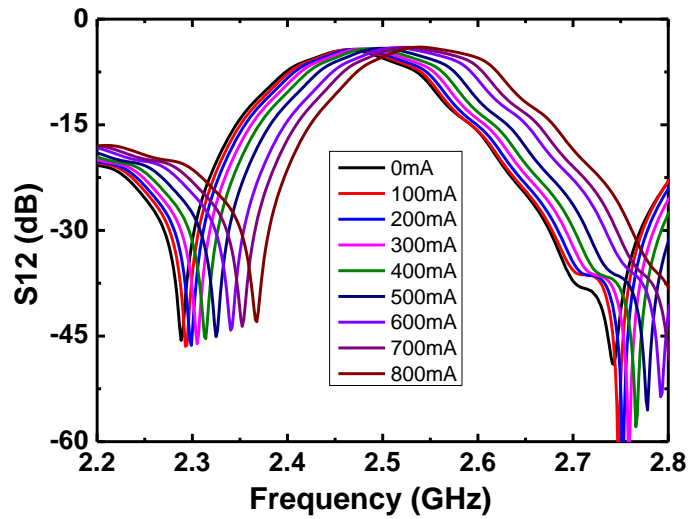


Figure4.16 Measured frequency shift of band-pass filter with engineered substrate under different DC current

showed that when the DC current is less than 500mA, the tunable range for each increased step of 100mA is around 7MHz, which is very small. When the DC current is more than 400mA, the tuned center frequency shift of 20MHz can be achieved with every increased step of 100mA DC current applied. The resonant frequency of the bandpass filter is expressed as  $f_0 = 1/2\pi\sqrt{LC}$ . As described in previous section, the effective permeability of the engineered substrate decreased with increased DC current, since the inductance density of the implemented filter is proportional to the effective permeability of the overall multi-layer substrate. The center frequency of the bandpass filter was thus tuned to a higher frequency with the increased DC current. The measurement results show that the center frequency shift of the bandpass filter implemented with the engineered substrate can be tuned successfully with applied DC current. And a larger tunability could be achieved when applied DC current becomes larger than 500mA.

## 4.4.4 Tunable Bandpass Filtering Balun

### 4.4.4.1 Introduction

In the receiver of wireless communication systems, the single-ended input signal from the antenna is first passed through a low noise amplifier (LNA) which has a differential two-port end. A transformer is always required to connect the single-ended port with the differential ports. A balun is widely used to convert an unbalanced signal (a single-ended signal) into balanced signals (differential signals with  $180^\circ$  in-phase) [94]. Generally the received signal from the antenna is processed through a bandpass filter to reduce the noise and unexpected signals from other channels, and then connects to a balun before the connection with the LNA. The single-end signal from the antenna is thus transformed into a differential mode as the input of the LNA. Integrating the bandpass filter and balun into a single device is highly desired in communication systems, which can be an effective approach to reduce the size and cost of the system. To demonstrate the efficacy of developing tunable miniaturized RF device with patterned Py thin film, the design and implementation of a bandpass filtering balun with the engineered substrate is presented in this section.

### 4.4.4.2 Design Theory of BPF-Balun

The theory of designing a bandpass filtering balun with a simple structure is introduced in this part. Conventional multiple coupled straight lines with a skew symmetric feeding method (port 1 and port 3) [95] as shown in Figure 4.17 (a) is utilized for filter design. Another filter with symmetric feeding between port 1 and port 2 can also be achieved on the same structure as shown in Figure 4.17 (a). This symmetric feeding

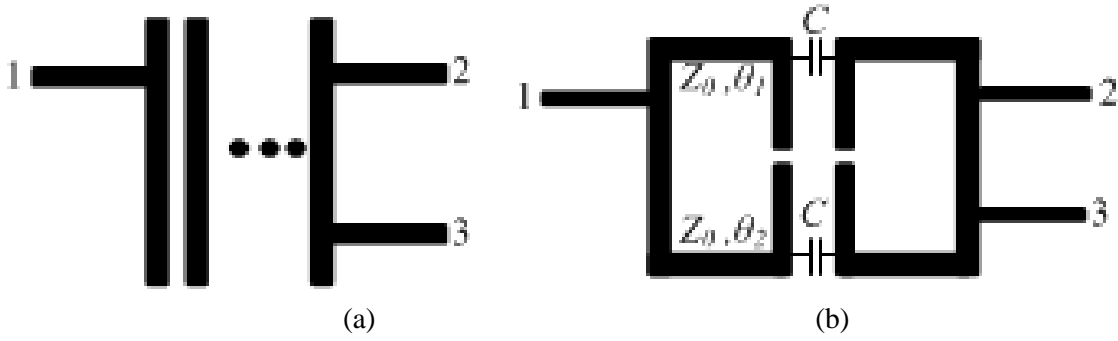


Figure 4.17 (a) Conventional coupled straight line and (b) Capacitive loaded coupled meander line

filter has a  $180^\circ$  phase difference with the filter fed between port 2 and port 3. Feeding with both symmetric and skew symmetric methods, the input signal from port 1 is divided into differential signals at port 2 and port 3 to function as a balun. The structure in Figure 4.17(a) can be further developed into two coupling split ring resonators as shown in Figure 4.17 (b). Having port 2 matched with a  $50 \Omega$  load, the equivalent transmission matrix for upper and lower paths with the skew symmetric feedings (port 1 and 3) can be expressed with the ABCD parameters [96]:

$$\begin{bmatrix} A_u & B_u \\ C_u & D_u \end{bmatrix} = \begin{bmatrix} \cos(\theta_1 + \theta_2) + \frac{1}{\omega Z_0 C} \sin\theta_1 \cos\theta_2 & jZ_0 \sin(\theta_1 + \theta_2) - j \frac{\cos\theta_1 \cos\theta_2}{\omega C} \\ j \frac{1}{Z_0} \sin(\theta_1 + \theta_2) + j \frac{1}{\omega Z_0^2 C} \sin\theta_1 \sin\theta_2 & \cos(\theta_1 + \theta_2) + \frac{1}{\omega Z_0 C} \cos\theta_1 \sin\theta_2 \end{bmatrix} \quad (4-15)$$

$$\begin{bmatrix} A_l & B_l \\ C_l & D_l \end{bmatrix} = \begin{bmatrix} \cos(\theta_1 + \theta_2) + \frac{1}{\omega Z_0 C} \cos\theta_1 \sin\theta_2 & jZ_0 \sin(\theta_1 + \theta_2) - j \frac{\cos\theta_1 \cos\theta_2}{\omega C} \\ j \frac{1}{Z_0} \sin(\theta_1 + \theta_2) + j \frac{1}{\omega Z_0^2 C} \sin\theta_1 \sin\theta_2 & \cos(\theta_1 + \theta_2) + \frac{1}{\omega Z_0 C} \sin\theta_1 \cos\theta_2 \end{bmatrix} \quad (4-16)$$

According to equation (4-15) and (4-16),  $A_u + A_l = D_u + D_l$ ,  $B_u = B_l$ , and  $C_u = C_l$ , for the transmission matrix of the whole circuit with ABCD parameters, the upper and lower

paths can be rewritten as [97]

$$\begin{aligned} \begin{bmatrix} A & B \\ C & D \end{bmatrix} &= \begin{bmatrix} \frac{A_u B_l + A_l B_u}{2} & \frac{B_u B_l}{2} \\ \frac{(A_u B_l + A_l B_u)(B_u D_l + B_l D_u) - (B_u + B_l)^2}{(B_u + B_l) B_u B_l} & \frac{B_u D_l + B_l D_u}{(B_u + B_l)} \end{bmatrix} \\ &= \begin{bmatrix} \frac{A_u + A_l}{2} & \frac{B_u}{2} \\ \frac{(A_u + A_l)^2 - 4}{2 B_u} & \frac{A_u + A_l}{2} \end{bmatrix} \end{aligned} \quad (4-17)$$

The total electrical length of a resonator is equal to  $\theta_1 + \theta_2 = \pi$  in the passband [98], so the transmission matrix can be derived with substituting the value in equation (4-17) from equations (4-15) and (4-16)

$$\begin{bmatrix} A & B \\ C & D \end{bmatrix} = \begin{bmatrix} -1 & -j \frac{\cos^2 \theta_1}{2\omega C} \\ 0 & -1 \end{bmatrix} \quad (4-18)$$

S parameters can be easily derived from the ABCD parameters through network-parameters conversion. The transmission coefficient between the skew symmetric feedings is:

$$S_{31} = \frac{-1}{2 - j \cos^2 \theta_1 / 2\omega C Z_l} \quad (4-19)$$

A similar method can be applied to the symmetric feeding mechanism (port 1 and port 2) and the derived equivalent ABCD parameters are

$$\begin{bmatrix} A & B \\ C & D \end{bmatrix} = \begin{bmatrix} 1 & -j \frac{\cos^2 \theta_1}{2\omega C} \\ 0 & 1 \end{bmatrix} \quad (4-20)$$

The transmission coefficient of the symmetric feeding is

$$S_{21} = \frac{1}{2 - j \cos^2 \theta_1 / 2\omega C Z_l} \quad (4-21)$$

As the derived transmission coefficient shown in equation (4-19) and (4-21), the transmitted power from port 1 can be divided into two parts at two out ports with the

same magnitude but  $180^\circ$  out-of-phase. Therefore, this proposed simple structure can be used for the design of a BPF-Balun on the engineered substrate.

#### 4.4.4.3 Simulation Results of BPF-Balun

According to the previously introduced theory, the structure which is fed with both symmetric and screw symmetric ports can be developed into a BPF-balun. The BPF-balun is initially designed and simulated with an EM model in ANSYS HFSS. The Roger 4350 ( $\epsilon_r = 3.66$ ,  $\tan\delta = 0.004$ ) with a thickness of 100um is selected as the basic substrate for the BPF-balun. The final optimized dimension of the BPF-balun with a center resonant frequency of 1.57GHz is shown in Figure4.18.

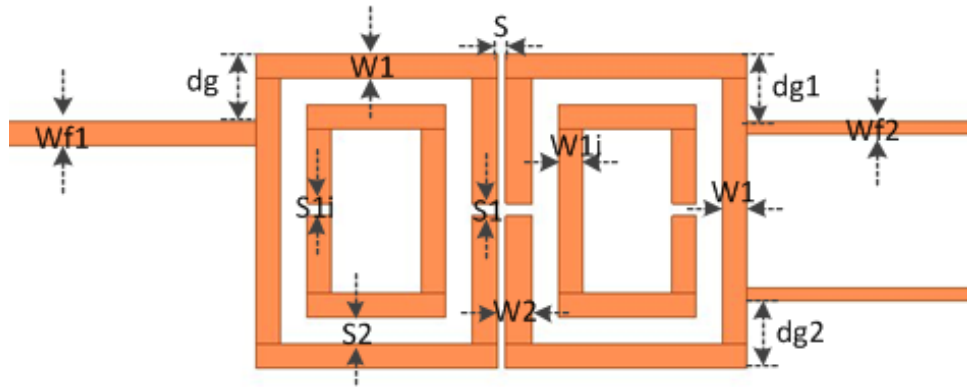
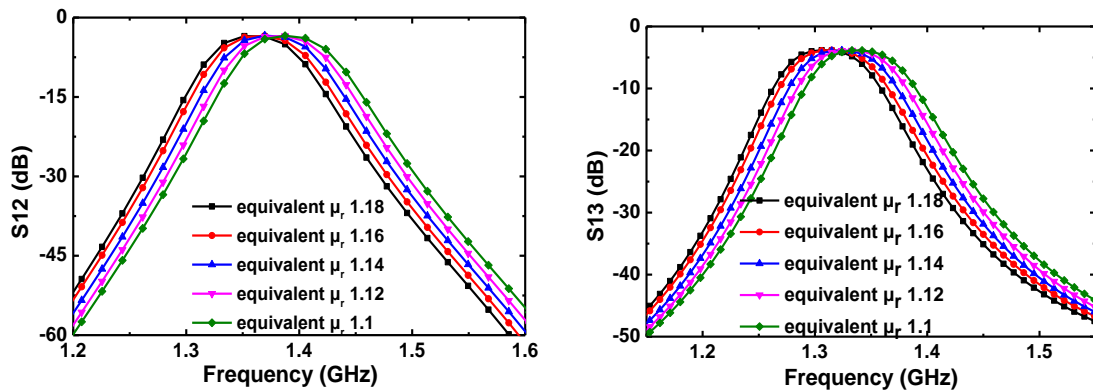


Figure4.18 Optimized dimension of BPF-balun in ANSYS HFSS with  $W_{f1} = 1.05mm$  ,  $W_{f2} = 0.55mm$  ,  $W_1 = 1mm$  ,  $W_2 = 1mm$  ,  $W_{1i} = 0.95mm$  ,  $S = 0.3mm$  ,  $S_{1i} = 0.3mm$  ,  $S_2 = 1.1mm$ ,  $dg = 2.8mm$ ,  $dg1 = 3mm$ ,  $dg2 = 2.9mm$

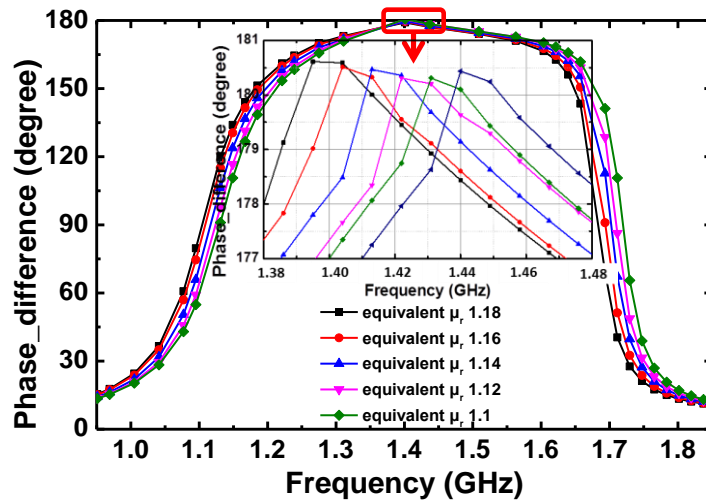
Similar to the tunable bandpass filter, the tunable performance of the BPF-balun can be simulated and optimized in HFSS with the equivalent relative permeability from the previous results in Table 4.2. The simulated transmission coefficients of the input between the two outputs are shown in Figure4.19 (a) and (b) respectively, and the phase

imbalance between the two balanced ports is shown in Figure4.19(c). The simulated results show that the center frequency of the BPF-balun can be tuned from 1.38GHz to 1.48GHz with the changed equivalent permeability of the overall substrate. The simulation results showed that the BPF-balun can be tuned with the similar tendency as the bandpass filter.



(a)

(b)



(c)

Figure4.19 (a) Simulated tunable transmission coefficient  $S_{12}$  with symmetric feeding (b) Tunable transmission coefficient  $S_{13}$  with skew symmetric feeding (c) Phase imbalance between two balanced ports

#### 4.4.4.3 Measurement Results of BPF-Balun

The BPF-balun is fabricated with PCB technology separately on Roger 4350 RF substrate ( $\epsilon_r = 3.66$ ,  $\tan\delta = 0.004$ ) with a thickness of 100 $\mu\text{m}$ . The Roger 4350 substrate is then bonded on the top surface of the engineered substrate. The implementation of the BPF-balun with the engineered substrate and a zoomed-in view of the patterned Py thin film on Silicon are shown in Figure 4.20. DC current is applied through the DC bias lines under Py patterns to tune its permeability which in turn shifts the center frequency of the developed BPF-balun. The performance of the designed BPF-balun is measured with a Vector Network Analyzer (VNA). The transmission coefficients of the unbalanced port are measured twice with one balanced port and the other one matched with a 50  $\Omega$  load. The measured transmission coefficients and phase imbalance between the two balanced ports are shown in Figure 4.21 (a), Figure 4.21 (b) and Figure 4.21 (c).

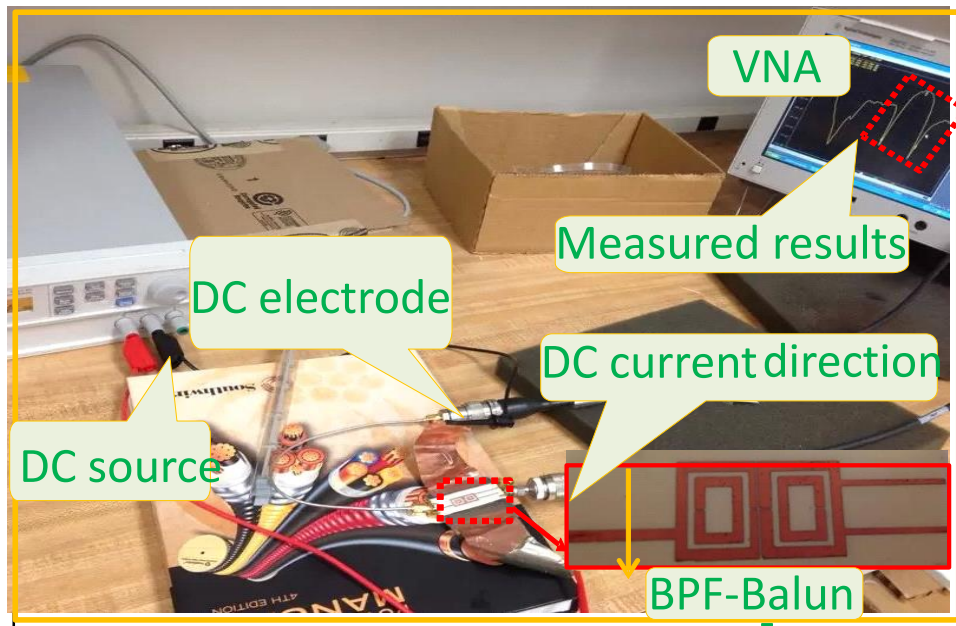
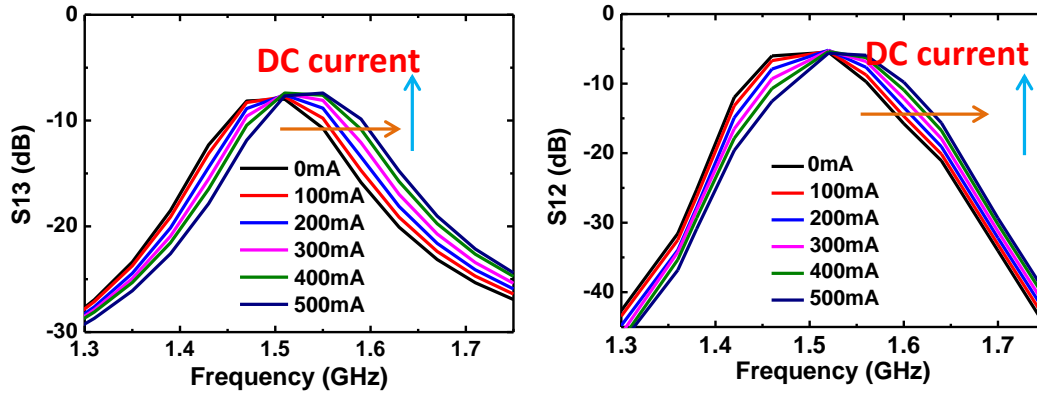


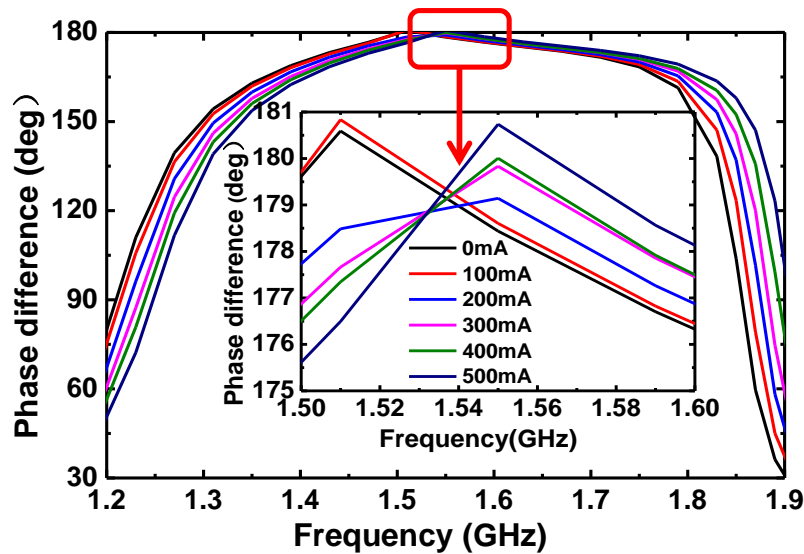
Figure 4.20 Implementation of tunable BPF-Balun with engineered substrate and zoom in view of Py patterns on silicon substrate and BPF-Balun on Rogers 4350 substrate

The measurement results show that the center frequency of the BPF-Balun implemented on the engineered substrate can be tuned from 1.49GHz to 1.545GHz when the applied DC current is increased from 0mA to 500mA which generated a small amount of power (32mW with 500mA DC current), the power could be further reduced by using



(a)

(b)



(c)

Figure 4.21 (a) Tunable transmission coefficient  $S_{12}$  with symmetric feeding, (b) Tunable transmission coefficient  $S_{13}$  with skew symmetric feeding (c) Phase imbalance between two balanced ports



wider bias lines. Within the tunable range, the magnitude imbalance and phase difference are within 0.5dB and  $180^\circ \pm 5^\circ$ . The applied DC current generated an external static magnetic field that added to the in-plane anisotropy field of the Py thin film, which in turn increased the FMR  $f_r$  and also decreased the permeability value. The inductance density of the BPF-balun is changed accordingly with the equivalent permeability of the engineered substrate embedded with Py patterns. The center resonant frequency of the BPF-balun is thus tunable and shifts to a higher frequency with the gradually increased DC current. The results agree well with the magnetic properties of the patterned Py thin film. Compared to the simulation results, the measured resonant frequency is higher than the simulation results, which is partly due to the air gap between the patterned Py thin film and the Roger 4350 substrate.

#### 4.5 Conclusions

In this chapter, a novel electrically tunable engineered substrate with patterned Py thin film was presented to design arbitrary RF components. Arrays of DC bias lines were specially arranged under the patterned Py thin film. The patterned Py thin film is prepared with a DC magnetron sputtering approach on high-resistivity silicon while the RF components can be fabricated independently on any substrate with PCB technology. The implementation of the tunable RF components was achieved through bonding the RF components on an arbitrary substrate onto the top surface of the engineered substrate, which provides a cost effective and flexible method to design arbitrary tunable devices with PCB technology and the engineered substrate. The electrically tunable property of the engineered substrate was affected by the magnetic properties of the patterned Py thin film under different biased DC current. Several different types of RF components (e.g.

one-port patch antenna, two-port phase shifter, two-port band-pass filter, three-port band-pass filtering balun) were modeled, simulated and measured with the engineered substrate to verify the tunable property of the engineered substrate. According to the performance of the bandpass filter and BPF balun, the measured resonant frequency is little higher than the simulation results. This is partly due to the bonding air gap between the engineered substrate and the PCB technology developed substrate. Although the consumption of DC power is small, the applied DC current is still too large to be applied in practical applications, which can be solved with an improved layout on the engineered substrate in future work.

## CHAPTER 5

### CHARACTERISTIC ANALYSIS OF ENGINEERED SUBSTRATE

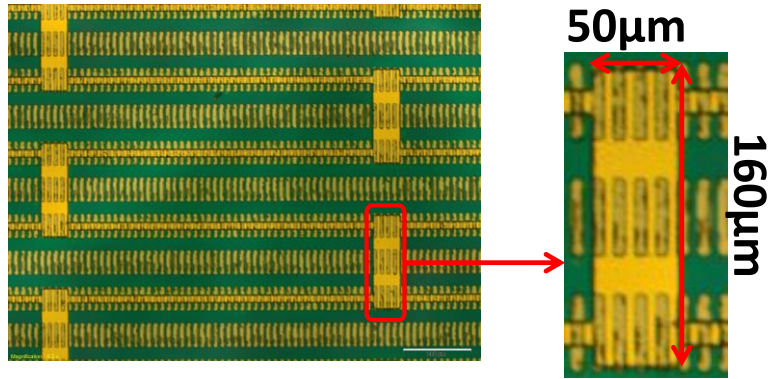
#### 5.1 Introduction

The implementation of the engineered substrate with various passive RF components has demonstrated the tunable property of the engineered substrate for arbitrary RF components. Generally the performance and tunable properties of devices is related to the characteristics of the engineered substrate which is affected by the layout of DC bias lines and patterned Py thin film. In this chapter, the characteristics of the engineered substrate and the approaches to improving the performance of RF devices are discussed and analyzed.

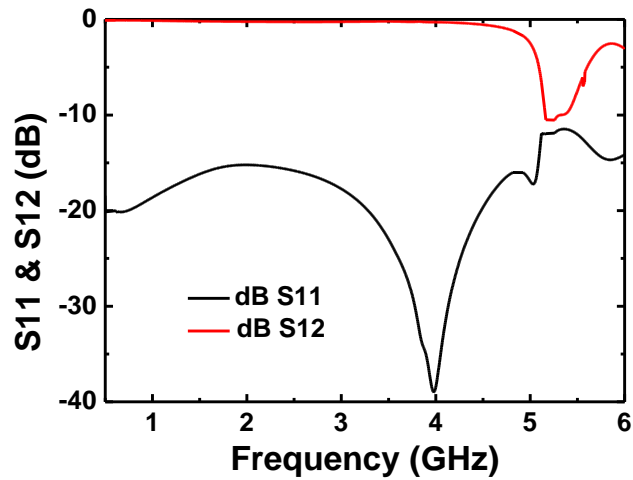
#### 5.2 Limitations of the Implementation with Engineered Substrate

##### 5.2.1 Band Gap Effects of DC Bias Lines

The working frequency of RF components on the engineered substrate is limited by the layout of the DC bias lines. The layout of the DC bias lines on the substrate shown in Figure 5.1, there are large metal plates with the dimensions of  $50\mu\text{m}$  by  $160\mu\text{m}$  arranged between two bias lines along the length of bias line. The DC bias line only has a width of  $10\mu\text{m}$  which is too small to extend into several tens of millimeters, and the distributed metal plates can work in case there are broken bias lines in certain area. The layer of DC bias lines for tuning patterned Py thin film works as an electromagnetic band



(a)



(b)

Figure 5.1 (a) Layout of DC bias line under patterned Py thin film (b) Simulated EBG effects of DC bias lines on engineered substrate

gap (EBG) surface after a certain frequency. The behavior of the independent DC bias line can be treated as an inductor while the coupling effect between nearby bias lines and the disconnected metal plates can be represented by the capacitor, which consisted of a low pass filter. Therefore, the layer of DC bias lines can support the transmission of low-frequency electromagnetic waves while reflecting high-frequency waves after a certain

frequency. The simulated EBG effect with the engineered substrate is shown in Figure 5.1. The distance between the large metal plates is around 1.2mm and the arrayed DC bias lines have 10 $\mu$ m width with a gap of 110 $\mu$ m. With current designing parameters for the layout of DC bias line, the simulated EBG effects of the engineered substrate due to the layout of the DC bias lines is around 5GHz. Reducing the number of DC bias lines and increasing the distance of the distributed large metal plates, the band gap effects can be reduced and shift to a higher frequency range. The operating frequency of RF components designed on the engineered substrate should be below the EBG effects.

### 5.2.2 FMR of Patterned Py Thin Film

Besides the EBG effects of the DC bias lines on the engineered substrate, Py thin film determined ferromagnetic resonant frequency (FMR) limits the maximum operating frequency of RF devices on the engineered substrate. According to the distribution of magnetic anisotropy field in the magnetic poles that introduced in the previous chapter, increasing the shape anisotropy field of Py thin film through a big margin which introduced from patterned slim bars is an effective approach to increasing the FMR of Py thin film while reducing the loss of magnetic material keeping it in a tolerable range. Properly patterned Py thin film can be build in high shape anisotropy field to provide self-biasing field for its application in high frequency ranges. The previous research in our laboratory has shown that the nano-patterned Py thin film can increase the FMR up to 6.3GHz [81]. Compared to the nano-scaled patterned Py thin film, the dimension of the engineered substrate is too large to have nano-scaled patterned thin film. In order to reduce the deposition time and have the patterned Py thin film applied on a large scale engineered substrate, the patterned dimensions of Py thin film is optimized to have a

micro-patterned size instead of a nano-patterned size. The patterned dimension of Py thin film has direct effects on the anisotropy field of material as well as the FMR. In order to analyze the effects of different patterning size on the anisotropy field of Py thin film, two patterned Py thin film with a thickness of 100nm are deposited on the silicon substrate: one pattern has a dimension of  $25\mu\text{m}$  by  $10\mu\text{m}$  with  $5\mu\text{m}$  gap space, and the other one is  $45\mu\text{m}$  by  $5\mu\text{m}$  with  $5\mu\text{m}$  gap space. The optical images of patterned Py thin films are shown in Figure5.2 (a) and Figure5.2 (b).

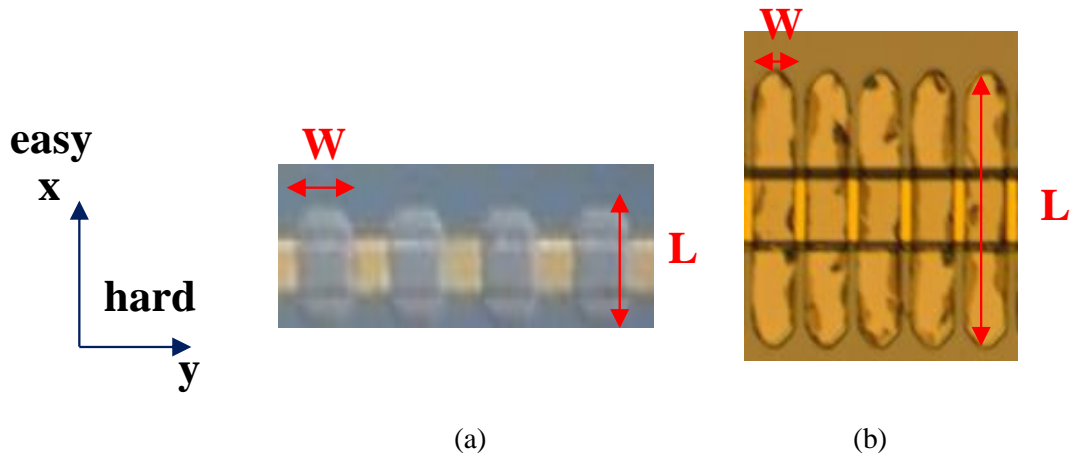


Figure5.2 Optical image of (a) Patterned Py film with length of  $25\mu\text{m}$  and width of  $10\mu\text{m}$ , and (b) Patterned Py film with length of  $45\mu\text{m}$  and width of  $5\mu\text{m}$

The effects of different Py patterning geometries on in-plane anisotropy field is simulated and analyzed with a finite element micro-magnetic simulator (NMAG). The patterned slim shape in the Py thin film can provide a big margin between two ends of the shape to decrease the demagnetizing field and, therefore contribute more shape anisotropy field so as to improve the total in-plane anisotropy field of the Py thin film. The simulated variations of in-plane anisotropy fields along the hard axis of the Py thin

film with the angular dependences of the romance ratio ( $M/M_s$ ) for different patterning film size are shown in Figure 5.3.

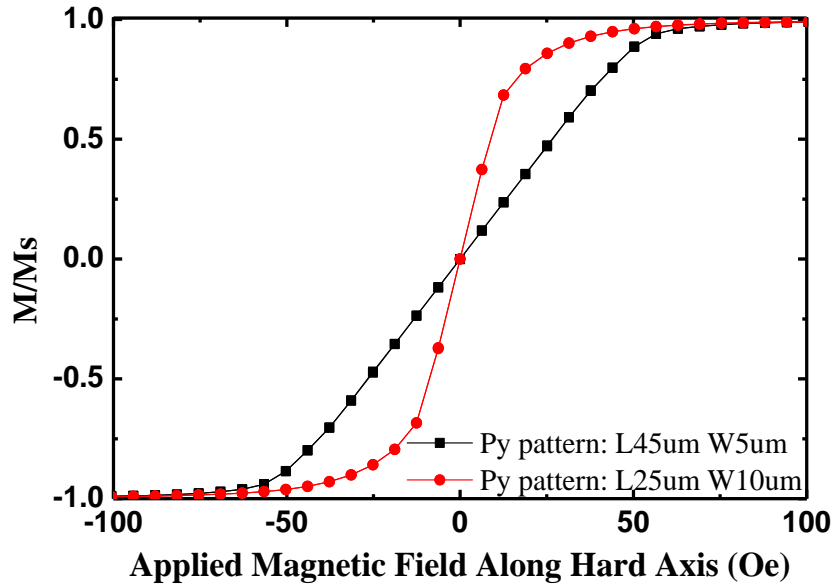


Figure5.3 Variations of in-plane anisotropic field with the angular dependences of the romance ratio ( $M/ M_s$ ) with different Py pattern sizes

The simulation results show that the effective anisotropy fields are increased with the increased length-to-width ratio ( $L/W$ ) of the Py patterns. And the saturation magnetization field  $M_s$  of patterned Py film is increased with the decrease of length-to-width ratio on patterns. The simulation result confirms the tendency of the analyzed magnetic properties of the Py thin film affected by various pattern sizes: large length-to-width ratio can create larger anisotropy field to increase the FMR. For magnetized Py patterns, surface charges are induced and then contribute magnetic fields in an opposition direction to the applied magnetic field. With a longer distance between the two poles of surface charges, the demagnetizing field along the easy axis can be decreased and therefore, the total anisotropy field will increase to support the high-frequency

application with the extra induced self-biasing field. According to Kittel's equation, the FMR of the patterned Py thin film can be roughly calculated according to the patterning dimension. Take the rectangular strips shown in Figure 5.2 as an example, considering the Py film patterns with length  $L$  (x-axis), width  $W$  (y-axis) and thickness  $h$  (z-axis), the demagnetizing factors along the easy axis can be described as  $N_x = W/L$ ,  $N_y = \varepsilon$  ( $\varepsilon = h/W$ ),  $N_z = 1 - \varepsilon$  [99]. From Kittel's equation [70], the patterned rectangular bars shown in Figure 5.2 (a) and Figure 5.2 (b) can be roughly estimated as 3.6GHz and 4.4GHz respectively.

The FMR of ferromagnetic material is defined as the energy absorption mechanism in the precession movement of the magnetization. According to the energy transmission on the ferromagnetic material, the FMR of patterned Py thin can be characterized with the scattering parameters of transmission line using a Vector Network Analyzer (VNA). The measurement can be taken with a transmission line applied on engineered substrate. The transmission coefficient will drop to a minimum value when the patterned Py thin film on the engineered substrate becomes resonant at a certain frequency at which the transmitted electromagnetic energy is absorbed due to the ferromagnetic resonance from the patterned Py thin film. A transmission line with a length of 42mm fabricated on the LCP board is performed respectively on the engineered substrate with different patterned size. The insertion loss from the one millimeter transmission line on the two patterned Py thin film based engineered substrate is shown in Figure 5.4. The measured FMR for the transmission line on the patterned size of  $25\mu\text{m}$  by  $10\mu\text{m}$  is 3.3GHz, while the FMR for the patterned size of  $45\mu\text{m}$  by  $5\mu\text{m}$  is 4.2GHz.



This shows that the bigger aspect ratio of patterned Py thin film can produce a larger FMR, which agrees well within the estimated results from Kittel's equation.

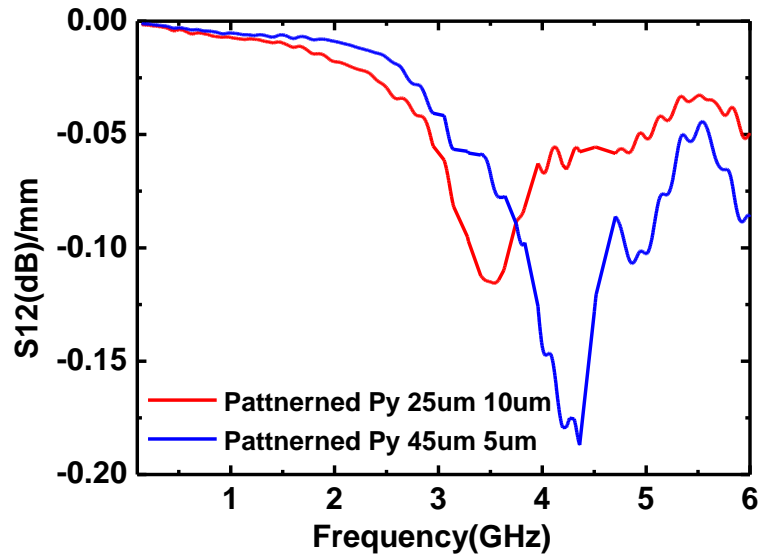


Figure 5.4 FMR effects on engineered substrate with different patterned Py thin film

### 5.2.3 Loss Effects of the Engineered Substrate

With extra fabricated DC bias lines and patterned Py thin film, the loss effects of the engineered substrate is larger than normal silicon substrate. The DC bias line provides extra conduction loss to the substrate and the patterned Py thin film introduces magnetic loss to the substrate. In addition, the implementation of the engineered substrate requires bonding the engineered substrate with other substrates, which can bring about extra loss to the devices due to the air gap between the bonds substrates. Although the patterned Py thin film has a high permeability value and increases the FMR to an acceptable range for high frequency application, the magnetic loss still exists in the materials. Take the design

of patch antenna on the engineered substrate as an example, the maximum fractional bandwidth of antenna can be expressed as [101,102]

$$FBW_{max} = \frac{VSWR-1}{Q_{total}\sqrt{VSWR}} \quad (5-1)$$

where  $Q_{total}$  represents the total quality factor of antenna which describes the total loss from the engineered substrate and can be calculated by:

$$1/Q_{total} = 1/Q_{rad} + 1/Q_{die} + 1/Q_{mag} + 1/Q_{con} + 1/Q_{gap} \quad (5-2)$$

where  $Q_{rad}$  represents the quality factor of the radiation from the antenna.  $Q_{die}$  represents the quality factor of dielectric tangent losses from the dielectric substrate and patterned Py thin film.  $Q_{mag}$  represents the quality factor of magnetic tangent loss contributed by the patterned Py thin film.  $Q_{con}$  represents the quality factor of conduction loss from the patch antenna and DC bias lines;  $Q_{gap}$  represents the quality factor of loss from the EBG effects and air gap between the engineered substrate and a printed PCB substrate.

Actually the bandwidth of tunable RF devices on the engineered substrate is linked to the quality factor which represents the loss of the engineered substrate. According to equation (5-2), the total quality factor decrease with the added magnetic and dielectric loss from substrate. Therefore, the decreased quality factor leads to the increased bandwidth of devices on the engineered substrate. The large bandwidth of the antenna or other RF devices on the engineered substrate comes at the price of small radiation efficiency or transmission loss. Because of the nano-scale (100nm) thickness of the patterned Py thin film, the total thickness of the patterned Py film is less than one thousandth of the total thickness of the engineered substrate (550 $\mu$ m). Therefore, the magnetic loss from Py thin film is not the major contribution to the bandwidth of antenna. In addition, the discontinuous connected patterned film plays an important role in

suppressing eddy currents on the surface of the magnetic material and thus decreasing the coupling effects among Py patterns, which further reduces the magnetic loss and puts it in a tolerable small range.

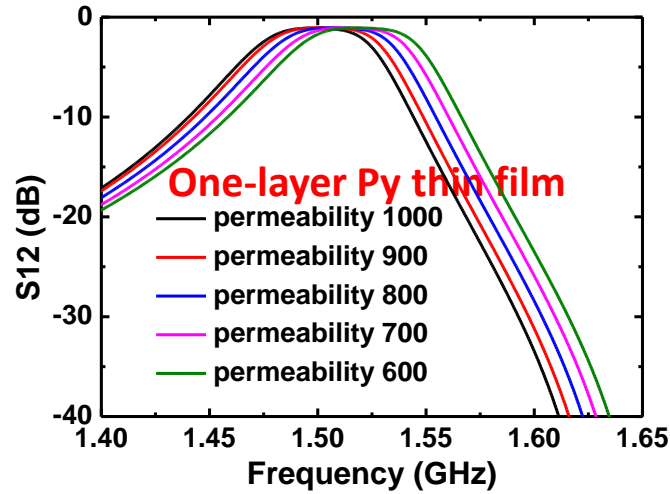
### 5.3 Tuning Property of Engineered Substrate

The tuning property of the engineered substrate can be affected by many factors. The effects of the thickness of the patterned Py thin film, the orientation of patterned Py thin film, the different structures of transmission line and joule heating are mainly discussed and analyzed in this section. An approach to decrease to the tuning current property is also introduced.

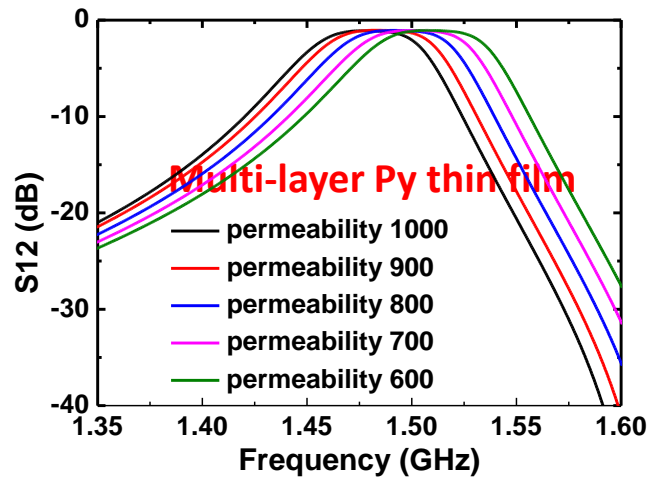
#### 5.3.1 Thickness Effects of Patterned Py Thin Film

Increasing the thickness of the patterned Py thin film is thought to increase the effective permeability of the engineered substrate and improve the tunable range of device on the substrate simultaneously. With a thicker layer of ferromagnetic material, more magnetic moments per volume can be introduced to the substrate and is impacted by the tuning DC current [99]. The effective permeability of the engineered substrate is thus proportional to the thickness of the Py film layers. Currently, the fabricated thickness of the patterned Py thin film is 100nm. To ensure the quality of deposited patterned Py film, the thickness of patterned Py thin film is increased with a multi-layered structure. The thickness of the patterned Py thin film can be increased up to a micrometer when using a multi-layered patterned Py thin film on the substrate. To verify that the thickness of the patterned Py thin film affects the tunable property of the engineered substrate, an optimized tunable microstrip filter designed on the engineered

substrate with one-layer patterned (100nm) Py thin film and multi-layered (1 $\mu$ m) patterned Py thin film is simulated in HFSS and the tunable performance under the same permeability range is shown in Figure 5.5(a) and Figure 5.5(b).



(a)



(b)

Figure 5.5 Tunable microstrip filter on engineered substrate with (a) One-layer patterned Py thin film with thickness of 100 nm (b) Multi-layer patterned Py thin film with thickness of 1 $\mu$ m thin film

As the tunable performance shown from the simulation results, the filter designed on multi-layered Py thin film based engineered substrate obtains a larger tunable range as expected. When changing the permeability of the thin layered Py film, the filter on the one-layer substrate shows a tunable range with center frequency shifted from 1.5GHz to 1.54GHz while the filter on the multi-layer substrate has a smaller tunable range with center frequency shift from 1.47GHz to 1.53GHz. In addition, the simulated filter on the multi-layered patterned film has a smaller center resonant frequency than the one-layered patterned film, which is partly due to the increased total thickness of the substrate and mainly contributed by the increased effective permeability over the whole substrate. Therefore, the simulation results initially demonstrate that increasing the thickness of the patterned Py thin film can be an effective approach to increase the tunable range and decrease the dimensions of RF devices.

### 5.3.2 Orientation Effects of Patterned Py Thin Film

As introduced in the previous chapter, there is a preferred direction in magnetic materials called the easy axis representing the direction which the magnetically anisotropic material tend to align with [66]. Therefore, the oriented direction of the patterned Py thin film also affects the tunable property of the engineered substrate. The applied DC magnetic field exerts different effects on the easy axis and the hard axis of the Py thin film. The orientation of easy axis of the patterned Py thin film bars is chosen to be perpendicular to the DC bias lines as shown in Figure 5.6 (a), which makes the applied DC magnetic field parallel to the easy axis of the film. In this condition, when the RF devices are implemented on the substrate, the RF field generated from the AC signal is perpendicular to the easy axis of the Py patterns (along the hard axis) while the

magnetization oscillates with the external field. Another approach to deposit the patterned Py thin film is to make its easy axis oriented along the direction of DC bias line as shown in Figure5.6 (b). In this condition, the applied DC magnetic field is controlled perpendicular to the easy axis of the Py patterns while the RF field generated from RF devices is parallel to the easy axis.

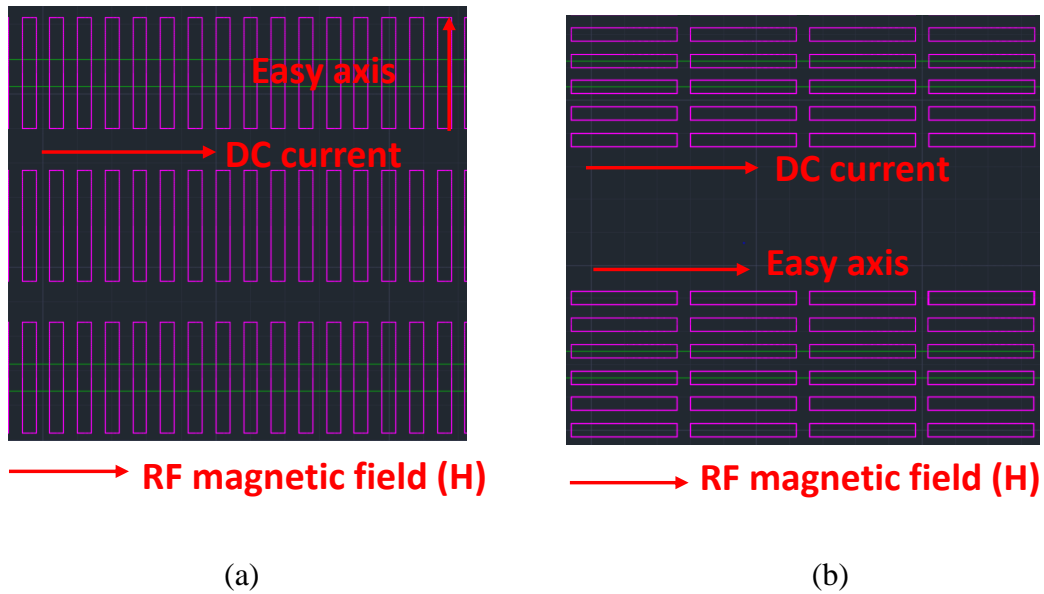


Figure5.6 Patterning orientation of Py thin film with easy axis (a) Perpendicular to DC bias line (b) Parallel to DC bias line

In the high-frequency range, the magnetization along hard axis always exhibits higher permeability than the magnetization along easy axis [103]. The rotational magnetization process governs the magnetic flux reversal along the hard axis, while the magnetic domain movement and resulting large eddy current losses are significant along the easy axis [104]. The RF field generated hard axis excitation can effectively contribute the total magnetic flux associated with the signal line and accordingly the permeability of substrate. So the orientation of the patterned Py film in Figure5.6 (a) can

presents better tunable properties from RF devices. The hysteresis loop of the B-H curve is another approach to analyze the orientation effects of the patterned Py thin film on the engineered substrate. The hysteresis loop of the ferromagnetic material along the easy axis and the hard axis are shown in Figure5.7. It shows that the hysteresis loop along the easy axis has a larger loop area which means that there is a larger coercivity and magnetic loss from the movement of the domain wall, while the hysteresis along the hard axis is nearly a straight line due to the spin rotation which makes the ferromagnetic material have larger permeability along the hard axis for the RF field and smaller magnetic loss. Therefore, the easy axis perpendicular to the DC bias line is the preferred direction for the application considering miniaturization and tunable RF components as the description shows in Figure5.6 (a).

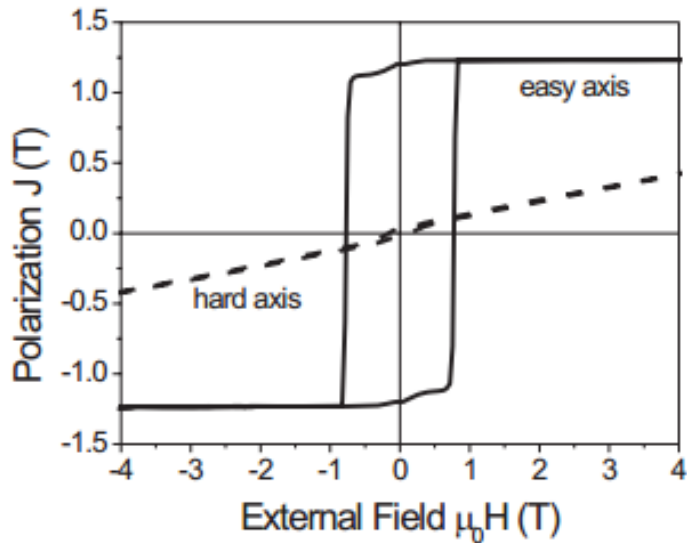


Figure5.7 Hysteresis loop of ferromagnetic material along easy axis and hard axis [105]

### 5.3.3 Effects of Different Types of Structure

Microstrip and coplanar waveguides (CPW) are two types of planar structures widely developed with PCB technology which can be suitable for designing tunable devices on the engineered substrate due to their simplicity in fabrication. These two planar structures have similar propagation modes: dominate operation in quasi transverse-electromagnetic (TEM) mode combined with some undesired spurious waves in Hybrid transverse-electric (TE) and hybrid transverse-magnetic (TM) modes. However, microstrip and CPW structure are different in terms of loss, interface connection, electromagnetic wave distribution, dispersion and the characterization of transmission impedance. For microstrip based structure, the important parameters of RF components include the width of the transmission signal and the thickness of the substrate. For CPW structure, besides the important parameters for the microstrip structure, the space between the ground and signal on the coplanar are important parameters for the CPW structure. The difference between the microstrip and CPW structure can be seen from the electromagnetic field distribution. Two basic microstrip and CPW structure based transmission lines with the distribution of electromagnetic field are shown in Figure 5.8 (a) and Figure 5.8 (b). With coplanar GSG configuration, CPW structure can suffer more conduction loss than the microstrip structure. The wave propagation in microstrip structure is dispersive naturally due to the different phase velocity of EM waves between the air and the substrate as shown in Figure 5.8 (a). With tight coupling from the GSG signal on the top surface of the same interface, CPW structure can have more EM waves propagating in the air to achieve less dispersion as shown in Figure 5.8 (b). EM waves in CPW structure based components are less sensitive to the properties of the substrate and



the inhomogeneity between the substrate and free space. It seems that the components designed with microstrip structure implemented on the engineered substrate can obtain higher tunability than that with CPW structure. In order to understand the property effects of the engineered substrate on different structures, the tunable property of microstrip and CPW structure based reconfigurable devices on the engineered substrate is compared and analyzed in this section.

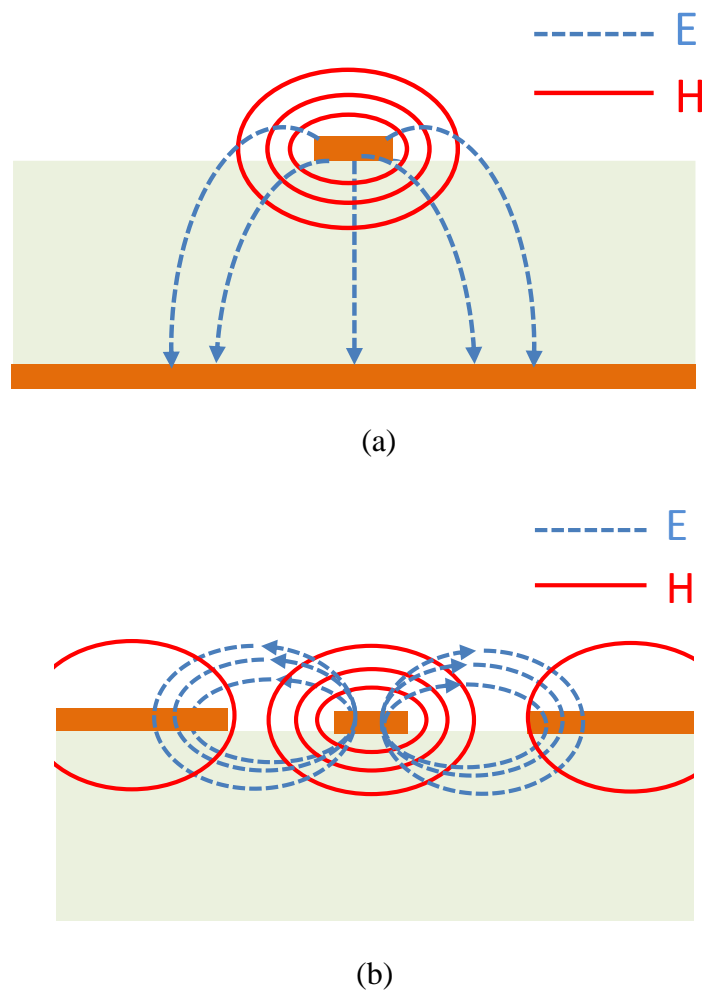


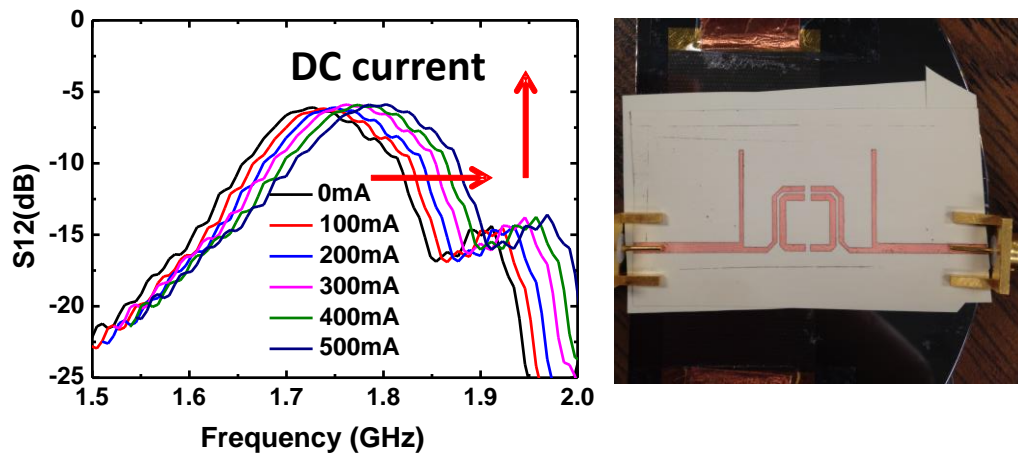
Figure 5.8 Electromagnetic field distribution in (a) Microstrip based transmission line (b) CPW based transmission line

An initial comparison is performed with EM models of two microstrip and CPW structure based transmission lines. The signal line of the two structures is optimized with the same width of  $0.4\mu\text{m}$  and both lines have a characteristic impedance of  $50\Omega$ . The substrate consists of a  $550\mu\text{m}$  engineered substrate and  $100\mu\text{m}$  LCP. For a CPW based transmission line, the air gap between the signal line and ground line is  $0.21\mu\text{m}$ . The finite element analysis software (ANSYS Q3D Extractor) is applied to extract the AC inductance of the microstrip and CPW structure based transmission lines. Adjusting the equivalent permeability of the patterned Py thin film on the engineered substrate, the percentage change of the inductance value on different structures based transmission line can be obtained. The extracted equivalent AC inductances from two structures under different permeability are listed in Table 5.1. The simulated results show that the extracted AC inductances from two structures can both be increased with the increase of permeability on the substrate. The average percentage change of inductance from the microstrip is 2.1, which is 1.5 times of that of the CPW transmission line (the average percentage change is evaluated as 1.4). Therefore, the microstrip structure shows a higher tunable range in simulation

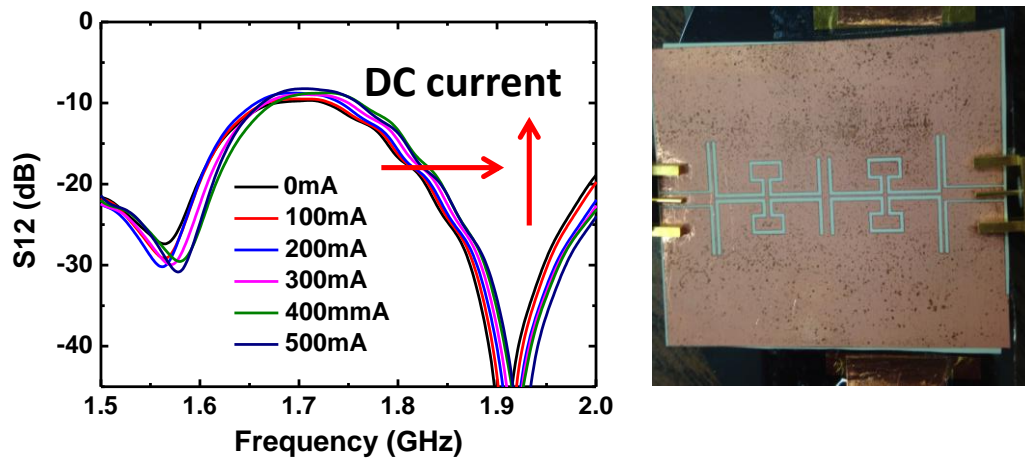
Table 5.1 Extracted equivalent inductance under different permeability

Inductor of Structure	Tunable $\mu_r$				
	600	700	800	900	1000
Microstrip	38.22nH	39.241nH	40.159nH	40.919nH	41.629nH
CPW	34.796nH	35.263nH	35.618nH	36.096nH	36.565nH

To better understand the tunable performance of these two structures based RF components implemented on engineered substrate, two filters designed with these two structures working around similar frequencies are designed and fabricated respectively as shown in Figure 5.9 (a) and Figure 5.9 (b). The center resonant frequency of the microstrip based bandpass filter can shift from 1.72GHz to 1.76GHz when the applied DC current is increased from 0mA to 500mA as shown in Figure 5.9 (a), while the center resonant frequency of the CPW based bandpass filter is obviously changed as shown in Figure 5.9 (b). The mean power bandwidth in the calibration process of the VNA is set so large that it makes the measured performance of the microstrip bandpass have some harmonic waves. There is an air gap between the engineered substrate and the PCB board of the device, which makes the measured performance of the two bandpass filters become worse. In the future, the optimization of the bandpass filter should have a thin air gap layer added in the simulation of EM models to reduce the loss effects from the air gap in measurement. The simulated results for the basic transmission lines and the measurement performance from the two structures based bandpass filter show that the tunable permeability of the engineered substrate can have more effects on the microstrip structure based components than CPW structure. This can be explained by the wave distributions because there is more propagating electromagnetic waves distributed in the air of CPW structure than that of the microstrip structure. The microstrip structure is more sensitive to the properties of the engineered substrate. The comparison and evaluation of the tuning properties on the engineered substrate with two different structures provides a better understanding to design arbitrary tunable components with the proposed engineered substrate.



(a)



(b)

Figure 5.9 (a) Microstrip structure based bandpass filter (b) CPW structure based bandpass filter

### 5.3.4 Effects of Joule Heating on Tuning Property

Besides the DC magnetic field, joule heating is thought to be another source of the change of permeability from the change of magnetic anisotropy. With DC current going through the bias gold lines, heat is generated from the resistance of the bias lines

causing an increase in temperature on the patterned Py thin film. The temperature is related to the saturation magnetization  $M_s$  of the ferro-magnetic material [106] :

$$M_s(T) = M_0 \left[ 1 - \left( \frac{T}{T_c} \right)^{1.5} \right] \quad (5-4)$$

where  $M_0$  is the saturation magnetization at temperature ( $T=0K$ ),  $T_c$  refers to the curie temperature defined as  $450^{\circ}C$  for Py film. According to the equation (5-4), the saturation magnetization  $M_s$  of the Py thin film decreases with the increasing temperature, which in turn results in the decrease of the total magnetic anisotropy and thus the permeability. In addition, thermal effects can work as domain wall depinning [107], and domain reconfiguration [108] which can tilt the magnetic anisotropy away from its easy axis and then further reduce the permeability of the patterned Py thin film. However, as one of the contributors to the total magnetic anisotropy, the temperature induced change in saturation magnetization among the total magnetic anisotropy is negligible. The previously performed experiments demonstrate that the highest change of magnetic anisotropy induced from temperature in the saturation magnetization was estimated as 5.33% which is small and negligible [92]. It can be concluded that the DC current generated ampere field is the major source for the change of the magnetic anisotropy that induces the change in the permeability and FMR, but not Joule heating. The experiments implemented in this this dissertation demonstrates that the shifted frequency is not contributed by the small change in temperature when the frequency shift of the components happened within the change of the DC current in a short time and do not keep on changing as the increase of joule heating.

### 5.3.5 Decrease of Tuning Current on Engineered substrate

According to the implementation of the engineered substrate, the applied tuning current for the frequency shift of the RF component is too large to be implemented in a real circuit even though the total power consumption of the circuit is small. Actually the DC bias lines are arranged on the overall footprint of the engineered substrate which results in a total number of 354 DC bias lines and large tuning current needed for one electrode of all the parallel lines. Each DC bias line only undertakes a small current of 1.4mA when an applied 500mA DC current is divided by the number of DC bias lines. The devices are mainly arranged on the middle part of engineered substrate. The applied tunable current could be reduced if the tuning current is only applied to the device area. Take the tunable SRR filter as an example; the bandpass filter only takes one-third of the footprint of the engineered substrate as shown in Figure5.10. The applied 800mA DC current for the tunable range of 140MHz can be re-evaluated with 180mA. For the design of tunable RF components, it is the DC bias lines below the components that contribute to the tuning effects for the change of permeability. Therefore, the tuning current could be

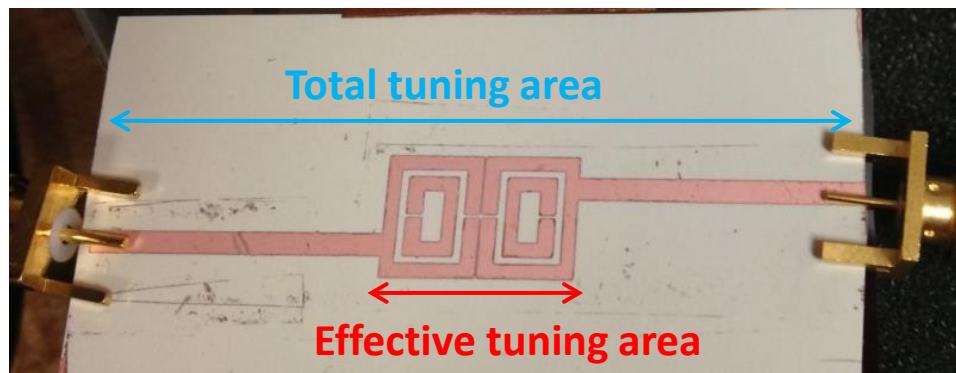


Figure5.10 Analysis of effective tuning area for bandpass filter

reduced when only considering the number of effective DC bias line under the device area. Discontinuous electrodes for DC bias lines can be adopted for partly tuning the selected DC bias lines under the device area to reduce the tuning current with the reduced number of DC bias lines in the circuit.

#### 5.4 Conclusions

This chapter mainly investigated and analyzed the characteristics effects of the engineered substrate. The limitation and tuning property of the engineered substrate were respectively presented. The limitation of the engineered substrate is affected by the bandgap effects from the DC bias lines and FMR of the patterned Py thin film on the substrate. The operating frequency of the RF components should be designed below a certain frequency to reduce the effects from these two factors. Due to the specially designed structure of the engineered substrate, there are extra losses are introduced to the substrate which decrease the quality factor. The device implemented on the engineered substrate can achieve a larger bandwidth than a normal substrate by sacrificing radiation efficiency for the antenna or transmission loss for other devices. The tuning property of the substrate can be affected by the thickness of the patterned Py thin film, the orientation of the patterned Py thin film, the structure type of the device and Joule heating. Wider tunable range and larger effective permeability can be achieved with multi-layered Py thin film on substrate. With smaller magnetic loss and larger permeability, the easy axis perpendicular to the DC bias line is the preferred direction for the design of tunable and miniaturized RF device on engineered substrate. The experimental results also show that microstrip based planar structure is more suitable to design tunable devices than CPW structure. Due to the air gap from the engineered substrate and PCB in measurement, a

thin layer of air gap should be considered and added into the simulation for the optimization of the device. Instead of applying DC current on the whole substrate, properly choosing DC bias line under the effective device area reduce the applied tuning current while keeping the same tunable range. Through theoretical and experimental analysis of the change in magnetic anisotropy field which is resulted from the change of temperature, the tuning property from the effects of joule heating can be negligible, which demonstrate the tuning property from the DC magnetic field.



## CHAPTER 6

### CONTRIBUTIONS AND FUTURE WORKS

#### 6.1 Summary of Contributions

In this dissertation, the contributed work can be divided into two major parts: the design and optimization of an inductively coupled wireless communication system for the telemetry of bio-pressure sensor and the design of miniaturized RF components with a novel tunable engineered substrate for wireless communication system. Each part is developed with following contents:

The first part is focused on the design and optimization of an inductively coupled wireless bio-pressure sensor system using the design of experiments method (DOE). Making use of the recent advances in micro-electromechanical systems (MEMS) and semiconductor technology, the micro-fabricated bio-pressure sensor is proposed and designed as a miniaturized LC resonant circuit and featured with a pressure-dependent capacitance to enable noncontact pressure sensing through inductive coupling between two coils. To make it implantable, the bio-pressure sensor needs a sufficiently small size within the footprint of 3.2 mm by 3.2 mm and operates in the Medical Implant Communication Service (MICS) band of 402-405 MHz. However, the design constraints limit the optimization flexibility of geometrical parameters to increase the inductive sensitivity and pressure sensitivity because of the increased parasitic effects in the small footprint. An optimization on performance related factors is thus presented with an

analysis of inductive sensitivity as well as pressure sensitivity. With mutually dependent geometrical parameters and performance related RF characteristics involved in the full optimization of the system, an optimization approach, DOE method, is introduced to reduce the large number of combined groups of values in factorial simulations to focus on a few performance related RF factors. Efficacy of the proposed design and optimization method has been demonstrated in the wireless sensor system. Both simulation and measurement results demonstrate the working wireless sensor system with a simplified inductive circuit.

The second part systematically explored the design, characterization and application of an engineered substrate deposited with patterned Py thin film for developing miniaturized and electrically tunable RF components. Although there are great advantages of using ferromagnetic material in designing miniaturized and tunable RF components, it is still challenging to have the magnetic material working up to the GHz range due to small FMR. Magnetic property of Py patterns is thus analyzed and adopted in the engineered substrate to improve the FMR up to several GHz and extends its application in high-frequency devices. A magneto-dielectric substrate, consisting of high-resistivity silicon substrate deposited with patterned Py thin film, is initially developed for the design of the miniaturized components. Besides the high-permeability for designing miniaturization of RF components, the permeability of the Py thin film can be also adjusted by external magnetic field and DC current. Instead of using the cumbersome external bias field, an electrically tunable substrate, a new substrate evolved from the magneto-dielectric substrate with a special layer of DC current bias lines under the patterned Py thin film, is proposed and designed for developing arbitrary tunable RF

components. The tuning properties of the engineered substrate is demonstrated by the design and implementation of different types of components such as antenna, phase shifter, filter and balun. All the theoretical and experimental results demonstrate the electrically tunable property of the engineered substrate for developing arbitrary RF components. This dissertation also researched the fabrication approach of the substrate. The fabrication approach for the application engineered substrate is also explored. The engineered substrate is fabricated using the DC magnetron sputtering method while the RF components are designed independently with PCB technology, which shows a unique flexible design methodology. The characteristic effects of the engineered substrate are finally discussed and analyzed a better implementation of the engineered substrate.

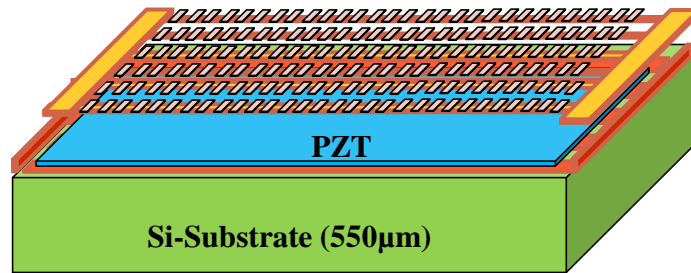
## 6.2 Future Works

Based on the summary of finished work, the future work can be focus on: reducing the loss effects of the ferromagnetic material and DC bias lines of engineered substrate; increasing the tuning range of patterned Py thin film on the engineered substrate with less DC current or power consumption. The loss effects from the patterned Py thin film can be reduced with the further increased FMR through the application of a larger length-to-width aspect ratio on the patterned Py thin film. Compared to the micro-scaled Py patterns, the footprint of the engineered substrate is relatively large. Considering the long fabrication time, the deposited patterning size of Py thin film in the design is  $25\mu\text{m}$  by  $5\mu\text{m}$  and  $45\mu\text{m}$  by  $5\mu\text{m}$ . Besides the increased time for large aspect ratio, the improved FMR causes a decrease of effective permeability for Py thin film. There is a balance between high FMR and high effective permeability for the miniaturization of RF components. The EBG effects of the engineered substrate can be

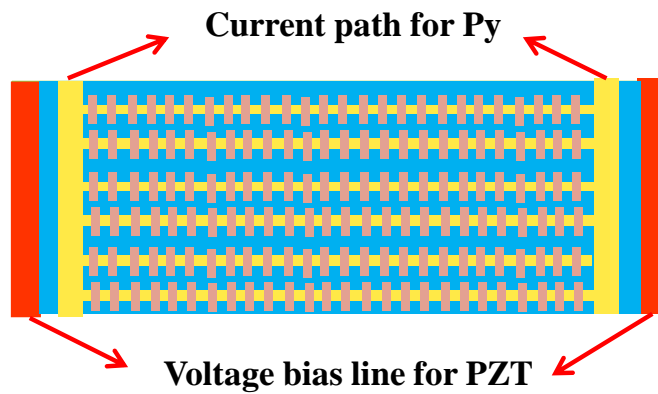
reduced through reducing the number of DC bias line or increasing the lattice gap between middle connection parts. The middle connection parts can be reduced if the quality of deposited DC bias lines can be guaranteed without disconnection.

Increased tuning range can be achieved with an increase in density of the Py thin film per volume or by incorporating more tunable elements. Thicker Py thin film is expected to bring more tunability than thinner film because more magnetic moments per volume can be impacted by the tuning DC current [99]. According to the simulation results, a multi-layer based patterned thin film can provide a wider tunable range than a one-layer substrate. However, the increased thickness of magnetic material may cause increased loss from eddy current. The increased thickness of the patterned Py thin film should be controlled in certain range to make sure that the loss from eddy current is tolerable. Besides the current tuning magnetic material, there is voltage tuning element which can be integrated into the substrate. Lead Zirconium Titanate (PZT), a kind of ferroelectric material, has voltage-dependent permittivity that can be used to design electrically tunable components [109]. The PZT thin film can be thus integrated into the engineered substrate to achieve a fully electrically tunable substrate as the layout shown in Figure 6.1. With both current-dependent permeability and voltage-dependent permittivity, the tunable range of the engineered substrate can be greatly increased. In addition, with the approach to reduce the EBG effects and the reduced number of DC bias line, the tuning range can be increased due to the increased undertaken current for each bias. Another approach to reduce the tuning current can be achieved through partially tuning. As shown in Figure6.2, the electrode can be divided into several discontinuous

parts, then the current can be selectively applied to the area with RF devices, which in turn can reduce the required tuning current.



(a)



(b)

Figure 6.1 (a) 3D layout of fully electrically tunable engineered substrate (b) Top view of fully electrically tunable engineered substrate

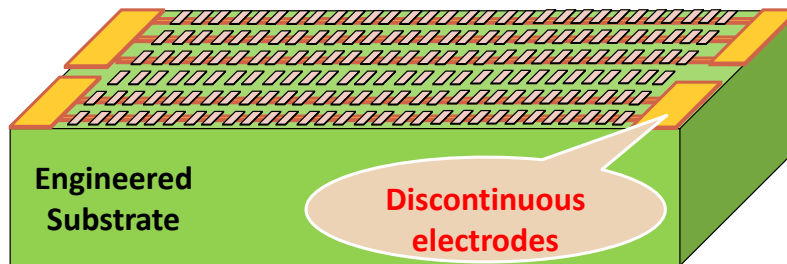


Figure6.2 Improved layout of engineered substrate with a discontinuous electrodes for partly tuning

## REFERENCES

- [1] Alt, E., and Stotts, L. J.. "Cardiac pacemaker with bidirectional communication." U.S. Patent No. 6,080,187. 27 Jun. 2000.
- [2] Shichiri, M., Asakawa, N., Yamasaki, Y., Kawamori, R., and Abe, H. "Telemetry glucose monitoring device with needle-type glucose sensor: a useful tool for blood glucose monitoring in diabetic individuals." *Diabetes Care* 9.3 (1986): 298-301
- [3] White, G., Hill, R., Zakrewski, M. J., Kummerlen, R., Abbott, M. S., and Brooks, R. C. "Patient medication IV delivery pump with wireless communication to a hospital information management system." U.S. Patent No. 6,790,198. 14 Sep. 2004
- [4] Valdastrì, P., Quaglia, C., Susilo, E., Menciassi, A., Dario, P., Ho, C. N., and Schurr, M. O. "Wireless therapeutic endoscopic capsule: in vivo experiment." *Endoscopy* 40.12 (2008): 979
- [5] Lizón-Martínez, S., Giannetti, R., Rodríguez-Marrero, J. L., and Tellini, B. "Design of a system for continuous intraocular pressure monitoring." *IEEE transactions on instrumentation and measurement* 54.4 (2005): 1534-1540.
- [6] Freudenthal, E., Herrera, D., Kautz, F., Natividad, C., Ogrey, A., Sipla, J., and Estevez, L. "Evaluation of HF RFID for implanted medical applications." (2007).
- [7] Chu, H., Wu, G., Chen, J., and Zhao, Y. "Study and simulation of semi-active RFID tags using Piezoelectric Power Supply for mobile process temperature sensing." *Cyber Technology in Automation, Control, and Intelligent Systems (CYBER), 2011 IEEE International Conference on*. IEEE, 2011.
- [8] Rowell, C. R., and Murch, R. D. "A compact PIFA suitable for dual-frequency 900/1800-MHz operation." *IEEE Transactions on Antennas and Propagation* 46.4 (1998): 596.
- [9] Gosalia, K., and Lazzi, G. "Reduced size, dual-polarized microstrip patch antenna for wireless communications." *Antennas and Propagation, IEEE Transactions on* 51.9 (2003): 2182-2186.

- [10] Mosallaei, H., and Sarabandi, K. "Magneto-dielectrics in electromagnetics: Concept and applications." *Antennas and Propagation, IEEE Transactions on* 52.6 (2004): 1558-1567.
- [11] Kärkkäinen, M., Ermutlu, M., Maslovski, S., Ikonen, P., and Tretyakov, S. "Numerical simulations of patch antennas with stacked split-ring resonators as artificial magnetic substrates." *Antenna Technology: Small Antennas and Novel Metamaterials, 2005. IWAT 2005. IEEE International Workshop on*. IEEE, 2005
- [12] Bayraktar, Z., Gregory, M., Kern, D., and Werner, D.H. "Matched impedance thin composite magneto-dielectric metasurfaces." *2009 IEEE Antennas and Propagation Society International Symposium*. 2009
- [13] Buell, K., Mosallaei, H., and Sarabandi, K. "Embedded-circuit magnetic metamaterial substrate performance for patch antennas." *Antennas and Propagation Society International Symposium, 2004. IEEE*. Vol. 2. IEEE, 2004.
- [14] Park, J. Y., and Allen, M. G. "Development of magnetic materials and processing techniques applicable to integrated micromagnetic devices." *Journal of Micromechanics and Microengineering* 8.4 (1998): 307.
- [15] Celinski, Z., and B. Heinrich. "Ferromagnetic resonance linewidth of Fe ultrathin films grown on a bcc Cu substrate." *Journal of Applied Physics* 70.10 (1991): 5935-5937.
- [16] Sroka, P., and Samuels, J. A. "Adaptive antenna matching." U.S. Patent No. 5,778,308. 7 Jul. 1998.
- [17] Wang, X., Bao, P., Jackson, T. J., and Lancaster, M. J. "Tunable microwave filters based on discrete ferroelectric and semiconductor varactors." *Microwaves, Antennas & Propagation, IET* 5.7 (2011): 776-782.
- [18] Entesari, K., and Rebeiz, G. M. "A differential 4-bit 6.5-10-GHz RF MEMS tunable filter." *Microwave Theory and Techniques, IEEE Transactions on* 53.3 (2005): 1103-1110.
- [19] Tagantsev, A. K., Sherman, V. O., Astafiev, K. F., Venkatesh, J., and Setter, N. "Ferroelectric materials for microwave tunable applications." *Journal of electroceramics* 11.1-2 (2003): 5-66.
- [20] Zhao, H. J., Ren, W., Yang, Y., Íñiguez, J., Chen, X. M., and Bellaiche, L. "Near room-temperature multiferroic materials with tunable ferromagnetic and electrical properties." *Nature communications* 5 (2014).

- [21] Amft, O., Junker, H., Lukowicz, P., Tröster, G., and Schuster, C. "Sensing muscle activities with body-worn sensors." *Wearable and Implantable Body Sensor Networks, 2006. BSN 2006. International Workshop on*. IEEE, 2006.
- [22] Stockhammer, R. "Authorization control device including a wristwatch having a biometric sensor." U.S. Patent No. 6,799,726. 5 Oct. 2004.
- [23] Sola, J., Proenca, M., Ferrario, D., Porchet, J. A., Falhi, A., Grossenbacher, O., and Sartori, C.. "Noninvasive and nonocclusive blood pressure estimation via a chest sensor." *Biomedical Engineering, IEEE Transactions on* 60.12 (2013): 3505-3513.
- [24] Horler, G. "Inductively coupled telemetry." *Sensors for Environment, Health and Security*. Springer Netherlands, 2009. 239-252.
- [25] Li, C. Y., Chen, Y. C., Chen, W. J., Huang, P., and Chu, H. H. "Sensor-embedded teeth for oral activity recognition." *Proceedings of the 2013 International Symposium on Wearable Computers*. ACM, 2013.
- [26] Chi, B., Yao, J., Han, S., Xie, X., Li, G., and Wang, Z. "Low-power transceiver analog front-end circuits for bidirectional high data rate wireless telemetry in medical endoscopy applications." *Biomedical Engineering, IEEE Transactions on* 54.7 (2007): 1291-1299.
- [27] Sardini, E., and Serpelloni, M. "Wireless measurement electronics for passive temperature sensor." *Instrumentation and Measurement, IEEE Transactions on* 61.9 (2012): 2354-2361.
- [28] Gao, Y., Zheng, Y., Diao, S., Toh, W. D., Ang, C. W., Je, M., and Heng, C. H. "Low-power ultrawideband wireless telemetry transceiver for medical sensor applications." *Biomedical Engineering, IEEE Transactions on* 58.3 (2011): 768-772.
- [29] Fonseca, M. A., English, J. M., Von Arx, M., and Allen, M. G. "Wireless micromachined ceramic pressure sensor for high-temperature applications." *Microelectromechanical Systems, Journal of* 11.4 (2002): 337-343.
- [30] Leonardi, M., Pitchon, E. M., Bertsch, A., Renaud, P., and Mermoud, A. "Wireless contact lens sensor for intraocular pressure monitoring: assessment on enucleated pig eyes." *Acta ophthalmologica* 87.4 (2009): 433-437.
- [31] Sample, A. P., Yeager, D. J., Powledge, P. S., Mamishev, A. V., and Smith, J. R. "Design of an RFID-based battery-free programmable sensing platform." *Instrumentation and Measurement, IEEE Transactions on* 57.11 (2008): 2608-2615.



- [32] Zhou, M. X., Huang, Q. A., Qin, M., and Zhou, W. "A novel capacitive pressure sensor based on sandwich structures." *Microelectromechanical Systems, Journal of* 14.6 (2005): 1272-1282.
- [33] Parker, R. L., and Krinsky, A. "Electrical Resistance-Strain Characteristics of Thin Evaporated Metal Films." *Journal of Applied Physics* 34.9 (1963): 2700-2708.
- [34] Liu, X., Zhu, Y., Nomani, M. W., Wen, X., Hsia, T. Y., and Koley, G. "A highly sensitive pressure sensor using a Au-patterned polydimethylsiloxane membrane for biosensing applications." *Journal of Micromechanics and Microengineering* 23.2 (2013): 025022
- [35] Suhara, M., Okayama, M., and Okumura, T. "Analysis of scaling-rule and size-reduction limit of spiral inductors to maximize quality factor." *Microwave Conference Proceedings, 2005. APMC 2005. Asia-Pacific Conference Proceedings*. Vol. 5. IEEE, 2005.
- [36] Simons, R. N., Hall, D. G., and Miranda, F. A. "RF telemetry system for an implantable bio-MEMS sensor." (2004).
- [37] Burghartz, J. N., Edelstein, D. C., Soyuer, M., Ainspan, H. A., and Jenkins, K. A. "RF circuit design aspects of spiral inductors on silicon." *Solid-State Circuits, IEEE Journal of* 33.12 (1998): 2028-2034.
- [38] Ashby, K. B., Koullias, I. A., Finley, W. C., Bastek, J. J., and Moinian, S. "High Q inductors for wireless applications in a complementary silicon bipolar process." *Solid-State Circuits, IEEE Journal of* 31.1 (1996): 4-9.
- [39] Yue, C. Patrick, and S. Simon Wong. "On-chip spiral inductors with patterned ground shields for Si-based RF ICs." *Solid-State Circuits, IEEE Journal of* 33.5 (1998): 743-752.
- [40] Mohan, S. S., del Mar Hershenson, M., Boyd, S. P., and Lee, T. H. "Simple accurate expressions for planar spiral inductances." *Solid-State Circuits, IEEE Journal of* 34.10 (1999): 1419-1424.
- [41] Ong, K. G., Grimes, C. A., Robbins, C. L., and Singh, R. S. "Design and application of a wireless, passive, resonant-circuit environmental monitoring sensor." *Sensors and Actuators A: Physical* 93.1 (2001): 33-43.
- [42] Huang, X., and Cao, Y. "3D-Solenoid MEMS RF Inductor Design in Standard CMOS Technology." *Electrical Engineering and Computer Sciences, College of Engineering, UC Berkeley* 4.

- [43] Vandevoorde G., and Puers R., " Wireless energy transfer for stand-alone systems: a comparison between low and high power applicability," *Sensors and Actuators A: Physical*, vol.92, no.1, 2001, pp.305-311.
- [44] Xue N., Chang S.P., and Lee J.B., "A SU-8-based microfabricated implantable inductively coupled passive RF wireless intraocular pressure sensor," *J. MEMS* vol. 21, no.6, 2012, pp.1338-1346.
- [45] Chen P.J., Saati S., Varma R., Humayun M.S., and Tai Y.C., "Wireless intraocular pressure sensing using microfabricated minimally invasive flexible-coiled LC sensor implant," *J. MEMS* , vol.19, no.4, 2010, pp.721-73.
- [46] Zang, Y., Zhang, F., Di, C.A. and Zhu, D.. "Advances of flexible pressure sensors toward artificial intelligence and health care applications." *Materials Horizons* 2, no. 2 (2015): 140-156.
- [47] Burghartz, J. N., and Rejaei, B. "On the design of RF spiral inductors on silicon." *Electron Devices, IEEE Transactions on* 50.3 (2003): 718-729.
- [48] Ng, K. T., Rejaei, B., and Burghartz, J. N. "Substrate effects in monolithic RF transformers on silicon." *Microwave Theory and Techniques, IEEE Transactions on* 50.1 (2002): 377-383.
- [49] Mutashar S., Hannan M.A., Samad S.A. , and Hussain A., "Analysis and optimization of spiral circular inductive coupling link for bio-implanted applications on air and within human tissue." *Sensors*, vol. 14, no. 7 , 2014, pp. 11522-11541.
- [50] Raj, P. M., Chakraborti, P., Sharma, H., Han, K., Gandhi, S., Sitaraman, S., & Tummala, R. "Tunable and miniaturized RF components with nanocomposite and nanolayered dielectrics." *Nanotechnology (IEEE-NANO), 2014 IEEE 14th International Conference on*. IEEE, 2014.
- [51] Altunyurt, N., Swaminathan, M., Raj, P. M., and Nair, V. "Antenna miniaturization using magneto-dielectric substrates." *Electronic Components and Technology Conference, 2009. ECTC 2009. 59th*. IEEE, 2009.
- [52] Niamien, C., Collardey, S., Sharaiha, A., and Mahdjoubi, K. "Compact expressions for efficiency and bandwidth of patch antennas over lossy magneto-dielectric materials." *Antennas and Wireless Propagation Letters, IEEE* 10 (2011): 63-66.
- [53] Ramprasad, R., Zurcher, P., Petras, M., Miller, M., and Renaud, P. "Fundamental limits of soft magnetic particle composites for high frequency applications." *physica status solidi (b)* 233.1 (2002): 31-38.

- [54] Lopusnik, R., Nibarger, J. P., Silva, T. J., and Celinski, Z. "Different dynamic and static magnetic anisotropy in thin Permalloy™ films." *Applied physics letters* 83.1 (2003): 96-98.
- [55] Cullity, B. D., and Graham, C. D.. *Introduction to magnetic materials*. John Wiley & Sons, 2011.
- [56] Zhang, S., and Zhang, S. S. L. "Generalization of the Landau-Lifshitz-Gilbert equation for conducting ferromagnets." *Physical review letters* 102.8 (2009): 086601.
- [57] L. Tauxe, S.K. Banerjee, R.F. Butler, and van der Voo, *Essentials of Paleomagnetism*, 2nd Web Edition, 2012, Available online: <http://magician.ucsd.edu/essentials/WebBook.html>.
- [58] N. Engheta, "Electromagnetics of complex media and metamaterials," *2002 Intl. Conf. Mathematical Methods in Electromagnetic Theory*, Vol. 1, pp. 175-180, 2002.
- [59] Gomez, R. D., Luu, T. V., Pak, A. O., Kirk, K. J., and Chapman, J. N. "Domain configurations of nanostructured Permalloy elements." *Journal of applied physics* 85.8 (1999): 6163-6165.
- [60] Hitchhiker's Guide To Magnetism. Available online: [http://www.irm.umn.edu/hg2m/hg2m\\_index.html](http://www.irm.umn.edu/hg2m/hg2m_index.html)
- [61] Herzer, G. "Magnetization process in nanocrystalline ferromagnets." *Materials Science and Engineering: A* 133 (1991): 1-5
- [62] Morales, C. A. "Magneto-Dielectric Polymer Nanocomposite Engineered Substrate for RF and Microwave Antennas." (2011).
- [63] B. M. F. Rahman, R. Divan, H. Zhang, D. Rosenmann, Y. Peng, X. Wang, and G. Wang, "Direct current tunable noise suppressor using sub-micrometer patterned Permalloy films," *J. Appl. Phys.*, vol. 115, p. 17E515, Feb. 2014.
- [64] Zhang, L., Zhu, W., Zheng, H., Wang, X., Bi, M., Wang, N., Zhou, P.; Lu, H.; Xie, J.; Deng, L., "Thickness-dependent magnetic properties of patterned FeCoBSi amorphous thin films on silicon substrate," in *Magnetics, IEEE Transactions on* , vol.PP, no.99, pp.1-1.
- [65] Bertotti, G. "General properties of power losses in soft ferromagnetic materials." *Magnetics, IEEE Transactions on* 24, no. 1 (1988): 621-630.
- [66] El-Ghazaly, A., Sato, N., White, R. M., and Wang, S. X. "Achieving Isotropic Permeability for Integrated Inductors." *Magnetics, IEEE Transactions on* 51.11 (2015): 1-4.

- [67] Yamaguchi, A., Motoi, K., Hirohata, A., Miyajima, H., Miyashita, Y., and Sanada, Y. "Broadband ferromagnetic resonance of Ni<sub>81</sub>Fe<sub>19</sub> wires using a rectifying effect", *Phys. Rev. B* 78, 104401, Sept. 2008.
- [68] Gevorgian, S. *Ferroelectrics in Microwave Devices, Circuits and Systems: Physics, Modeling, Fabrication and Measurements*. Springer Science & Business Media, 2009.
- [69] Huang, D., Poutrina, E., and Smith, D. R. "Analysis of the power dependent tuning of a varactor-loaded metamaterial at microwave frequencies," *Applied Physics Letters*, vol. 96, no. 10, Article ID 104104, 3 pages, 2010.
- [70] Setter, N., Damjanovic, D., Eng, L., Fox, G., Gevorgian, S., Hong, S., and Stolitchnov, I. "Ferroelectric thin films: Review of materials, properties, and applications." *Journal of Applied Physics* 100.5 (2006): 051606.
- [71] Rebeiz, G. M., and Muldavin, J. B. "RF MEMS switches and switch circuits." *Microwave Magazine, IEEE* 2.4 (2001): 59-71.
- [72] Abdelmoneum, M. A., Demirci, M. U., and Nguyen, C. T. "Stemless wine-glass-mode disk micromechanical resonators." *Micro Electro Mechanical Systems, 2003. MEMS-03 Kyoto. IEEE The Sixteenth Annual International Conference on*. IEEE, 2003.
- [73] Chan, King Yuk, et al. "RF MEMS switchable interdigital bandpass filter." *Microwave and Wireless Components Letters, IEEE* 22.1 (2012): 44-46.
- [74] Chan, K. Y., Fouladi, S., Ramer, R., and Mansour, R. R. "Reconfigurable 4 pole bandstop filter based on RF-MEMS-loaded split ring resonators." *Microwave Symposium Digest (MTT), 2010 IEEE MTT-S International*. IEEE, 2010.
- [75] Wang, X., Bao, P., Lancaster, M. J., and Jackson, T. J. "Ferroelectric lumped element filter/switch for microwave applications." *Microwave Conference, 2008. EuMC 2008. 38th European. IEEE, 2008*.
- [76] Tagantsev, A. K., Sherman, V. O., Astafiev, K. F., Venkatesh, J., and Setter, N. "Ferroelectric materials for microwave tunable applications." *Journal of electroceramics* 11.1-2 (2003): 5-66.
- [77] Yang, X., Wu, J., Beguhn, S., Zhou, Z. Y., Lou, J., and Sun, N. X. "Novel C-band tunable bandpass filter with low bias magnetic fields using partially magnetized ferrites." *Microwave Symposium Digest (MTT), 2012 IEEE MTT-S International*. IEEE, 2012.
- [78] Yang, X., et al. "Novel C-band tunable bandpass filter with low bias magnetic fields using partially magnetized ferrites." *Microwave Symposium Digest (MTT), 2012 IEEE MTT-S International*. IEEE, 2012.

- [79] Rahman, B. F., Divan, R., Zhang, H., Rosenmann, D., Peng, Y., Wang, X., and Wang, G. "High performance tunable slow wave elements enabled with nano-patterned permalloy thin film for compact radio frequency applications." *Journal of Applied Physics* 115.17 (2014): 17A508.
- [80] B. Kuanr, R. E. Camley, and Z. Celinski, "Narrowing of the frequency-linewidth in structured magnetic strips: Experiment and theory", *Appl. Phys. Lett*, vol 87, no. 01, 2005.
- [81] B. M. F. Rahman, "Slow wave structures integrated with ferro-magnetic and ferro-electric thin films for smart RF applications," Ph.D. dissertation, Department of Electrical Engineering, University of South Carolina, Columbia, SC, 2014.
- [82] Rahman, B. F., Divan, R., Zhang, H., Rosenmann, D., Peng, Y., Wang, X., and Wang, G. "Direct current tunable noise suppressor using sub-micrometer patterned permalloy films." *Journal of Applied Physics* 115.17 (2014): 17E515.
- [83] Sun, N. X., & Srinivasan, G. "Voltage control of magnetism in multiferroic heterostructures and devices." *Spin*. Vol. 2. No. 03. World Scientific Publishing Company, 2012.
- [84] Brank, J., Yao, J., Eberly, M., Malczewski, A., Varian, K., and Goldsmith, C. "RF MEMS-based tunable filters." *International Journal of RF and Microwave Computer-Aided Engineering* 11.5 (2001): 276-284.
- [85] Durán-Sindreu, M., Naqui, J., Paredes, F., Bonache, J., and Martín, F. "Electrically small resonators for planar metamaterial, microwave circuit and antenna design: A comparative analysis." *Applied Sciences* 2.2 (2012): 375-395.
- [86] Jindal, S., and Sharma, J. "Review of Metamaterials in Microstrip Technology for Filter Applications." *International Journal of Computer Applications* 54.3 (2012): 48-54.
- [87] García-García, J. , Bonache, J. , Gil, I. Martín, F. , Velazquez-Ahumada, M. C. and Martel, J. "*Microwave Theory and Techniques*." *IEEE Transactions on* 54, no. 6 (2006): 2628-2635.
- [88] Yu, C. C., and Chang, K. "Novel compact elliptic-function narrow-band bandpass filters using microstrip open-loop resonators with coupled and crossing lines." *Microwave Theory and Techniques, IEEE Transactions on* 46, no. 7 (1998): 952-958.
- [89] Pozar, D. M. *Microwave engineering*. John Wiley & Sons, 2009.
- [90] Marqués, R., Martín, F., and Sorolla, M. *Metamaterials with negative parameters: theory, design and microwave applications*. Vol. 183. John Wiley & Sons, 2011.

- [91] Hong, J. S., and Lancaster, M. J. "Theory and experiment of novel microstrip slow-wave open-loop resonator filters." *Microwave Theory and Techniques, IEEE Transactions on* 45, no. 12 (1997): 2358-2365.
- [92] Hong, J. S., & Lancaster, M. J. "Couplings of microstrip square open-loop resonators for cross-coupled planar microwave filters." *Microwave Theory and Techniques, IEEE Transactions on* 44, no. 11 (1996): 2099-2109.
- [93] Wong, J. S., "Microstrip tapped-line filter design." *IEEE Transactions on Microwave Theory Techniques* 27 (1979): 44-50.
- [94] Wang, G., Rahman, F., Xia, T., & Zhang, H. "Patterned Permalloy and Barium Strontium Titanate Thin Film Enabled Tunable Slow Wave Elements for Compact Multi-Band RF Applications." *Magnetics, IEEE Transactions on* 49.7 (2013): 4184-4187
- [95] Hong, J. S., and Lancaster, M. J. "Cross-coupled microstrip hairpin-resonator filters," *IEEE Trans. Microwave Theory Tech.*, vol. 46, pp. 118–112, Jan. 1998.
- [96] Tang, C. W. "Design of a microstrip filter using multiple capacitively loaded coupled lines." *IET Microwaves, Antennas & Propagation* 1, no. 3 (2007): 651-657.
- [108] Hong, J. S., and Lancaster, M. J. "Cross-coupled microstrip hairpin-resonator filters," *IEEE Trans. Microwave Theory Tech.*, vol. 46, pp. 118–112, Jan. 1998.
- [97] Tsai, C. M., Lee, S. Y., and Tsai, C. C. "Performance of a planar filter using a 0 feed structure." *Microwave Theory and Techniques, IEEE Transactions on* 50, no. 10 (2002): 2362-2367.
- [98] Koch, R. H., Grinstein, G., Keefe, G. A., Lu, Y., Trouilloud, P. L., Gallagher, W. J., and Parkin, S. S. P. "Thermally assisted magnetization reversal in submicron-sized magnetic thin films," *Phys. Rev. Lett.*, vol. 84, pp. 5419–5422, June 2000.
- [99] Ilgaz, D., Kläui, M., Heyne, L., Boulle, O., Zinser, F., Krzyk, S., and Heyderman, L. J. "Selective domain wall depinning by localized Oersted fields and Joule heating." *Applied Physics Letters* 93.13 (2008): 132503.
- [100] Belohoubek E. and Denlinger E., "Loss considerations for microstrip resonators," *IEEE Trans. Microw. Theory Tech.*, vol. 23, pp. 522–526, Jun. 1975.
- [101] Carver K. R. and Mink J. W., "Microstrip antenna technology," *IEEE Trans. Antennas Propag.*, vol. 29, pp. 2–24, Jan. 1981
- [102] Pardavi-Horvath, M., Ross, C.A. and McMichael, R.D.. "Shape effects in the ferromagnetic resonance of nanosize rectangular permalloy arrays." *IEEE transactions on magnetics* 41, no. 10 (2005): 3601-3603.

- [103] Yamaguchi, M., Baba, M. and Arai, K.I., 2001 "Sandwich-type ferromagnetic RF integrated inductor.", *49*(12), pp.2331-2335.
- [104] Patra, A.K., 2008. *Crystal Structure, Anisotropy and Spin Reorientation Transition of Highly Coercive, Epitaxial Pr-Co Films*. Cuvillier Verlag.
- [105] Y. Chun, J. S. Hong, P. Bao, T. J. Jackson, M. J. Lancaster, "BST-Varactor Tunable Dual-Mode Filter Using Variable  $Z_c$  Transmission Line," *IEEE Microw. Compon. Lett.*, vol. 18, no. 3, pp. 167-169, 2008.
- [106] Herzer, G. "Grain structure and magnetism of nanocrystalline ferromagnets." *Magnetics, IEEE Transactions on* 25.5 (1989): 3327-3329.
- [107] Koch, R. H., Grinstein, G., Keefe, G. A., Lu, Y., Trouilloud, P. L., Gallagher, W. J., and Parkin, S. S. P. "Thermally assisted magnetization reversal in submicron-sized magnetic thin films," *Phys. Rev. Lett.*, vol. 84, pp. 5419–5422, June 2000.
- [108] Ilgaz, D., Kläui, M., Heyne, L., Boulle, O., Zinser, F., Krzyk, S., and Heyderman, L. J. "Selective domain wall depinning by localized Oersted fields and Joule heating." *Applied Physics Letters* 93.13 (2008): 132503.
- [109] Y. Chun, J. S. Hong, P. Bao, T. J. Jackson, M. J. Lancaster, "BST-Varactor Tunable Dual-Mode Filter Using Variable  $Z_c$  Transmission Line," *IEEE Microw. Compon. Lett.*, vol. 18, no. 3, pp. 167-169, 2008.